Investigations of Bismuth- and Cobalt-based Electrocatalysts for Carbon Dioxide Reduction Reactions

by

Mengnan Zhu

A thesis submitted in partial fulfillment of the requirements for the degree of

Doctor of Philosophy

in

Materials Engineering

Department of Chemical and Materials Engineering

University of Alberta

Abstract

The electrochemical reduction of carbon dioxides (CO_2RR) is a promising solution for mitigating CO_2 emissions while simultaneously generating value-added chemicals. From the perspective of materials engineering, understanding the structure-function relationships is crucial in guiding the rational design of electrocatalysts and advancing CO_2RR technologies. Considering its significance attached, this thesis endeavors to investigate the i) $BaBiO_3$ (BBO) perovskite, ii) Bi- and iii) Co-based electrocatalysts with atomically distributed active sites, with particular focus on how the key structural features including potential-driven reconstructions, coordination environment, and local geometry affect the catalytic performances of CO_2RR.

The first part of this thesis delves into the investigation of the voltage-driven structural reconstructions in the perovskite BBO, resulting in the generation of Bi metallene (eBBO) that manifests an efficient production of formate/formic acid (FA) with appreciable selectivity and partial current densities. Furthermore, Ba^{2+} ions are released into the electrolyte during the course of reconstructions owing to the irreversible exsolution of Bi cations and phase transformations. The combined insights from the time-resolved Fourier-transform infrared spectroscopy (FTIR) and in situ Raman analysis reveal that the adsorption of Ba^{2+} ions at eBBO surface facilitates CO_2 adsorption, leading to an enhanced CO_2-to-FA conversion. This work is of direct significance in uncovering the structural evolutions during electrolysis and elucidating the cooperative catalysis between A- and B- site cations in perovskites for room-temperature CO_2RR.

The second part of this thesis presents a simple and versatile nanosecond pulsed lasers method for the simultaneous confinement of the Bi “single atom” (SA) on graphene-based support for

CO_2RR. The outcomes of the reactions could be controlled by adjusting the compositions of the graphene support. Electrochemical studies disclose that the Bi ensemble supported by pristine or nitrogenated graphene preferably produces FA or syngas, respectively, as the dominant CO_2RR products. X-ray absorption spectroscopy (XAS) and theoretical modeling collectively reveal that the product tunability originates from the distinct electronic characteristics of the doped Bi SAs induced by their different first-shell coordination (either carbon or nitrogen), which modify the hybridizations between the Bi center and *OCHO/*COOH intermediates, alter the energy barriers of the rate-determining steps and ultimately trigger bifurcated reaction pathways. This study demonstrates a practical and scalable ultrafast laser approach to tailoring the fine-structures and catalytic properties of supported catalysts and offers atomic-level insights into the mechanisms of CO_2RR on ligand-modified Bi SAs with potential applications in various fields.

The third part of this thesis presents the geometric tuning of the CoN8C8 motif in cobalt phthalocyanine (CoPc) through varying the radius of carbon nanotubes (CNTs) supports, revealing the underlying volcanic correlations between the magnitude of compressive deformation/curvature within CoN8C8 and its catalytic performance in CO_2RR. The optimally curved CoN8C8 boosts the turnover frequency by 2.4-fold at a potential of -0.8 V vs RHE *via* regulating the energy barrier of the rate-determining step (RDS), as supported by Tafel analysis and computational simulations. Such structural features further secure a near 4-fold CoPc mass preservation, affording a halved degradation rate in CO partial current density in the optimally strained sample in contrast to the least strained one by virtue of the slower CoPc demetallation and more efficient charge transfer.

Preface

This thesis is an original work by Mengnan Zhu (Meng-Nan Zhu) under the supervision of Dr. Jing-Li Luo.

Chapter 1 is the introduction to the background knowledge and fundamentals of electrochemical carbon dioxide reduction reactions at room temperatures and pressures.

Chapter 2 is a Review with reference to the up-to-date literature reports in electrochemical carbon dioxide reduction reactions.

Chapter 3 introduces the methodologies and characterization techniques.

Chapter 4 of this thesis has been published as Meng-Nan Zhu, Bo-Wen Zhang, Min-Rui Gao, Peng-Fei Sui, Chenyu Xu, Lu Gong, Hongbo Zeng, Karthik Shankar, Steven Bergens, Jing-Li Luo. Electrochemically reconstructed perovskite with cooperative catalytic sites for CO_2-to-formate conversion, Applied Catalysis Environmental: B, 2022, 306, 121101.

J.L.L. is responsible for project administration, supervision, funding acquisition, review and editing the manuscript. J.L.L., M.N.Z and B.W.Z conceived the work. M.N.Z synthesized the materials, performed electrochemical studies, data analysis and interpretation, the DFT analysis, and wrote the manuscript draft. B.W.Z synthesized the materials. M.R.G participated in DFT data analysis. P.F.S and C.X helped with data curation. L.G. performed the AFM analysis. H.Z, K.S and S.B reviewed and edited the manuscript.

Chapter 5 of this thesis has been published as Meng-Nan Zhu, Haoqing Jiang, Bo-Wen Zhang, Minrui Gao, Peng-Fei Sui, Renfei Feng, Karthik Shankar, Steven H. Bergens, Gary J. Cheng, and Jing-Li Luo. Nanosecond Laser confined bismuth moiety with tunable structures on graphene for carbon dioxide reduction, ACS Nano, 2023, 17, 8705−8716.

J.L.L supervised and directed the study, contributed to the funding acquisition, edited, and revised the manuscript. G.J.C directed the study, edited, and revised the manuscript. J.L.L, M.N.Z and H.J conceived the work. M.N.Z performed the DFT analysis, electrochemical studies, data analysis and interpretation, and wrote the manuscript draft. H.J contributed to the material synthesis and revised the manuscript. B.W.Z participated in electrochemical studies, XAFS data analysis and revised the manuscript. M.R.G conducted the XRD analysis. P.F.S participated in the data discussions and gave constructive comments of this work. R.F performed the synchrotron X-ray spectroscopy and gave constructive comments on XAFS data interpretation measurements. K.S and S.B gave constructive comments of this work. M.N.Z and H.J contributed equally.

Chapter 6 of this thesis, entitled Volcano-shaped Carbon Dioxide Reduction on Cobalt Phthalocyanine with Curvature Induced Atomic Spacing Regulation, is ready for submission.

J.L.L supervised and directed the study, contributed to the funding acquisition, edited, and revised the manuscript. J.L.L and M.N.Z conceived the work. M.N.Z performed the DFT analysis, electrochemical studies, data analysis and interpretation, and wrote the manuscript draft. B.W.Z contributed to the material synthesis and XAFS data analysis. S.Z performed the ICP-OES analysis. M.R.G contributed to DFT data analysis. R.F performed the synchrotron X-ray spectroscopy and

gave constructive comments on XAFS data interpretation measurements. K.S and S.B gave constructive comments of this work.

Chapter 7 of this thesis includes the summary and prospects.

Acknowledgements

In the writing of this thesis, I have incurred many debts of gratitude, too many to credit them all.

To my supervisor, Dr. Jing-Li Luo, who took a chance on an unknown student by offering me the opportunity to join her research group. Her academic and financial support since 2018 has been invaluable. Without her guidance, this thesis would simply not be possible.

To my supervisory committee members Dr. Hongbo Zeng and Dr. Hyun-Joong Chung for their valuable suggestions and guidance during my research progress. To Prof. Steven Bergens and Prof. Karthik Shankar, who provided valuable comments on the manuscript revision.

To Canada First Research Excellence Fund (CFREF) and the Future Energy Systems (FES) research institute at the University of Alberta, who supported this research financially.

To my colleague Bo-Wen Zhang for his invaluable advice and academic rigor, which has inspired me in many ways. I am also grateful to my colleague Min-Rui Gao, who taught me a lot on Density-Functional-Theory and provided me with lots of advice throughout my projects. I would like to extend my sincere gratitude to my colleagues Nanqi Duan, Zhou Chen and Jiankuan Li, who not only spent hours addressing my questions but also teamed up with me for badminton during our leisure times. I would like to acknowledge the contributions of my other colleagues, Dr. Chenyu Xu, Dr. Jing Xiao, Yuanyuan Hong, Pengfei Sui, Shaoqing Liu, and Yicheng Wang, who have been a great help to me during the past four years.

I would also like to express my heartfelt gratitude to all of my friends for their unwavering support and companionship.

And finally, to my parents, for giving me their understanding, encouragement, advice, and love throughout the duration of my study.

Table of Contents

List of Tables

List of Figures

List of Symbols

FE_x	Faradaic efficiency
I_x	Partial current density of product x
I	Total current
n	The number of electrons transferred
c_x	Concentration of product x
F	Faraday constant
V_m^{-1}	Unit molar volume at 298.15 K
V	Total volume of the electrolyte
e	1.6×10^{-19} C mol^{-1}
$\mathrm{N_A}$	Avogadro number
$\mathrm{Q_{total}}$	Total amount of charge passed through the system
j	Current density
$\mathrm{j_x}$	Partial current density toward product x
$\mathrm{j_{ECSA}}$	ECSA-normalized j
$\mathrm{j_{x-ECSA}}$	ECSA-normalized j_x
$\mathrm{C_{dl}}$	Double-layer capacitance
$\mathrm{I_a}$	Anodic charging current
$\mathrm{I_c}$	Cathodic charging current
ν	Scan rate
$\mathrm{C_{REF}}$	Capacitance of the smooth planar surface

S	Surface area of the electrodes
ω	The content of the active sites
m	Mass
M	Atomic mass
η	Overpotential
E	Applied potential
E^0	Thermodynamic equilibrium potential
G	Gibbs free energy
ΔG^0	Gibbs free energy change
E_{DFT}	DFT calculated electronic energy
E_{ZPE}	Zero-point energy
$\int C_p dT$	Enthalpy correction
TS	Entropy correction
E_b	Binding energy
$\nu_1 CO_3^{2-}$	Symmetric stretching oscillation of carbonate
U_L	Thermodynamic limiting potentials
R	Bond length
σ^2	Debye-Waller factors
ΔE_0	Inner potential correction
I_{photo}	Photocurrent

List of Abbreviations

CO_2RR	Carbon dioxide reduction reaction
BBO	$BaBiO_3$
eBBO	Electricity-induced Bi metallene from $BaBiO_3$
FA	Formic acid/Formate
FTIR	Fourier-transform infrared spectroscopy
SA	Single atom
XAS	X-ray absorption spectroscopy
CoPc	Cobalt phthalocyanine
CNTs	Carbon nanotubes
RDS	Rate-determining step
OER	Oxygen evolution reaction
GC	Gas chromatography
IC	Ion chromatography
EC	Electrochemical cell
HER	Hydrogen evolution reaction
ECSA	Electrochemically active surface area
CV	Cyclic voltammetry
OCP	Open-circuit potential
TOF	Turnover frequency
RHE	Reversible hydrogen electrode

DFT	Density Functional Theory
CHE	Computational hydrogen electrode
SERS	Surface-enhanced Raman scattering
HEAs	High entropy alloys
ORR	Oxygen reduction reaction
LCO	La_2CuO_4
SACs	Single atom-based catalysts
XANES	X-ray Absorption Near Edge Spectroscopy
EDTA	Ethylenediaminetetraacetic acid
BVO	$BiVO_4$
BVOh	H_2 treated $BiVO_4$
BVOh-FN	H_2 treated $BiVO_4$ with FeOOH and NiOOH
XRD	X-ray diffraction
FE-SEM	Field emission scanning electron microscopy
TEM	Transmission electron microscopy
XPS	X-ray photoelectron spectroscopy
EDX	Energy dispersive X-ray spectrometry
AFM	Atomic force microscope measurements
ICP-OES	Inductively coupled plasma optical emission spectrometry
LSV	Linear sweep voltammetry
VASP	Vienna Ab initio Simulation Package
BBO100	BBO reduced for 100 s

BBO500	BBO reduced for 500 s
BBO1000	BBO reduced for 1000 s
BBO3000	BBO reduced for 3000 s
BBO5000	BBO reduced for 5000 s
Bi-C	Bi SA coordinated to C
Bi-NC	Bi SA coordinated to N
CN	Coordination number
r-FE_{CO}	FE_{CO} retention
r-j_{CO}	j_{CO} retention

Chapter 1. Introduction

1.1. Overview of Carbon Dioxide Recycling

The dependence on fossil fuels and the resultant emissions of carbon dioxide (CO_2) are pressing issues in the present-day energy landscape. According to the data released by the National Oceanic and Atmospheric Administration of the US Department of Commerce, the average concentration of CO_2 in the atmosphere reached 419.47 parts per million by January 2023, which almost doubles the CO_2 level recorded during the Industrial Revolution.[1] The persistent increase in atmospheric CO_2 levels not only poses significant threats to the environment, but also results in the inefficient utilization of carbon, a vital component in fuels. In light of this, many nations, such as Canada, have pledged to achieve net-zero emissions by 2050 and are making efforts to transition to a sustainable energy system.[2]

Carbon neutrality, otherwise referred to as the net-zero CO_2 emission, entails a delicate balance between the emission and removal of CO_2 from the atmosphere. To achieve the goal, efficient carbon recycling schemes, e.g., CO_2-fuels-CO_2 loop, should be integrated to energy-intensive industries. The cornerstone of the CO_2 removal process is the reduction of captured CO_2 into value-added substances that can either be used directly as raw materials or serve as reactants in numerous chemical processes. However, the conversion of CO_2 molecules poses a significant challenge due to its chemical inertness, and cannot be achieved without the presence of an external driving force under standard temperature and pressure conditions.[3] To tackle the challenges, various man-made CO_2 conversion processes have been devised in recent years, incorporating a diversity of functional units such as solar energy, electricity, thermo, among

others. The processes aim to expedite the CO_2 recycling and the utilization process are depicted in Figure 1.1a.

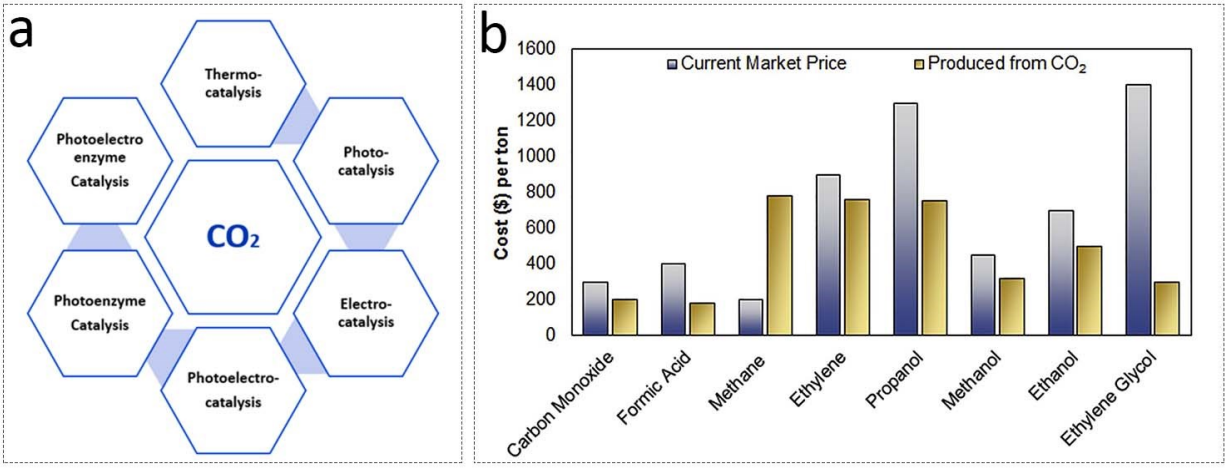

Figure 1.1 (a) CO_2 conversion strategies. (b) Comparison of the cost of various CO_2-derived chemicals between the current market price and the levelized cost from CO_2 reduction.[4] Reprinted with permission from Reference [4]. Copyright (2018) Elsevier Ltd.

The electrochemical CO_2RR technique has made rapid progress in recent years, standing out among its counterparts due to its several advantages, including mild reaction conditions such as ambient temperature and pressure and the use of aqueous-based non-toxic electrolytes. Additionally, its ability to easily control electrode potential results in the products with high activity and stability, making it suitable for large-scale implementation when integrated with renewable energy sources such as photovoltaic, biomass, and hydroelectric power. Recent techno-economic evaluations of room temperature CO_2 electrolysis conducted by several independent research groups have reached similar conclusions, reinforcing the feasibility of room temperature CO_2RR as a solution to the current carbon crisis.[4,5] In particular, the production

of CO and formic acid/formate (FA) through present-day techniques has already become commercially competitive with conventional processes. According to a reported by Shin et al., the base production costs of CO and FA are approximately US$0.44 and US$0.59 per kilogram, respectively.[5] These costs are comparable to their respective market prices of US$0.80 and US$0.50 per kilogram, thereby indicating the commercial viability of CO and FA produced *via* CO_2RR. Although the large-scale productions of high-order C2+ feedstocks for economic gain are not immediately feasible, it holds promise for the near future, provided that electricity prices continue to decrease, and energy efficiency is improved. Bushuyev and co-workers conducted a separate study, taking into account the factors such as the costs of CO_2, electricity, separation, capital/maintenance, and operation, as well as the known product selectivity (Figure 1.1b).[4] They obtained similar conclusions as Shin et al., stating that current CO_2RR technologies are already more cost-effective than traditional processes in the production of major C1 products (e.g., CO and FA), and that the continued use of low-cost, renewable electricity has the potential to further enhance the economic viability of CO_2RR. While it is acknowledged that certain scientific hurdles still persist, the roadmap for CO_2 neutralization through the utilization of CO_2RR at room temperature and pressure exhibits great promise over the long term.

1.2. Fundamentals of Carbon Dioxide Reduction Reaction (CO_2RR)

1.2.1. The working systems

CO_2 electrolysis is usually carried out in specialized electrochemical reactors that continuously convert CO_2 to fuels at the cathode side, driven by external cathodic potentials. This process is frequently paired with the oxygen evolution reaction (OER) from water splitting at the anode,

thereby completing the overall reaction of $CO_2 + H_2O \rightarrow \text{fules} + O_2$. To analyze the products obtained from CO_2RR, the cathode is directly connected to the gas chromatography (GC) spectrometer for online detection of gaseous products, while the liquid products are collected and subsequently analyzed by ion chromatography (IC). To prevent products crossover and re-oxidation during the reaction, a proton-exchange membrane (e.g., Nafion 117) is placed between the two chambers. The cathodic electrode is equipped with a reference electrode near its surface to accurately regulate the external potentials applied to the cathode. In lab-scale research, the H-type cell (Figure 1.2) has been widely adopted due to its simple cell fabrication, efficient pre-screening of the catalyst performances, and easy access to probe the reaction mechanisms when combined with advanced *in situ* spectroscopy techniques.

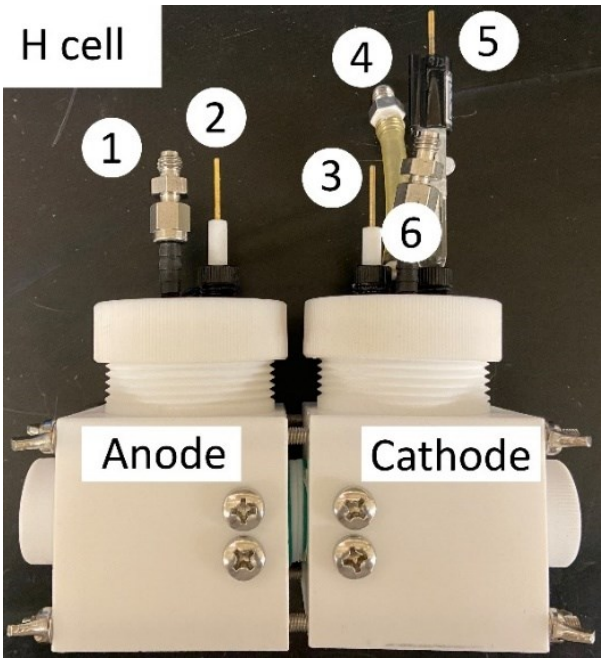

Figure 1.2 Digital image of the H-type cell used in electrochemistry studies (1. CO_2 inlet. 2. counter electrode. 3. working electrode. 4. CO_2 inlet. 5. reference electrode. 6. Connection to GC).

1.2.2. Figures of Merit for CO_2RR

- **Faradaic efficiency**

Faradaic efficiency (FE_x, x is target product) measures the fraction of the current used to generate a specific product x over the total current flowed through the system.[6,7] For a system to exhibit optimal efficiency in generating a target product, it is desirable to attain a 100% FE, meaning that all the charges flowing through the circuit will be consumed in the production of the desired product. The FE_x of gaseous product x is calculated based on Equation 1.1:

$$FE_x = \frac{I_x}{I} = \frac{n \cdot \nu_{co_2} \cdot c_x \cdot F \cdot V_m^{-1}}{I} \tag{1.1}$$

Where I_x and I stand for the partial current density of product x and the overall current flow through the system. n represents the number of electron transfer for the formation of 1 mol of x. ν_{co_2} denotes the flow rate of CO_2 feeding gas. c_x is the concentration of x . F and V_m^{-1} refer to the Faraday constant (96,485 C mol^{-1}) and unit molar volume (24.5 L mol^{-1}) at 298.15 K.

The FE_{FA} of FA is calculated based on Equation 1.2:

$$FE_{FA} = \frac{2 \cdot c_{FA} \cdot V \cdot e \cdot N_A \cdot (0.001)}{Q_{total}} \tag{1.2}$$

Where c_{FA} (mol L^{-1}) is the measured concentration of FA. V stands for the total volume of the electrolyte, which is around 30-35 mL in this study. e is 1.6 x 10^{-19} C mol^{-1}. N_A is the Avogadro number (6.02 x 10^{23}). Q_{total} represents the total amount of charge passed through the system.

- **Total current density**

Total current density (j) is the measurement of the number of electrons flowing through the electrochemical cell (EC) per unit surface area. The observed j is mainly attributed to the two simultaneous reactions, i.e., hydrogen evolution reaction (HER) and CO_2RR on the electrode surface in aqueous-based electrolytes, and thus the increase in j can not be directly translated to an increase in catalytic activities for generating product x. To distinguish the capability of electrocatalysts to drive CO_2RR and HER, the values of j obtained in both CO_2 and argon saturated electrolyte should be reported and compared.

- **Partial current density**

Partial current density of x (j_x) reflects the current density for forming product x, which is determined by multiplying the steady j and FE_x at the same potential. j_x can be used as the descriptor to evaluate the production rates/activities of the electrocatalysts. Typically, the j and j_x are normalized with respect to the geometric area of the electrode, which sometimes fail to reflect the intrinsic activity of catalyst due to the surface roughness effect.[8] Therefore, the electrochemically active surface area (ECSA)-normalized j and j_x, namely the j_{ECSA} and j_{x-ECSA} , has been employed to probe the intrinsic activity of the electrocatalysts. ECSA can be obtained by measuring the double-layer capacitance (C_{dl}) with cyclic voltammetry technique (CV) in the non-Faradaic regime, which is typically a 100 mV window centered as the open-circuit potential (OCP) based on Equations 1.3 and 1.4.[9]

$$C_{dl} = \frac{I_a - I_c}{2\nu} \tag{1.3}$$

$$ECSA = \frac{C_{dl}}{C_{REF}} \tag{1.4}$$

Where I_a and I_c is the anodic and cathodic charging current, respectively. ν represents the scan rate. C_{REF} stands for the capacitance of the reference smooth planar surface.

- **Turnover Frequency (TOF)**

Turnover frequency (TOF) is defined as the mole of products generated per electrocatalytic active sites per unit time, as shown in Equation 1.5:

$$TOF = \frac{j_x \cdot S/nF}{\omega m/M} \tag{1.5}$$

Where S is the surface area of the electrodes. ω is the content of the active sites. m is the total mass of electrocatalysts. M is the atomic mass of the active element.

- **Overpotential**

Overpotential (η) refers to the potential difference between the thermodynamic equilibrium potential of a certain reaction and the applied potential, as shown in Equation 1.6:

$$\eta = E - E^0 \tag{1.6}$$

where E and E^0 refer to the applied potential and the standard potential of the target CO_2RR reaction.

- **Stability**

The long-term durability is evaluated by assessing the values of $\mathrm{FE_x}$ and $\mathrm{j/j_x}$ of certain products periodically over the course of electrolysis. For practical applications, the service lifetime of electrodes should reach to several thousands of hours; meanwhile, the degradation rate of $\mathrm{j/j_x}$ and $\mathrm{FE_x}$ overtime should reside in a reasonable range.[10,11] In lab experiments, the stability tests are typically performed up to at least a few hours.

1.2.3. Thermodynamics of CO_2RR

The electrochemical CO_2RR are essentially multiple proton−electron reactions that result in the generation of a diverse range of carbonaceous products and water. A clear correlation exists between the external potentials applied and the electrocatalytic products in the context of CO_2RR. The standard redox potentials (E^0 V *vs* RHE, reversible hydrogen electrode) for the CO_2RR products can be calculated based on Equation 1.7 and the results are presented in Table 1.1 (all potential hereafter is referred to RHE scale unless otherwise specified).

$$\Delta G^0 = -nFE^0 \tag{1.7}$$

where ΔG^0 is the Gibbs free energy change.

Table 1.1 Equilibrium Potentials of the representative CO_2RR.[12,13]

Reaction	E^0 (V *vs* RHE)
CO_2RR	
$CO_2 + 2H^+ + 2e^- \rightarrow HCOOH_{(aq)}$	-0.20 (for pH < 4). -0.20 + 0.059 * [pH-4] (for pH > 4)
$CO_2 + 2H^+ + 2e^- \rightarrow CO_{(g)} + H_2O$	-0.11
$CO_2 + 8H^+ + 8e^- \rightarrow CH_{4(g)} + 2H_2O$	0.17
$CO_2 + 6H^+ + 6e^- \rightarrow CH_3OH_{(aq)} + H_2O$	0.03
$2CO_2 + 12H^+ + 12e^- \rightarrow C_2H_{4(g)} + 4H_2O$	0.07
$2CO_2 + 12H^+ + 12e^- \rightarrow C_2H_5OH_{(aq)} + 4H_2O$	0.08
Water splitting	
$2H_2O \rightarrow O_2 + 4H^+ + 4e^-$	1.23
$2H^+ + 2e^- \rightarrow H_2$	0

It is noteworthy that several of the reduction potentials of the CO_2RR are similar, which exacerbates the challenges of low selectivity and thus product diversity for the desired product during the CO_2RR process. Furthermore, the HER can further undermine the selectivity of CO_2RR, leading to decreased efficiency. The fact that a broad range of products can be generated indicates the presence of different reactions mechanisms as well as the branched reaction pathways on the electrocatalysts surface. Hence, fine-tuning the properties of electrocatalysts to achieve the selective and stable production of target products remains as a central objective CO_2RR research.

1.2.4. Mechanistic insights of CO_2RR

The comprehensive understanding of the mechanisms behind CO_2RR is of utmost importance to the advancement of the field. Experimental and theoretical approaches are thus indispensable in providing a thorough investigation of the complex reaction process and pathways. The application of *in situ* spectroscopy techniques offers direct evidence to the nature of reaction intermediates,[14] yet the intricacy of CO_2RR often poses limitations to the decoding of spectra. As a complementing tool, atomic-scale density-functional-theory (DFT) calculations based on the computational hydrogen electrode (CHE) model have proven to be instrumental in yielding insights into the reaction mechanisms and pathways. Within this formalism, the concerted proton-electron transfer is assumed at each elementary step. The pH and potential effects are not directly considered by DFT but can be added in a linear fashion.[15,16]

- ***Mechanisms of C1 production***

CO and FA are the simplest products of CO_2RR, requiring the transfer of only two electrons/protons to complete the reaction. In practice, large overpotentials are required to initiate these reactions because the first step to form adsorbed $*CO2^{\bullet-}$ with bended structure is both thermodynamically and kinetically limited (* stands for the adsorption site).[17] After this step, the $*CO2^{\bullet-}$ will react with H_2O to form either *COOH and *OCHO as the first protonated intermediate (Figure 1.3).[18] Feaster et al. reported that the *COOH binding energy can be used as the descriptor for the production of CO, whereas the *OCHO binding energy shows a clear correlation to the FA production.[18] To produce CO, a carbophilic catalyst is generally required to initiate the metal-C bonding and the subsequent formation of *COOH, and further protonation

of *COOH can lead to a variety of products; in contrast, the formation of *OCHO requires a oxyphilic catalyst and FA is a "dead-end" and cannot be further reduced.[19,20] These results collectively suggested that the production of CO and FA proceeds through different intermediates. In a recent work conducted by Chernyshova et al., the cutting-edge techniques including the operando surface-enhanced Raman scattering (SERS), Tafel analysis, and DFT simulations collectively confirmed that the FA and CO production on Cu proceeds through a carboxylate intermediate with the $\eta^2(C,O)-CO_2^-$ structure, which can be used as the common descriptor of the CO_2-to-CO and CO_2-to-FA.[14]

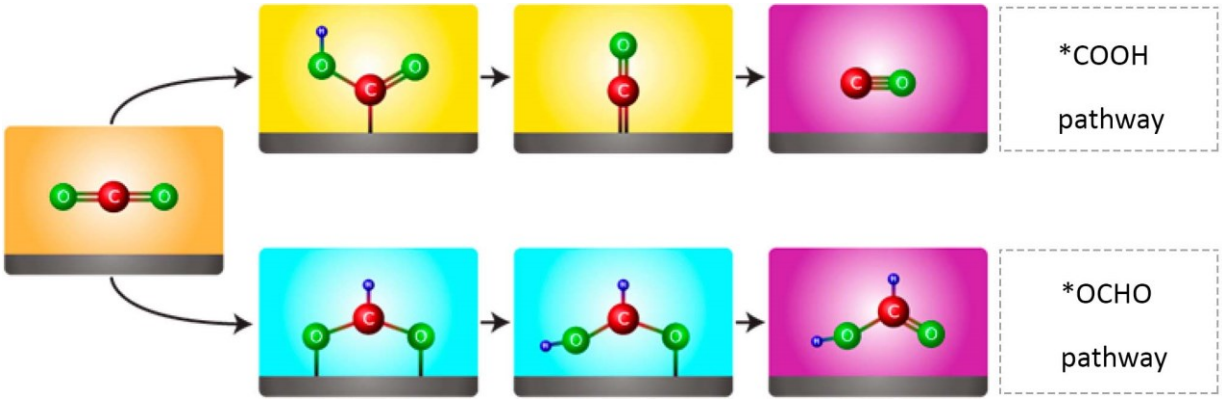

Figure 1.3 CO_2-to-CO and CO_2-to-FA reaction pathways involving two different intermediates of *COOH and *OCHO.[18] Reprinted with permission from Reference [18]. Copyright (2017) American Chemical Society.

CH_4 and CH_3OH, another two major C1 products, are preferably observed over Cu-based electrocatalysts. It has been generally accepted that the production of CH_4 undergoes two stages: the production of *CO and its further protonation. Peterson and co-workers, through DFT calculations, predicted that protonation of the *CO to *CHO is the RDS (0.39 eV), which

experiences the "*CHO-*CH2O-*CH3O-CH4" pathway (Figure 1.4, pathway a), leaving *O on the surface of electrocatalysts that is subsequently converted to H_2O. The selectivity between CH_4 over CH_3OH has been proposed to be the final reduction of *CH3O. However, their calculation results were merely based on thermodynamic analysis and the kinetics contributions were not accounted for. By explicitly incorporating the role of water alongside the kinetic analysis of each elementary step, Ni et al. further proposed a different reaction mechanism involving the formation of *COH intermediate, which requires a lower energy of 0.21 eV, and the complete pathway follows "*CO-*COH-*C-*CH-*CH2-*CH3-*CH4-CH4" (Figure 1.4, pathway b).[21] In addition, studies have shown that the protonation steps follow a Langmuir-Hinshelwood mechanism where the surface adsorbed *H directly participates in the reaction, in good agreement with the experimentally observed concerted increase/decrease in HER and CO_2-to-CH_4 reaction.

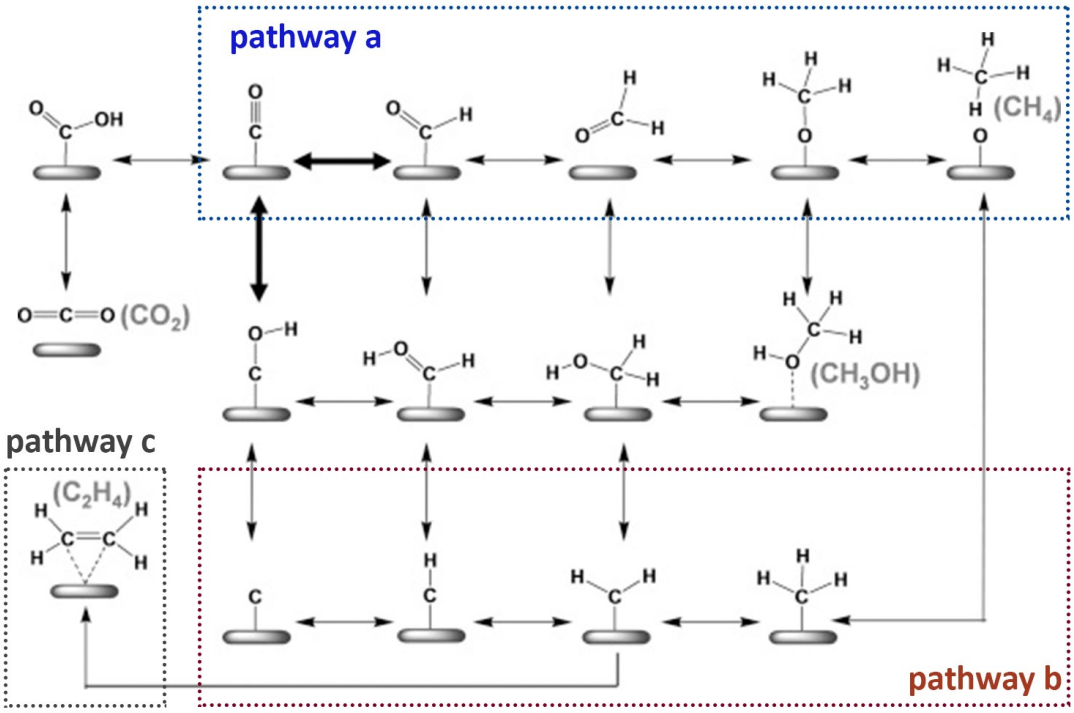

Figure 1.4 (a and b) The proposed reaction pathways for CO_2-to-CH_4. (c) The proposed reaction pathway for CO_2-to-C_2H_4.[21] Reprinted with permission from Reference [21]. Copyright (2013) WILEY-VCH Verlag GmbH & Co. KGaA, Weinheim.

- ***Mechanisms of C2+ production***

The reaction pathways of CO_2RR toward various high-order C2+ hydrocarbon/oxygenated products are even more complicated and there is currently no consensus in the research community, and yet it has been widely accepted that the production of C2+ requires the formation of C-C bonds. Some detailed mechanistic routes have been suggested, showing the bifurcated reaction pathways from the common intermediate *CO.[22] Cite C_2H_4 as an example: the formation of C_2H_4 involves the *CO dimerization with an electron transfer to render the *C2O2 as key species, followed by the subsequent protonation to produce *CO-CHO

intermediate. The final intermediate of ethenol (C_2H_4O) can be further reduced to C_2H_4 or CH_3CHO. Although the equilibrium potentials of CO_2 reduction toward hydrocarbon or alcohol products are thermodynamically more favorable than toward CO and FA, the RDS, which is the formation of C-C bonds, limits some of these reactions kinetically. This explains the experimentally observed low C2+ yield. In addition to the *CO-CO step, Ni et al. also suggested a different C_2H_4 pathways involving the coupling of *CH2-CH2 (Figure 1.4, pathway c). Overall, future studies are required to clarify the reaction mechanisms in terms of the C2+ generations.

Chapter 2. Literature Review

2.1. General Material-Function Relations in CO_2RR

Since the seminal studies by Hori et al., extensive research efforts by various research organizations have contributed to establishing a general consensus among the scientific community that there exists a clear relation between the chemical properties of metal-based electrocatalysts and the resultant yields from CO_2RR.[23] As shown in Figure 2.1a, noble metal-based electrocatalysts (mainly Ag and Au) and metal Zn are generally highly active toward CO generation. The p-blocking metal-based electrocatalysts, mainly Sn, In, Bi, Sb, etc., predominantly yield FA from CO_2RR. Cu, intriguingly, is the only metal-based catalyst capable of reducing CO_2 to hydrocarbons and oxygenates with appreciable production rates. Main group transition metals, e.g., Fe, Co, Mn, etc., are almost inert to CO_2RR but are active toward the competitive HER.[24] These experimental findings can be correlated to the distinctive metal-intermediate interactions that are characterized by the adsorption energy of a specific species. As demonstrated in Figure 2.1b, the group of metals that exhibit high production of CO (Ag and Zn) displays a relatively weak *CO binding, which tends to desorb from the catalysts' surface and form CO. Au exhibits the highest activity toward CO production, being situated at the peak of the graph. The metals on the left side of the figure (Pt and Ni) exhibit a strong binding to *CO and are prone to poisoning and deactivation. Cu presents a favorable balance of *CO adsorption energy, neither too strong nor too weak, making it a promising candidate for deep reduction of CO, as depicted in Figure 2.1c.

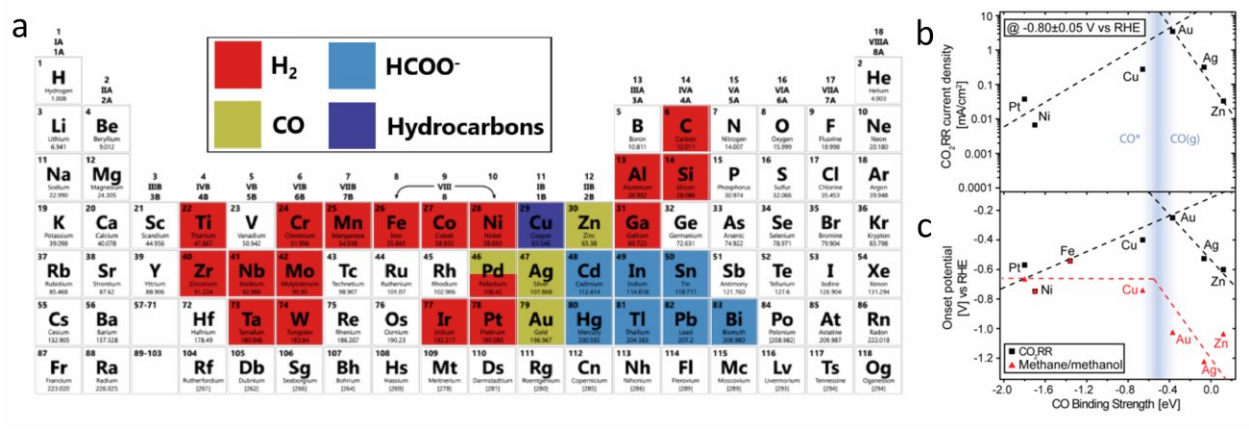

Figure 2.1 (a) Metal electrocatalysts and their major CO_2RR products.[24] Reprinted with permission from Reference [24]. Copyright (2021) Elsevier Ltd. (b, and c) Volcano plot of CO_2RR current density at −0.8 V as a function of the CO binding strength (b) and onset potentials of CO_2RR and methane/methanol as a function of the CO binding strength (c).[16] Reprinted with permission from Reference [16]. Copyright (2014) American Chemical Society.

Metal derivatives, such as metal alloys, metal (oxides/sulfides) composites, have been investigated for CO_2RR as they provide extra dimensions (e.g., electronic effect, ligand effect, etc.) in tuning the electronics features of electrocatalysts compared to the mono-component ones. Despite delivering similar product distributions for CO_2RR compared to the metals, the values of FE_x and j_x are subjected to variations based on the factors like the physiochemical properties (e.g., morphology, particle sizes, surface chemistries, etc.) of the electrocatalysts, the type of electrolyser, and testing conditions, etc. P-blocking metal-based derivatives mostly take on the similar selectivity/product distributions as their metal forms. For example, Yang et al. synthesized the $Sn_{0.80}Bi_{0.20}$ alloy that was reconstructed to Bi doped SnOx under cathodic potentials, exhibiting much enhanced FA production compared to that of the untreated SnOx samples

(Figure 2.2a-2.2c).[25] Xing et al. fabricated the Bi@Sn core–shell nanoparticles (Bi core and Sn shell) by the electroreduction of $Bi_2Sn_2O_7$ precursor.[26] The as-obtained electrocatalysts could convert CO_2 to FA with a FE_{FA} around 90% from -0.9 to -1.2 V whereas SnO_2 delivered a much lower FE_{FA} of less than 60% within the same potential range. In addition to the p-blocking metal-based materials, Cu alloys could deliver the more diverse product distributions in CO_2RR. Zhong et al., using DFT calculations in combination with active machine learning, identified the Cu-Al electrocatalysts as the excellent electrocatalysts for C_2H_4 production from a series Cu-based alloys.[27] The as-obtained Cu-Al reduced CO_2 to C_2H_4 with a high FE of over 80% at a current density of 400 mA cm^{-2} and a half-cell ethylene power conversion efficiency of 55 ± 2% at 150 mA cm^{-2}, representing the state-of-the-art electrocatalysts for CO_2-to-C_2H_4 conversion. Beyond alloys, dual-component catalysts, where a second phase is only mechanically/physically introduced without the formation of the alloy, have been investigated in a few other studies. For instance, Ag-Cu and Au-Cu based heterostructures were developed and showed promising C2+ production rates through the so-called “tandem” reaction mechanisms.[28,29] In such a tandem configuration, the CO_2 is firstly reduced to CO on Ag or Au sites, generating the microenvironment with high local CO concentrations. In this regard, the sequential CO-CO dimerization step over Cu surface would be easily initiated for enhanced C2+ products (Figure 2.2 d and 2.2e).

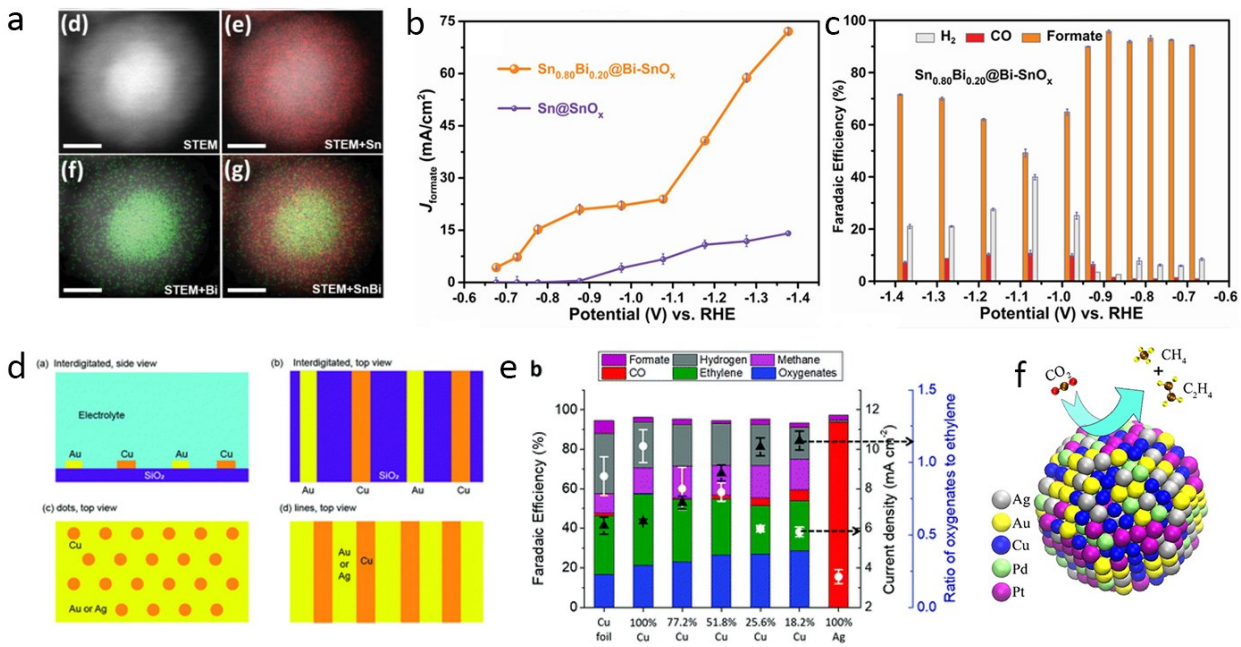

Figure 2.2 (a) EDS elemental mapping images of $Sn_{0.80}Bi_{0.20}$ alloy NPs. (b) j_{FA} of $Sn_{0.80}Bi_{0.20}$ @Bi-SnO*x* and Sn@SnO*x* nanoparticles. (c) FEs of $Sn_{0.80}Bi_{0.20}$@Bi-SnOx.[25] Reprinted with permission from Reference [25]. Copyright (2020) Wiley – VCH Verlag GmbH & Co. KGaA, Weinheim. (d) Schematics of interdigitated bimetallic electrodes in the interdigitated design. (e) FEx for Cu lines on Ag system as a function of Cu areal coverage.[28] Reprinted with permission from Reference [28]. Copyright (2017) American Chemical Society. (f) Schematic of the HEA and catalysis reaction.[30] Reprinted with permission from Reference [30]. Copyright (2020) American Chemical Society.

High entropy alloys (HEAs), composing of various different elements, have been recently applied to CO_2RR. Nellaiappan et al.[30] and Pederson et al.[31] independently reported the AuAgPtPdCu HEAs for CO_2RR, based on the joint of experimental results and theoretical simulations. According to the findings of Nellaiappan et al., the electrocatalytic activity of AuAgPtPdCu was

predominated by the redox-active Cu species (Cu^{2+}/Cu^0) and the other metals only contributed synergistically. As a result, a 100% conversion of CO_2 to gaseous products could be achieved at a low voltage of -0.3 V (Figure 2.2f). Pederson et al. applied DFT methods with supervised machine learning to predict the *CO and *H adsorption energy of all sites in the (111) facet of disordered CoCuGaNiZn and AgAuCuPdPt HEAs, thereby identifying the locally optimal HEAs for CO_2RR. In addition to these efforts, Li and colleagues recently developed the HEAs aerogels with the enrichment of p-blocking metals, and the optimal sample was identified as PdCuAuAgBiIn. On this specific catalyst, FA was the predominant product, achieving a maximum $\mathrm{FE_{FA}}$ of 98.1% at -1.1 V.[32] The selective FA production was ascribed to the strong interactions between different metal species and the presence of abundant surface unsaturated sites.

2.2. Perovskites- based Electrocatalysts

Perovskites are a family of organic and inorganic materials possessing similar crystal structures of ABX_3. In general, the A-site elements in a perovskite are comprised of rare earth or alkali metal ions, while the B-sites are occupied by transition metals such as Fe, Ni, Co, Mn, among others, which typically possess smaller radius than A-site elements. X generally represents O, F, or halide elements. The ideal ABO_3 structures could be depicted as a continuous network of corner-sharing BO_6 octahedral, with A occupying the cubo-octahedral voids (Figure 2.3a). The versatility and flexibility of the A-site and B-site combinations, including their types and ratios, render perovskites highly promising candidates for a multitude of redox processes, such as oxygen reduction reaction (ORR), OER and HER. It has been widely recognized that the B-site elements in perovskites play a crucial role in dictating the catalytic outcomes, thereby providing a

fundamental guideline for selecting appropriate perovskites to initiate CO_2RR. In a recent study, Pi et al. applied $SrSnO_3$ nanowires to convert CO_2 to FA, showcasing an appreciable FE_{FA} > 75% over a broad potential range from -1.1 V to -1.3 V and the highest j_{FA} of 21.6 mA cm^{-2} at -1.3 V.[33] The catalytic outcomes of $SrSnO_3$ are invariably dictated by the Sn ions as Sr is almost inert toward CO_2RR, however, whether $SrSnO_3$ is intrinsically more active than SnO_2 in the context of CO_2RR remains underexplored (Figure 2.3b). Zhu et al. reported a $LaInO_3$ perovskite for FA production, reaching the maximum FE_{FA} of 91.4% along with a j_{FA} of 106.8 mA cm^{-2} at -0.9 V.[34] In addition to Sn- and In-based perovskites, Yan et al. demonstrated that a near-unity FA selectivity can be acquired on $YbBiO_3$ perovskite at -0.9 V, as well as a wide potential window range with FE_{FA} > 90% from -0.8 to -1.2 V.[35]

Cu-based perovskites, particularly La_2CuO_4 (LCO) with the tetragonal layered K_2NiF_4 structure, have been shown to be able to catalyze multi-electron transfer reactions in CO_2RR with a variety of products beyond CO and FA. In early studies, researchers adopted La_2CuO_4 as the cathodes on the belief that it would maintain the high oxidation states of Cu^{2+}/Cu^{+} during CO_2RR electrolysis, which are crucial to produce C2+ products. Schwart et al. showed that CO_2 could be reduced to CH_3OH, C_2H_5OH, and n-propanol up to = 40% at current density of 180 mA cm^{-2} on $La_{1.8}Sr_{0.2}CuO_4$ using a flow cell device.[36] Mignard et al. performed CO_2RR over the same $La_{1.8}Sr_{0.2}CuO_4$ with similar device setup and operating environment, but the electrocatalysts variably yielded CH_4 and C_2H_4 as the major products and only a negligible amount of C_2H_5OH had been detected.[37] A few other studies reported similar product distributions over LCO-based electrocatalysts with hydrocarbons being the major products of CO_2RR. For instance, Chen et al. reported that La_2CuO_4 underwent structural transformation to form the Cu/La_2CuO_4 heterostructures under extreme

cathodic potentials; such unique interface accounted for the observed CO_2-to-CH_4 conversion with a high FE_{CH_4} of 56.3% alongside a j_{CH_4} of 117 mA cm^{-2} for CH_4 production at an external potential of −1.4 V (Figure 2.3c).[38] Wang et al. demonstrated good C_2H_4 selectivity ($FE_{C_2H_4}$ ~ 60%) over nano-bamboo LCO with rich twin boundaries synthesized from electrospinning. Furthermore, in situ XAS revealed that the Cu^{2+} was well maintained during the catalytic process. Recently, Zhu et al. investigated the effect of A-site deficiency on the CO_2RR performances and unveiled a volcano-type "A deficiency – performance" relation, where $L_{1.9}CuO_{4-x}$ exhibited the optimal current density (51.3 mA cm^{-2}) and selectivity ($FE_{C_2H_4}$ ~ 51.4%) for C2+ products, and yet $L_{1.7}CuO_{4-x}$ favours CH_4.[39] The non-stoichiometry induced tunable oxygen vacancies and/or the formation of CuO/Ruddlesden-Popper hybrids are considered the main contributors to the tunable selectivity in LCO.

Given the cathodic operating potential inherent to CO_2RR, the B-site elements reduction to low-valence phases during electrolysis appears unavoidable. The initial reduction of perovskite can pose stabilities issues, rendering the $\mathrm{FE_x}$ / $\mathrm{j_x}$ obtained during this period unreliable. As demonstrated by a study conducted by Whittingham et al., LCO remained functionally stable within the voltage ranges between -0.4 - 1.1 V, but further decreasing the voltage down below -0.4 V led to amorphization of the LCO structures.[40] Singh et al. revisited the structural evolution of LCO and showed that it underwent dissociation to La_2O_3 and Cu_2O under relatively mild cathodic potentials, and further disintegrated to metallic Cu at even more negative potentials below -0.5 V.[41]

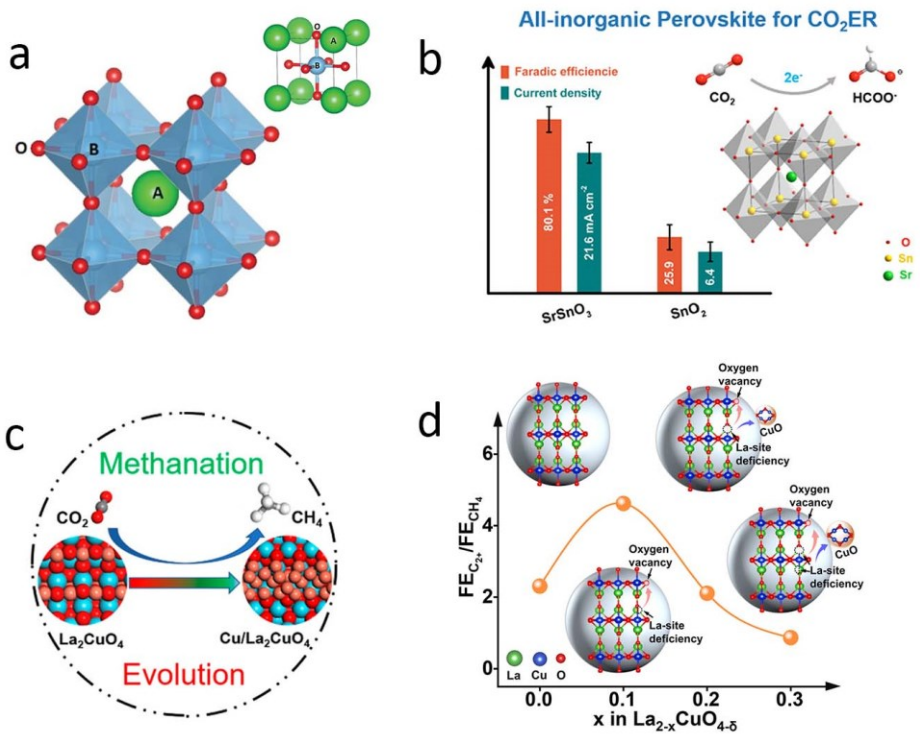

Figure 2.3 (a) Illustrations of the ABX_3 structures of perovskite.[43] Reprinted with permission from Reference [43]. Copyright (2020) Wiley - VCH Verlag GmbH & Co. KGaA, Weinheim. (b) Comparisons of the FE_x and current densities in $SrSnO_3$ and SnO_2.[33] Reprinted with permission from Reference [33]. Copyright (2019) Elsevier Ltd. (c) Schematic illustration of the transformation from LCO to form the Cu/La_2CuO_4.[38] Reprinted with permission from Reference [38]. Copyright (2020) American Chemical Society. (d) Correlations between the A-site deficiency in LCO and $FE_{C_{2+}}/FE_{CH_4}$.[39] Reprinted with permission from Reference [39]. Copyright (2021) Wiley - VCH GmbH.

In addition to La_2CuO_4, a Ca_2CuO_3 perovskite oxide with undercoordinated Cu sites generated due to partial Ca^{2+} release and strong basic strength endowed by A site, delivering a high j_{CH_4} of 517 ± 23 mA cm^{-2} as the potential of -0.3 V. DFT calculations suggested that the hydrogenation

of *CO and *CHO at the undercoordinated Cu sties was more easier, thus enabling the high CH_4 production rates.[42] Until now, the potential-induced reconstructions of perovskites remain largely under-researched, and further in-depth examination is required to determine the potential benefits of this effect on CO_2RR.

2.3. Single Atom-based Electrocatalysts

Atomic metal ions supported by substrates demonstrate great potentials in heterogeneous catalysis due to their unique chemical environment and potentially maximum atom efficiency, which opens a new horizon of possibilities in the field.[44] Previous studies have engineered the type of central metal atom to steer the production distributions, which can be readily achieved through the manipulation of the precursor metal ions during the manufacturing process. Carbon supported Ni,[45,46] Fe,[47–49] Co,[50] and Mn-based[51,52] single-atom-based catalysts (SACs) coordinated by nitrogen atoms have been shown to exhibit favourable CO generation, in stark contrast to the bulk forms of these materials, which primarily display activity toward HER. A comprehensive analysis conduced by Ju et al. demonstrated that Fe-N-C and Ni-N-C electrocatalysts, among a series of catalyst materials composed of MNx moieties (M= Mn, Fe, Co, Ni, Cu), rival traditional Au- and Ag-based electrocatalysts in terms of the intrinsic catalytic reactivity, turnover frequency, and $\mathrm{FE_{CO}}$.[53] Park et al. used DFT-based calculations to evaluate the potentials of 23 SACs, each possessing an "M-N-C" structure, for CO_2-to-CO reaction. Fe-N-C, Co-N-C and Ni-N-C were identified as highly promising transition metal-based SACs candidates based on the critical performance metrics, including the maximum reaction energy, differences in the *H and *CO binding energy (ΔG*H−ΔG*CO), and *CO desorption energy (ΔG*CO→CO).[54] More recently, p-

blocking metal-based SACs, including Sn-N4,[55,56] In-N4,[57–60] and Sb-N4,[61,62] have draw attention due to their capability in delivering both FA and CO (Figure 2.4b-2.4d). In addition to basic products requiring the transfer of two electrons, a more diverse array of products, including CH_3OH, CH_4,[63] C_2H_4,[63,64] CH_3COCH_3,[65] etc., has been observed on Cu-based SACs. However, these catalysts display a much lower efficiency for the production of higher-order C2+ species compared to their bulk counterparts, primarily due to the low concentrations of Cu centers and the increased distances between adjacent Cu centers, which retard the *CO-CO dimerization. It is noteworthy that several studies have reported the dynamic formation of Cu aggregation under operando CO_2RR studies,[66,67] leading to the identification of Cu clusters, rather than Cu SAs, as the true active centers. Xu et al. reported a Cu SAC for CO_2-to-ethanol conversion, during which the Cu SAs could transform to Cu_n clusters (n = 3 and 4), as evidenced by the leftward shifts in the operando Cu k-edge X-ray Absorption Near Edge Spectroscopy (XANES) spectra (Figure 2.4e).[66] DFT calculations collectively revealed that the reactions are most possibly carried out over Cu clusters (Figure 2.4f). The formation of Cu clusters (Cu < 4 atoms) has also been identified in Cu-in-Ag alloy system (about 1 atomic per cent of Cu) when applied to CO reduction.[68] Bai et al., through DFT simulations, predicted that the adsorption of H acts as a critical step driving the leaching of Cu atoms from the graphene lattice. Such process would accelerate at more negative potentials where stronger H adsorption took place.[69] The leached Cu atoms would aggregate and redisperse on the graphene surface, functioning as the true active centers dictating the catalytic outcomes. Therefore, further studies are imperative to examine the structural reconstruction of Cu SACs under cathodically relevant potentials and to gain a deeper understanding of the structure-performance relationships of SACs under *in situ* conditions.

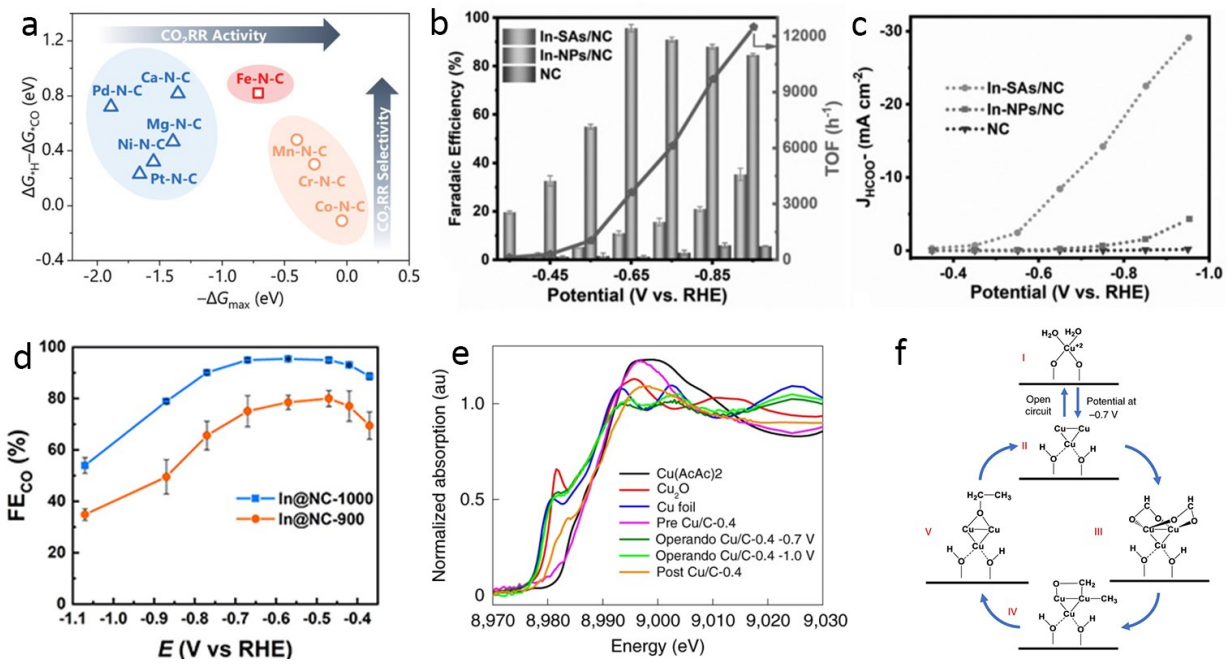

Figure 2.4 (a) The difference in *CO and *H binding energy (ΔG*H−ΔG*CO) versus the maximum CO_2RR reaction energy (−ΔGmax).[54] Reprinted with permission from Reference [54]. Copyright (2021) Wiley-VCH GmbH. (b) FEs and TOF of FA at different potentials for In-SAs/NC, In-NPs/NC, and NC. (c) j_{FA} at different potentials for In-SAs/NC, In-NPs/NC, and NC.[70] Reprinted with permission from Reference [70]. Copyright (2020) Wiley - VCH GmbH. (d) $\mathrm{FE_{CO}}$ of In@NC-1000 and In@NC-900.[60] Reprinted with permission from Reference [60]. Copyright (2022) American Chemical Society. (e) In situ Cu k-edge XANES spectra of pre Cu/C-0.4, Cu/C-0.4 at −0.7 V and −1.0 V vs RHE and post Cu/C-0.4.[66] (f) The hypothesized reaction mechanism suggested by the operando measurements.[66] Reprinted with permission from Reference [66]. Copyright (2020) Springer Nature.

Beyond the atom identity, the modulation of ligand functionality, including the number and type of coordinated atoms, can also change the bonding configuration and the electron distributions

of the active sites, which in turn influence the adsorption and activation of the CO_2 molecule and intermediates. In an effort to enhance the electrocatalytic performance and stability of SACs, early investigations primarily centered around understanding the M-N4 pyramidal structures with a symmetrical nitrogen coordination environment due to the simplicity of the structure and ease of synthesis. However, as the field has progressed, a plethora of studies have been carried out to investigate the impact of asymmetrical and/or non-nitrogen coordination environments on the M-Nx structures and their effects on the CO_2RR. Pan et al. exploited the Co-N4 and Co-N5 with different coordination number and found that Co-N5 exhibited superior CO_2RR performances with $\mathrm{FE_{CO}}$ of 99.2% and 99.4% at -0.73 and -0.79 V, respectively, equivalent to a 15.5-fold enhancement of Co-N4 in activity.[50] Ni et al. fabricated a Sn-C2O2F SACs which actively converted CO_2 to CO with a $\mathrm{FE_{CO}}$ > 90.0% over a potential window from -0.2 to - -0.6 V, in contrast to the Sn-N4 where FA was identified as the major product.[55] DFT calculations indicated that C/O coordination regulates the adsorption of intermediates, resulting the RDS shift from *CO desorption on Sn-N4 to the *CO2 activation on Sn-C2O2 and Sn-C2O2F, thereby changing the selectivity of CO_2RR. Lakshmanan et al. recently reported an unique Fe SACs configuration where the central Fe atom is surrounded by three -SO_3 groups via the oxygen atoms in Nafion coated functionalized multi-wall carbon nanotubes (Fe-n-f-CNTs), as shown in Figure 2.5.[71] Interestingly, the as-obtained Fe-n-f-CNTs achieved a high $\mathrm{FE_{C_2H_5OH}}$ of 45% and a production rate of 56.42 μmol cm^{-2} h^{-1} at -0.8 V. The near +3 oxidation states of Fe and the unique catalytic features induced by oxygen coordination collectively contributed to the high yields of C_2H_5OH. Li et al. synthesized the P,N co-coordinated Fe SACs (Fe−N/P−C) on commercial carbon black, which demonstrated enhanced activity and stability toward CO_2RR compared to the N coordinated Fe

SACs (Fe-N-C).[48] *Ex situ* XAS analyses of Fe−N/P−C and Fe-N-C before and after CO_2 electrolysis suggest the more severe Fe clustering in the latter sample, which indicates that the P,N co-coordinated Fe is more resilient toward aggregation. Therefore, the coordination-tunning strategy presents a general approach to regulating the intrinsic activities of the metal center and can be more broadly applied to other electrochemical processes.

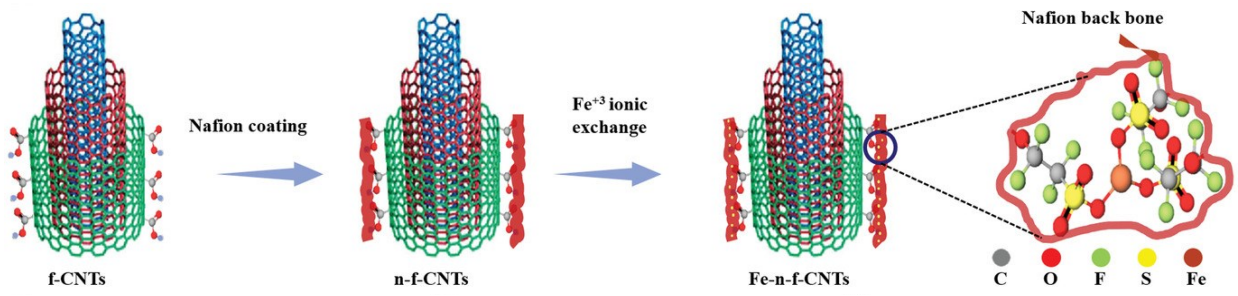

Figure 2.5 Graphical illustration of the synthesis process of Fe-n-f-CNTs.[71] Reprinted with permission from Reference [71]. Copyright (2022) Wile - VCH GmbH.

An interesting phenomenon worth mentioning is the reported variability in CO_2RR performance over SACs that possess identical coordinating atoms. This suggests that the activity of these SACs is not only determined by the metal/ligand pairing but may also rise from the overarching microstructures of these SACs. Through DFT simulations, Zhu et al. predicted a curvature-dependent CO_2RR selectivity using cobalt porphyrin nanotubes with various radius of 2.93/2.42 (CoPrNT-2), 4.17 (CoPrNT-3) and 5.25 (CoPrNT-4) Å. The simulated results showed that CO_2-to-CO could be readily initiated on the catalyst with larger diameters, while the high curved nanotubes with smaller radii would preferably enable further CO hydrogenation to CH_4.[72] Xiong et al. synthesized Ni-N4 single atom structures on a series of carbon shell with different shell thickness.[73] They found that the electrocatalysts displayed the highest CO selectivity when the

Ni-N4 was loaded on 12 nm shell (thinnest). Hao et al. reported that Zn SACs anchored on the highly curved carbon nano-onions (CNO) support displayed much higher CO_2RR activity compared to the ones on two-dimensional planar graphene substrate, which was ascribed to the reduced thickness of electrochemical double layer and stronger electric field strength on the surface of the former Zn SACs.[74] Zhang and colleagues reported that the atomically dispersed Sn on the tensile-strained ZnO nanosheets demonstrated enhanced activity and selectivity in comparison to ZnO in terms of CO_2-to-FA conversions.[75] These studies point to the critical roles of the geometric structures in dictating the CO_2RR, which remain less explored in SACs for CO_2RR.

2.4. Current Status and Remaining Challenges

In the past decades, tremendous efforts have been devoted to CO_2RR research which represents one the most promising solutions to the ultimate carbon neutrality. The enrichment of commercially available electrocatalysts that are low-cost, high active and durable remain as the prioritized work aimed at the enhancement of CO_2RR technology on a broad scale. The prevalent methods of material development are primarily predicated on a process of repeated experimentation that follows a trail-and-error approach, while a deeper understanding of the underlying principles dictating their effectiveness remains inadequately explored. In this regard, elucidating the correlations between structure and performance of electrocatalysts is a paramount aspect of research and requires further investigations.

In order to address these challenges, the objectives of this thesis are outlined into two major segments as follows. First, for practical applications, it is crucial to design low-cost catalysts with facile synthesis procedures. Perovskites, which offer tunable A-site and B-site combinations,

present significant opportunities for regulating the selectivity and activity of CO_2RR. In addition, perovskites can be prepared using versatile methods, including the widely used and straightforward "sol-gel" approach, enabling the large-scale production of perovskite powders. However, the systematic investigations into the application of perovskites for room temperature CO_2RR has been lacking, and one crucial aspect that remains unexplored is how the evolved perovskite structure influences performance and stability under cathodic reductions relevant to CO_2RR. To fill the gap, the structure-performance relations in a representative perovskite, $BaBiO_3$ (BBO), are to be systematically explored in this thesis. Under cathodic potentials, the structural evolution during electrolysis and the catalytic roles of both A-site and B-site elements are investigated to shed lights on the utilization of perovskites in room-temperature CO_2RR. Moreover, the cooperative catalytic scheme of A- and B- sites has been proposed to enhance the formate production *via* distinct mechanisms. The conclusions drawn from these studies can serve as valuable guidance in designing other potential perovskite systems for highly active CO_2.

To enhance the cost-effectiveness and atom utilization of catalysts, there is a growing interest in downsizing nano-bulk materials to an extreme extent where all metal atoms are discretely embedded in a certain matrix. This involves exposing only a single active atom to the reactants. In the ideal scenario, the atomic utilization efficiency would be maximized, as inactive atoms are eliminated, and all catalytically active sites are effectively utilized. The structure-performance of SACs, especially the coordination effects and the geometry effects, are to be studied on two representative SACs including Bi SACs and Co SACs. The coordination effects are to be examined on a series of Bi SACs, owing to the capabilities of p-blocking metal-based materials to catalyze both CO and FA production. In terms of the geometry effects, Co SACs anchored on curved CNT

substrates will be adopted as model electrocatalysts. These catalysts hold significant promise for advancing the field of catalysis and opening up new opportunities for sustainable and efficient chemical processes.

Chapter 3. Experimental Methodologies

3.1. Materials Synthesis

3.1.1. Sol-gel synthesis of $BaBiO_3$ (BBO)

BBO powder was prepared by a facile sol−gel method. Stoichiometric amounts of $Ba(NO_3)_2$ and $Bi(NO_3)_3{\cdot}5H_2O$ were firstly dissolved in 300 mL deionized water and then, nitric acid was introduced dropwise until $Bi(NO_3)_3{\cdot}5H_2O$ was completely dissolved. Afterwards, ethylenediaminetetraacetic acid (EDTA) and citric acid were added (the molar ratio of EDTA and citric acid to total metal ions was set as 1:2:1), and the pH of the solution was adjusted to be around 7 by $NH_3{\cdot}H_2O$. The precursor solution was slowly evaporated on a hot plate to yield viscous gel which further underwent a self-combustion reaction. Finally, the obtained powder was annealed at 850 °C for 4 h in air, and the as-obtained powder was further ball milled in ethanol for 6 hours to achieve smaller particle size distribution.

3.1.2. Synthesis of BVOh-FN photoanode

Nanoporous $BiVO_4$ (BVO) photoanode was prepared according to the pioneering work by Kim and Choi with slight modifications.[76] Briefly, 0.73 g $Bi(NO_3)_3{\cdot}5H_2O$ was dissolved in 50 mL 0.4 M KI solution, and its pH was adjusted to ~ 1.7 by HNO_3. The precursor was further mixed with a separate ethanol solution (20 mL) containing 0.23 M p-benzoquinone and stirred for 5 mins to form the BiOI deposition precursor solution. To obtain BiOI nanosheets, a piece of clean FTO (2 * 3 cm^2), Pt foil and Ag/AgCl (sat.) electrode were employed as the working, counter, and reference electrodes, respectively. The potential was kept at - 0.1 V vs Ag/AgCl for 10 - 12 minutes to deposit BiOI. To convert BiOI to $BiVO_4$, 0.6 mL of 0.2 M $VO(acac)_2$ dissolved in dimethyl sulfoxide was

pipetted onto BiOI, which was further annealed at 450 °C for 2 hours at a ramping rate of 2 °C min^{-1}. Afterwards, the as-obtained material was soaked in 1.0 M KOH for 30 mins to remove excess V_2O_5. Finally, the BVO substrate was dried and annealed at 270 °C at a ramping rate of 2 °C min^{-1} in Ar/H_2(5%) for 20 minutes to generate excessive oxygen vacancies (BVOh). FeOOH and NiOOH co-catalyst layer was further deposited on BVOh to enhance water oxidation kinetics. FeOOH thin layer was photo-deposited onto $BiVO_4$ from a 0.1 M $FeSO_4$ solution. To assist photo-deposition, an external bias of 0.3 V vs Ag/AgCl was applied. The deposition proceeded for 20 mins prior to increasing the potential to 1.2 V vs Ag/AgCl and maintained there for another 1 min. Subsequently, NiOOH was photo-deposited from a 0.1 M $NiSO_4$ solution (pH ~ 7) with an external potential of 0.11 V vs Ag/AgCl for 15 mins, followed by a sequential electrodeposition of NiOOH at 1.2 V vs Ag/AgCl for 1 min. The as-prepared samples are denoted as BVOh-FN. The BVOh-FN photoelectrode was washed with deionized water, and naturally dried overnight.

3.1.3. Synthesis of Bi-C and Bi-NC

- ***Synthesis of nitrogen-doped reduced graphene:***

N doped rGO was synthesized by annealing the rGO and dicyandiamide mixture (in a mass ratio of 1:10) at 900 °C in argon flow for 1 h at a ramping rate of 2 °C min^{-1}. After cooling down naturally in the argon flow, the nitrogen doped graphene powder was obtained.

- ***Synthesis of Bi-C and Bi-NC:***

The synthesis of Bi-based SACs was achieved by a three-step synthesis process including **(i)**. precursor powder preparation, **(ii)**. laser irradiation process, and **(iii)**. the final acid refluxing treatment.

(i). The precursor powder was obtained by dispersing 20 mg of rGO/NrGO to the 10 mL of ethanol solution containing 4mM of $Bi(NO_3)_3{\cdot}5H_2O$ or $BiCl_3$ salts, and the dispersion solution was subsequently subjected to constant ultrasound treatment for 20 min. The obtained mixture was then dried and degassed under vacuum at room temperature overnight. Finally, the powdery precursor was obtained and preserved in a vacuum oven.

(ii). The Bi ions/graphene complex was subjected to pulsed laser irradiation, and the details are described as follows:

<u>Sample preparation</u>: 50 mg of the powdery precursor was loaded in a glass vial with a volume of 20 ml and then covered by a glass slide on the opening from which laser pulses were penetrated through.

<u>Laser system setup</u>: the nanosecond pulse laser was operated at a wavelength of 1064 nm and pulse duration of 5 ns (Nd:YAG, Surelite III Q-switch, Continuum). Three reflective mirrors and a focus lens were used to reflect and focus the laser beam. The reflective mirrors changed the laser pulse direction from horizontal to vertical and thus, the laser beam passed through the focus lens and irradiated into the opening of the vial containing precursors. The spot size of the laser beam could be adjusted by changing the distance between the focus lens and the glass vial. In a typical

procedure, the spot size of the laser beam was 5 mm, and the laser pulse energy was 620 mJ to produce a power density of 0.64 GW cm^{-2}. For a typical experiment, 50 laser pulses were used to convert 50 mg precursor.

Laser processing: in the typical laser treatment, the glass vial containing the precursor was placed under the focus lens. The laser pulses were delivered to the precursors automatically with a frequency of 2 Hz. Once the laser contacted the precursor, a bright light was observed along with floating black smoke saturated across the whole vial. The light was caused by the plasma plume and the black smoke was generated by the powdery precursor thrusted by the ejection of plasma from the precursor during laser irradiation. In the optimized protocol for the synthesis Bi SACs, the laser irradiation dose was 1 pule per mg of the precursor. After laser treatment, the obtained product was soaked 3 times in fresh ethanol to dissolve residual metal salts. The final product was obtained by vacuum drying overnight at room temperature.

The overall ultrafast laser-based method can be concluded as follows: initially, laser photons were absorbed by both the carbonaceous support and metal ions, resulting in the generation of electrons. High-temperature conditions were achieved simultaneously, leading to the reduction, and etching of the carbonaceous support. The laser-induced plume, characterized by localized high temperature and a reductive atmosphere, effectively reduces the metal ions, enabling the entire process to be conducted in ambient air. Following this, the reduced metal atoms were rapidly cooled upon laser irradiation, embedding into the defect sites of the carbon support. This laser-induced ultrafast reduction and cooling process occurs within nanoseconds, facilitating the swift reduction of metal salts and the formation of highly enriched Bi SACs with wide distribution

on the supports. Importantly, the non-contact nature of laser interaction makes this method particularly suitable for processing powdery precursors, which aligns well with modern industrial fabrication practices with significant cost reduction.

(iii). To obtain the final Bi SACs, the as-obtained powder was washed with 0.5 M H_2SO_4 three times to remove the Bi-based nanoclusters.

3.1.4. Synthesis of CoPc-CNTx

- ***Synthesis of acid functionalized CNTs***

CNTs with various radii (XFNANO Materials Tech Co., Ltd) were annealed in air at 450 – 500 °C for 5 h in air to oxidize the amorphous carbon layer, followed by acid wash (5% w/w HCl) to remove the Ni reside. 150 mg of the pre-annealed CNTs powder was dispersed in 15 mL of concentrated H_2SO_4, following the slow addition of 5 mL of concentrated HNO_3 with mild magnetic agitation to improve hydrophilicity. The CNTs suspension was cooled down naturally and washed extensively with deionized water until the pH of the suspension approached 7. The powder was freeze-dried overnight.

- ***Synthesis of CoPc-CNTx***

The synthesis of CoPc-CNTx was based on the previous report with slight modifications.[77] In details, 20 mg of the functionalized CNTs powder was dispersed in 20 mL of dimethylformamide solution and sonicated for 30 mins to achieve homogenous distributions. 10 mL of the CoPc stock solution (0.12 mg mL^{-1}) was then added dropwise to the CNTs suspension and sonicated for 30

mins, followed by magnetic stirring for another 24 h to allow complete CoPc-CNTx hybridization. The CoPc-CNTx was then filtered with polypropylene membrane and washed with dimethylformamide two times and ethanol one time. The as-obtained powder was dried in a vacuum oven overnight to yield the final products. The synthesis of CoPc-rGO follows the same protocols but replacing the CNTs powder with graphene nanosheets.

3.2. Physical Characterizations

To study the physicochemical properties of materials, the following characterization techniques were adopted:

- **X-ray Diffraction (XRD)**: The X-ray diffraction (XRD) analysis was acquired on a Rigaku Ultima IV equipped with a Cu-K_α radiation source (Kα = 1.540598 Å) operating at 40 kV and 44 mA with a scan speed of 8° min^{-1}. The XRD data was deconvoluted by Jade Software.
- **Field Emission Scanning Electron Microscopy (FE-SEM)**: the microstructures of the materials were recorded using the Zeiss Sigma FE-SEM configured with in-lens secondary electron detector and a backscatter detector.
- **Transmission Electron Microscopy (TEM)**: the TEM images were acquired using the JEOL JEM-ARM200CF, which is a probe aberration corrected S/TEM (scanning TEM) with a cold field emission gun at 200 kV. Energy dispersive X-ray spectrometry (EDX) elemental mapping and aberration-corrected high angle annular dark field scanning transmission electron microscopy (AC-HAADF-STEM) was also acquired using JEOL JEM-ARM200CF.

- **X-ray photoelectron spectroscopy (XPS):** the XPS analysis was performed on a Krato AXIS Ultra with the carbon C 1s at the binding energy of 284.8 eV as the calibration. The XPS data were analyzed using CasaXPS.[78]
- **Fourier-transform infrared spectroscopy (FTIR)**: FTIR was performed on the Nicolet 8700 Fourier Transform Infrared Spectrometer equipped with an in situ cell with constant CO_2/H_2 flow (CO_2: H_2 = 0.2 : 20 sccm) during signal collections.
- **Raman**: Raman spectroscopy was conducted on the Renishaw inVia Qontor Confocal Raman Microscope with a laser wavelength of 532 nm. Surface-enhanced Raman spectroscopy (SERS) was conducted by dipping materials onto the Au-based SERS substrates (Ocean Insight).
- **Atomic force microscope measurements (AFM):** suitable amounts of the ethanol suspension of electrocatalysts were deposited on a clean silicon wafer. The MFP-3D-Bio AFM system (Asylum Research, Santa Barbara, CA) was exploited to characterize the thickness of electrocatalysts.
- **X-ray absorption spectroscopy (XAFS)**: The XAFS data were collected at VESPERS, Canadian Light Source. The data were processed using Demeter software package.[79]
- **Inductively Coupled Plasma Optical Emission spectroscopy (ICP-OES):** The samples were digested, and the ions concentrations were measured by Thermo iCAP6300 Duo (N. America) inductively coupled plasma-optical emission spectrometer.

3.3. Electrochemical Characterizations

3.3.1. Electrolyser setup

The electrolyser used in the experiments of this thesis is a customized gas-tight two-compartment H-cell in a three-electrode configuration. The anode and cathode compartments were separated by a piece of activated proton-exchange Nafion 117 membrane. The catalyst ink was prepared by dispersing the suitable amount of catalyst powder in the homogeneous solution containing ethanol/water mixture, with the addition of Nafion solution (5 wt%, Sigma-Aldrich) to enhance the viscosity. The ink was subjected to ultrasonic treatment for at least 1h before usage. The as-prepared ink was pipetted onto carbon paper to achieve desirable loading mass (c.a. 0.04 – 0.1 mg cm^{-2}). A graphite rod and the Ag/AgCl (sat.) electrode were employed as the counter and reference electrodes, respectively. Prior to the start of electrolysis, CO_2 was fed to electrolyte until saturated (around 30 mins). During the experiment, the flow rate of CO_2 was fixated at 20 mL min^{-1}. The CO_2 saturated 0.1 M and 0.5 M $KHCO_3$ electrolyte have the pH of 6.8 and 7.4, respectively.

3.3.2. Electrochemical analysis

Linear sweep voltammetry (LSV) polarization curves and the CV scans were obtained in CO_2 and/or Ar saturated $KHCO_3$ electrolyte. Gaseous and liquidous products were analyzed using the Agilent 6890 N GC and Metrohm 850 Professional IC Cation–HP-Gradient IC, respectively, as described in section 1.2.2. All potentials reported in aqueous electrolytes were converted to the RHE scale: $\mathrm{E_{RHE}(V)} = \mathrm{E_{Ag/AgCl}(V)} + 0.059 * \mathrm{pH} + 0.197$. All electrochemical studies were performed on Autolab worksation unless otherwise specified. Electrochemical Impedance

Spectroscopy (EIS) was performed in 10^5 – 0.1 Hz. The EIS data was fitted using suitable equivalent circuits.

3.4. Density Functional Theory

3.4.1. Calculation parameters

The first-principles calculations were performed based on the DFT with the generalized gradient approximation in the form of Perdew-Burke-Ernzerhof implemented in the Vienna Ab initio Simulation Package (VASP). The electron ion interaction was described with the projector augmented wave method. Vaspkit package was used to generate input files.[80] Vesta software was used for visualization and model constructions.[81]

Before calculations, the convergence tests were performed to determine the values of K points and cutoff energy (E_{cutoff}) for each system. The Gibbs free energy change of each step during CO_2RR and HER was determined based on the CHE model.[15] The Gibbs free energy of the slabs with different adsorbents was determined by the following equation Equation 3.1:

$$G = E_{DFT} + E_{ZPE} + \int C_p dT - TS \tag{3.1}$$

where E_{DFT}, E_{ZPE} , $\int C_p dT$ and TS stand for the DFT calculated electronic energy, zero-point energy, enthalpy correction and entropy correction, respectively.

- Calculation details for BBO

For unit cell optimization, a cutoff energy of 520 eV was set. Spin polarization was considered in all calculations. Based on the optimized cells, the following calculations were performed on a (3

× 3) Bi (003) slab, (3 × 1) BBO (100) and (3 × 1) BBO (001) slab with a 15 Å vacuum layer on the top (Table S4.2). Brillouin Zone k points (3 ×3×1), (6 ×5×1) and (4 ×5×1) were generated for Bi (003) slab, BBO (100) and BBO (001) slab, respectively, and the cutoff energy was set as 500 eV. The criterion of convergence for electronic step was set as 10^{-5}. The two upper layers of the slab were allowed to fully relax until a maximum force component of 0.02 eV $Å^{-1}$ was reached, and the positions of other atoms were fixed. To obtain the optimized model with *OCHO adsorption, the different supercell models with various adsorption locations were considered, and the configuration with the lowest energy was used in the subsequent calculations (Table S4.3).

- Calculation details for Bi-C and Bi-NC

The Bi single atom embedded at the vacancy site of C and NC was modeled by replacing the carbon atom(s) with Bi atom(s) or/and N atoms in a 4 * 4 graphene supercell based on the previous reports.[82,83] The configurations were diversified by filling single and double vacancies with Bi atom, followed by replacing the coordinated carbon atom(s) with nitrogen atom(s) in the initial BiC3 and BiC4 models. There are two different configurations when two nitrogen atoms are doped in the double vacancy models, which are labeled as BiC2N2-1 adjacent (N) and BiC2N2-2 (opposite N). A 15 Å vacuum layer was placed along Z direction in all the models to minimize the interactions between the periodic graphene sheets. A plane-wave basis cutoff energy was set as 500 eV for spin polarization calculations, and Brillouin Zone K points (4*4*1) were generated by Gamma centered grid based on the results of convergence tests. The criterion of convergence for electronic step was set as $1e^{-5}$, and all atoms were allowed to relax during the geometry optimizations until a maximum force component of 0.02 eV $Å^{-1}$ was reached. Gaussian smearing

was adopted for calculations based the previous reports.[83,84] DFT-D3 semi-empirical van der Waals corrections were considered during structural optimization to compile with the deficiencies of DFT in dealing with dispersion interactions.[85] Furthermore, a correction of -0.45 eV for gaseous CO_2 molecule was added to compensate the deviation between theoretical and experimental results of gas-phase molecules.[86] The thermodynamic stabilities of Bi SAs were evaluated by calculating the E_b of different models with $E_b = E_{total} - E_g - E_a$, where E_{total} indicates the total energy of the Bi-graphene systems, E_g refers to the energy of graphene substrate, E_a stands for the energy of one atom which is calculated by dividing the Bi bulk energy by the number of Bi atoms.[84] Within this definition, the more negative values of E_b indicate the stronger bonding strength between Bi SA and the substrate.

- Calculation details for Co-CNT

For the structural optimization and electronic property calculations of CoPc-CNT, a plane wave basis set with a cutoff energy of 520 eV and the Gamma 2 × 2 × 1 K points was used to sample the Brillouin zone. The criterion of convergence for electronic step was set as $1e^{-5}$. The atoms can relax freely during the geometry optimizations until the forces were lower than 0.02 eV $Å^{-1}$. Gaussian smearing with a smearing width of 0.05 eV was adopted based on the previous reports. The vacuum thickness was set as 20 Å along the Z-axis. For the calculations of the simplified CoN4C8N4 embedded in graphene, a $\sqrt{2} * \sqrt{2}$ graphene unit cell (rectangular cell) was employed to construct a (7 x 3 x 1) supercell to ensure applications of the biaxial strain, and to avoid the interactions between adjacent CoN4C8N4 motifs. During the application of strain, the a/b value of the supercell was fixated. The Gamma 2 × 3 × 1 K points was used, and the vacuum thickness

was set as 15 Å along the Z-axis. For all the calculations, the Van der Waals interactions were corrected using DFT-D3 semi-empirical to cope with the deficiencies of DFT in dealing with dispersion interactions. Spin polarizations were also considered in all the calculations. Furthermore, a correction of -0.45 eV for gaseous CO_2 molecule was added to compensate the deviation between the theoretical and experimental results of gas-phase molecules.

3.4.2. Reaction pathways

- ***FA pathway***

the elementary reaction step along FA pathway can be represented by Equations 3.2 and 3.3:

$$\mathrm{CO_2} + * + \mathrm{H^+} + \mathrm{e^-} \leftrightarrow {}^*\mathrm{OCHO} \tag{3.2}$$

$${}^*\mathrm{OCHO} + \mathrm{H^+} + \mathrm{e^-} \leftrightarrow * + \mathrm{HCOOH} \tag{3.3}$$

where $*$ stands for the adsorption site. The ΔG for each step can be calculated using the Equations 3.4 and 3.5:

$$\Delta G1[{}^*\mathrm{OCHO}] = G[{}^*\mathrm{OCHO}] - G[*] - G[\mathrm{CO_2}] - G[\mathrm{H^+}] - G[\mathrm{e^-}] \tag{3.4}$$

$$\Delta G2[\mathrm{HCOOH}] = G[\mathrm{HCOOH}] - G[\mathrm{CO_2}] - 2G[\mathrm{H^+}] - 2G[\mathrm{e^-}] \tag{3.5}$$

The free energy change diagrams were plotted based on ΔG1 and ΔG2.

- ***CO pathway***

$$\mathrm{CO_2} + * + \mathrm{H^+} + \mathrm{e^-} \leftrightarrow {}^*\mathrm{COOH} \tag{3.6}$$

$$^{*}COOH + H^{+} + e^{-} \leftrightarrow {}^{*}CO + H_2O \quad (3.7)$$

$$^{*}CO \leftrightarrow * + CO \quad (3.8)$$

where $*$ stands for the adsorption site. The ΔG for each step can be calculated using the Equations 3.9-3.11:

$$\Delta G3[^{*}COOH] = G[^{*}COOH] - G[*] - G[CO_2] - G[H^{+}] - G[e^{-}] \quad (3.9)$$

$$\Delta G4[^{*}CO] = G[^{*}CO] + G[H_2O] - G[CO_2] - G[*] - 2G[H^{+}] - 2G[e^{-}] \quad (3.10)$$

$$\Delta G5[CO] = G[CO] + G[H_2O] - G[CO_2] - 2G[H^{+}] - 2G[e^{-}] \quad (3.11)$$

The free energy change diagrams were plotted based on ΔG3, ΔG4 and ΔG5.

- ***H_2 pathway***

$$* + H^{+} + e^{-} \leftrightarrow {}^{*}H \quad (3.12)$$

$$H^{+} + {}^{*}H + e^{-} \leftrightarrow * + H_2 \quad (3.13)$$

The Gibbs free energy change for HER can be calculated using the Equation 3.14:

$$\Delta G6[^{*}H] = G[^{*}H] - G[*] - G[H^{+}] - G[e^{-}] \quad (3.14)$$

The free energy change diagrams were plotted based on ΔG6.

Chapter 4. Electrochemically Reconstructed Perovskite with Cooperative Catalytic Sites for CO_2-to-formate Conversion

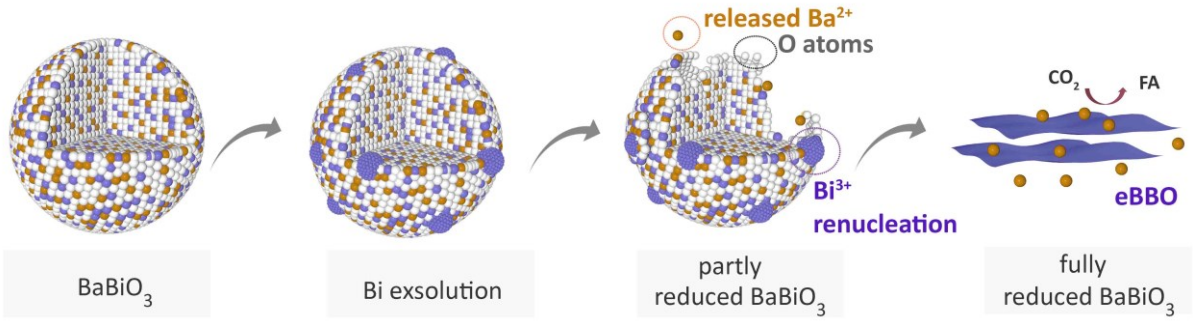

Figure 4.1 Illustration of the structural evolution of BBO under cathodic potentials (colors of the atom, orange: Ba; purple: Bi; white: oxygen).

4.1. Introduction

CO_2RR driven by sustainable energy resources holds great promise for alleviating the adverse effects of CO_2 accumulation by converting CO_2 to value-added chemicals in order to realize zero net emission of CO_2 in the carbon cycle of CO_2-fuel-CO_2 [12,87–89]. FA is an important liquid product of CO_2RR and plays an indispensable part in various industrial processes [90–93]. For the past few years, substantial efforts have been devoted to boosting the CO_2-to-FA conversion using different nanostructured catalysts, however, the complicated synthesis procedures and low product yields are usually associated with many of these catalysts, which hinder their scalability. Therefore, it is imperative to synthesize electrocatalysts through rational design with easy fabrication process and economic feasibility to advance CO_2RR technology for its large-scale implementation.

Inspired by the multiple advantages of perovskites (e.g., structural/compositional flexibility, good scalability, etc.), we pursue initiating the room-temperature electrochemical conversion of CO_2 on perovskite-based catalysts owing to their excellent activity and easy production [94–96]. It has been well recognized that B-site cations of perovskites play major catalytic roles, and this knowledge provides a basis when choosing appropriate perovskite. For instance, Cu-based perovskites have been shown to favorably produce hydrocarbon products, i.e. CH_4 [38], C_2H_4 [97], while Sn-based perovskites, in sharp contrast, tend to selectively produce FA [33]. According to these studies, a close correlation can be established between the type of B-site species and production distributions in CO_2RR. The second concern that needs to be addressed is the potential-induced reconstruction of perovskites at catalytically relevant voltages. Electricity-driven reconstructions in electrocatalysts have been actively investigated in binary metal compounds (e.g., oxides, sulfides, etc.) for various applications including OER, HER, etc. [98–100], but rarely discussed in perovskites for room-temperature CO_2RR. In general, the voltage-driven reconstructions in perovskites could lead to the change of crystal phase accompanied by the evolution of geometrical structures (e.g., enlarged surface area, more exposed active sites, etc.); and/or give rise to new electronic features that stabilize certain intermediates and lead to the promoted activity of reactions [101–104]. Finally, it should be noted that the electrochemical reduction of perovskite will trigger the rearrangement of all or a portion of A-site elements due to the “diffusion - re-nucleation - growth” of B-site ions [105,106]. Since A-site elements in perovskites are usually considered to be non-active in CO_2RR (i.e., Pr, Ba, La, and Sr, etc.), the role of A-site elements in CO_2 conversion under room-temperature conditions has been overlooked so far.

Therefore, the reconstructions of perovskites under cathodic potentials may be of great significance for CO_2RR and require further investigations.

In this work, the BBO perovskite is fabricated by crystallization of the sol-gel Ba^{2+}/Bi^{3+} nitrate crosslinkers. Bi cations placed at B-site is expected to facilitate FA production, whereas Ba at A-site is determined due to its suitable ionic radius and valence state to form perovskite structure. Our studies show that under negative potentials, BBO pre-catalysts undergo irreversible structural and phase transformations, giving rise to electricity induced BBO (eBBO) that leads to high FA selectivity in both EC and PEC cells. Further investigations reveal that A-site element (Ba) can diffuse to the electrolyte and remain as Ba^{2+} ions, and the effects of Ba^{2+} on CO_2RR are co-dependent on the type of electrolyte, the external potentials, and the concentration of Ba^{2+} in the electrolyte. Our study proposes that the utilization of both A- and B- sites in BBO to benefit CO_2 conversion could be possible, which may be extended to other perovskite electrocatalysts for CO_2RR.

4.2. Results and Discussion

Gram-scale BBO powder was synthesized by annealing 0.01 mol BBO sol-gel precursor under high temperature followed by ball-milling for 6 hours to achieve the smaller particle size distributions of BBO. The XRD pattern of the sintered powder matches well with the standard monoclinic BBO phase (JCPDS: 035-1020, Figure 4.1a) with no discernable impurity phase. The successful synthesis of BBO is further corroborated by the Raman scattering spectrum where the three fingerprint vibrations emerged at 300.0, 492.1, and 556.4 cm^{-1} can be well assigned to the superstition of Bi-O bending mode, Bi-O stretching mode, and the $[BiO_6]$ breathing with A_g

symmetry in monoclinic BBO, respectively (Figure 4.1b).[107] The FE-SEM and TEM reveal that the ball-milled BBO composes of the irregularly shaped nanoparticles (Figure 4.1c and 4.1d).

Considering the cathodic working potential nature of CO_2RR, we performed the CV analysis in Argon-saturated 0.1 M $KHCO_3$ with a scan rate of 20 mV s^{-1} to initially probe the redox capabilities of fresh BBO (Figure 4.1e). No distinguishable reduction peak could be observed in the initial cathodic sweep, but starting from the second scan, a cathodic peak merged at 0.04 V, indicative of the reduction of Bi ions. The inter-crossing point located at - 0.07 V is attributed to the insulating nature of BBO and the high energy requirement to deconstruct BBO scaffold.[108] In anodic scans, three anodic peaks located at 0.23 V (point C), 0.43 V (point D) and 0.63 V (point E) represent the oxidation reactions from Bi^0 to Bi^{3+}. The presence of Bi^0 phase is further supported by performing the XRD analysis over catholically reduced BBO electrodes at - 1.2 V for various time periods of 100, 500, 1000, 3000 and 5000 s (denoted as BBO100, BBO500, BBO1000, BBO3000, and BBO5000, respectively, Figure 4.1f). The peaks emerged at 23.8°, 27.2°, 37.9° and 39.6° are well indexed to the (003), (012), (104) and Bi (110) facets of metallic Bi, respectively, thus confirming the formation of rhombohedral Bi^0 (JCPDS: 44-1426) in all reduced BBO samples. Notably, the readily observed Bi^0 phase in BBO100 imply that voltage-driven Bi reduction is an extremely efficient process compared to the traditional high-temperature annealing method in reducing atmosphere (which usually takes up to hours).[106] Based on these results, we further performed Raman spectroscopy over a typical phase-changed BBO3000 (Figure 4.1g). Clearly, the absence of all three representative BBO Raman shifts in BBO3000 confirms the deconstruction of BBO architecture upon deep reductions.

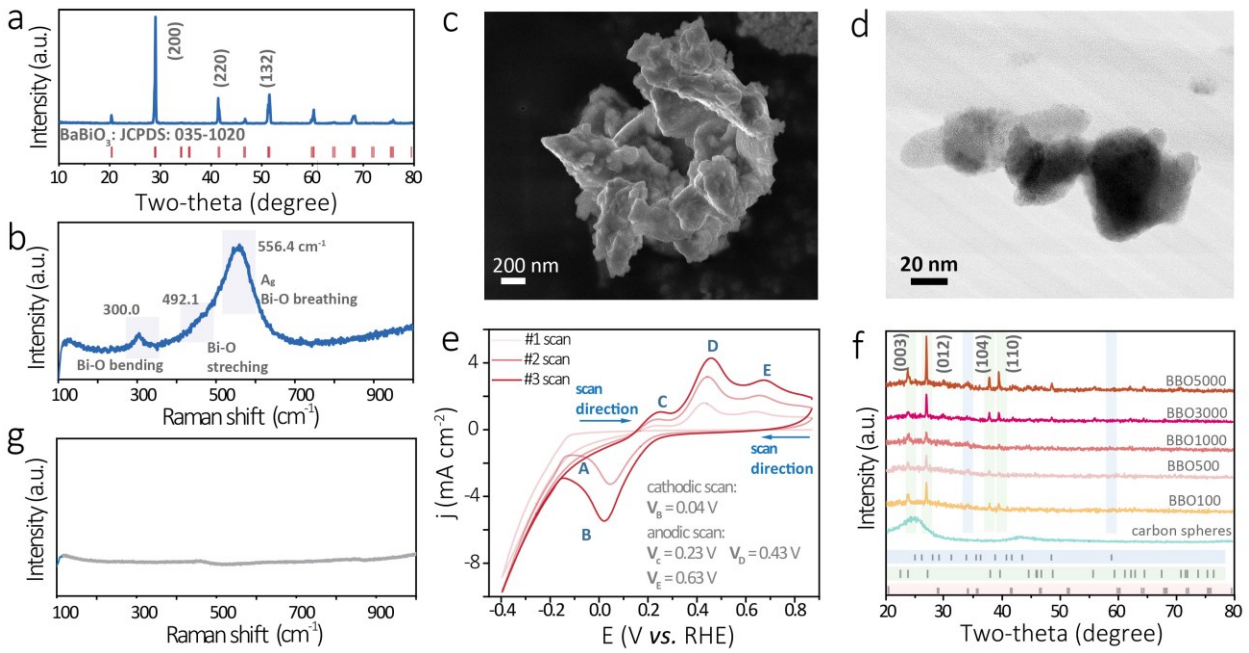

Figure 4.1 (a) XRD pattern, (b) Raman spectrum, (c) FE-SEM and (d) TEM of fresh BBO powder. (e) CV curves of fresh BBO electrode. (f) *Ex situ* XRD analysis of BBO electrodes reduced at various time periods of 100, 500, 1000, 3000, and 5000 s (green: JCPDS Bi: 44-1246; blue: JCPDS $Bi_2O_2CO_3$: 41-1448; red: JCPDS $BaBiO_3$: 035-1020). (g) Raman spectrum of BBO3000.

The surface chemistry of BBO3000 was studied by the XPS. As shown in Figure 4.2, the Bi 4f spectra of BBO3000 and the control sample Bi-3000 (where the commercial Bi nanoparticles were reduced at - 1.2 V for 3000s) exhibit the similar features, and the two peaks located at ca. 159 eV and 164 eV can be ascribed to the $Bi^{\delta+}$ ($0 < \delta < 3$) resulting from the oxidation of surface Bi species. The surface oxides of the BBO3000 and Bi-3000 were then partly removed by the Ar^+ sputter etching for three minutes (denoted as BBO3000-etch and metal Bi-3000-etch, respectively). After surface etching, the original XPS peaks split into four new peaks. The new peaks located at around 157.1 and 162.4 eV can be ascribed to metallic Bi; the other two peaks at around 159.6 and 165.0

eV can be assigned to Bi^{3+}.The resembled Bi 4f scans of BBO3000 and metal Bi suggest similar chemical states of Bi atoms in BBO3000 and metallic Bi. These results confirm that the fresh BBO was reduced to Bi^0 phase when subjected to the external potential of - 1.2 V for 3000 s. Moreover, the Ba signals are completely vanished after cathodic polarization, as observed from XPS, which is presumably explained by the release of Ba^{2+} into the surrounding electrolyte, rather than the formation of relevant Ba species (i.e., BaO) at the electrode surface.

Ex situ FESEM images of the different BBO samples during the reduction process were captured to examine the surface morphology changes (Figure 4.3). Upon a short reduction time of 100 s, no apparent morphological changes have been observed, but the surface of BBO100 is clearly roughened, which is assigned to the partial Bi exsolution from BBO lattice. Starting from BBO500, all samples show the nanosheets structures, indicating that the cathodic potentials could not only modify the electronic properties of Bi centers, but also lead to rapid self-reconstruction in nanostructures. HRTEM in conjunction with EDX mapping and the corresponding line scans were employed to characterize three representative samples (Figure 4.4), namely, BBO100, BBO1000 and BBO3000, to uncover the evolution process of BBO. In the initial stage of reduction (BBO100), nanosized Bi were clearly exsolved on the surface of BBO, leading to the intermediate Bi/BBO structures where the unreacted BBO core is covered by the Bi shell. This observation is in accordance with XRD and FESEM results. As the reduction prolongs to 1000 s, the BBO phase is hardly maintained, as revealed by the much weaker intensity of Ba signal compared to BBO100. Noteworthy, the majority of BBO should have converted to Bi at this point due to the severe BBO dissolution. As the reaction time extends to 3000 s, only the Bi nanosheets can be identified.

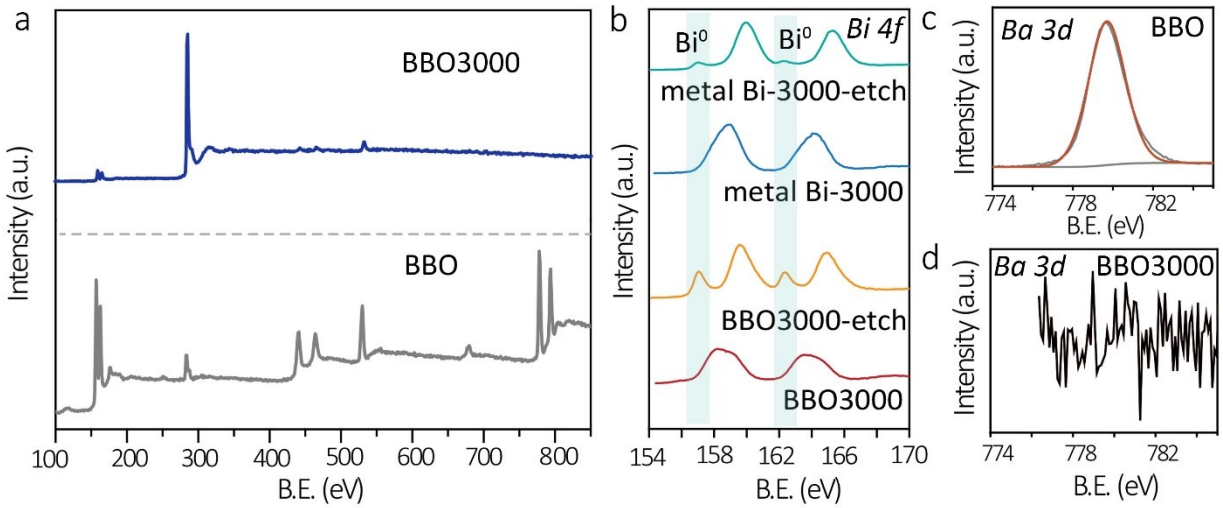

Figure 4.2 (a) XPS survey scans of BBO and BBO3000. (b) High-resolution Bi 4f spectra of metal Bi-3000 and BBO3000 before and after Ar etching for 3 mins. (c, d) High-resolution Ba 3d spectra of (c) BBO and (d) BBO3000, respectively.

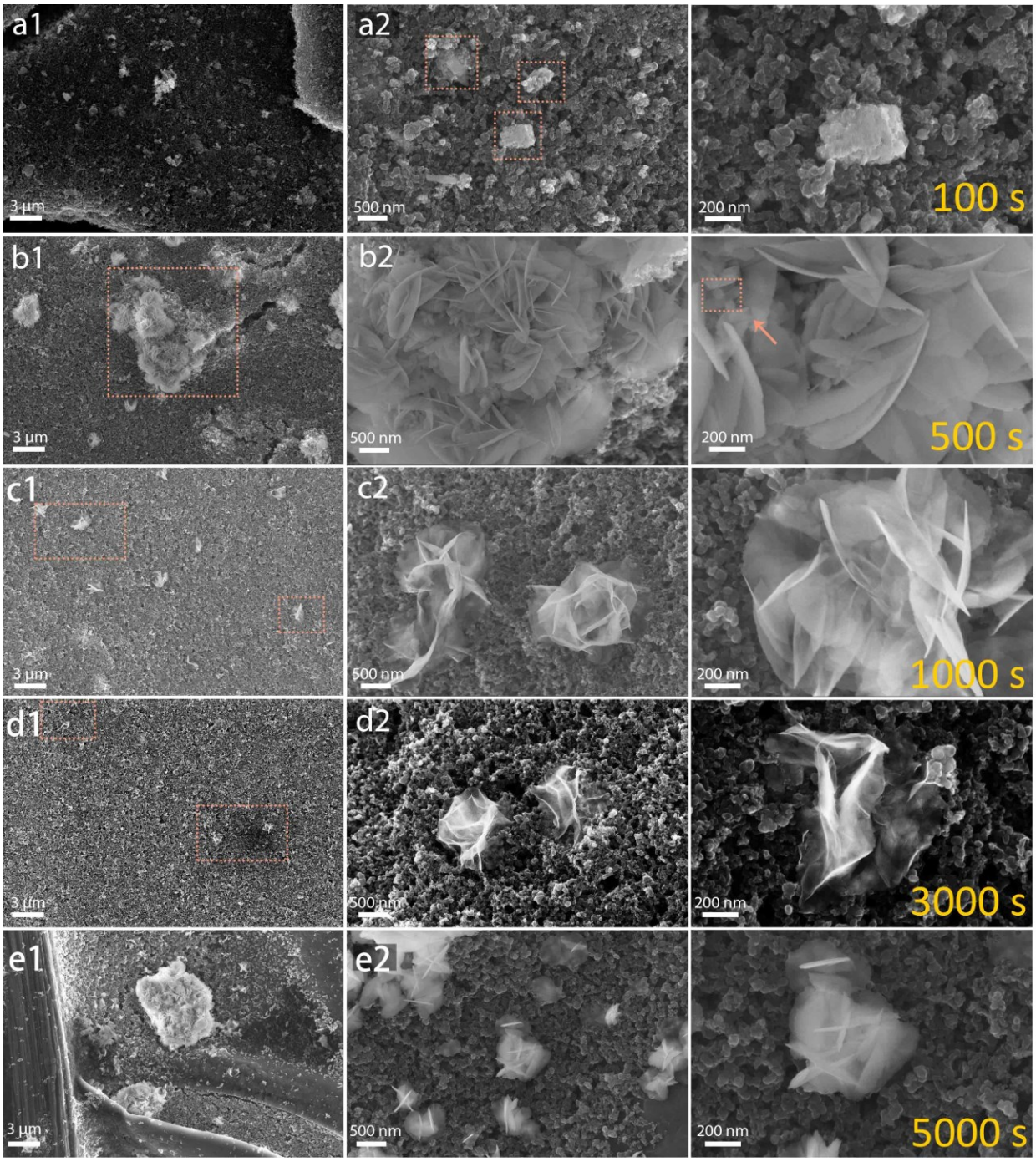

Figure 4.3 (a-e) FE-SEM images of catholically reduced BBO powder with various reduction times of (a) 100, (b) 500, (c) 1000, (d) 3000, and (e) 5000 s at three different magnifications.

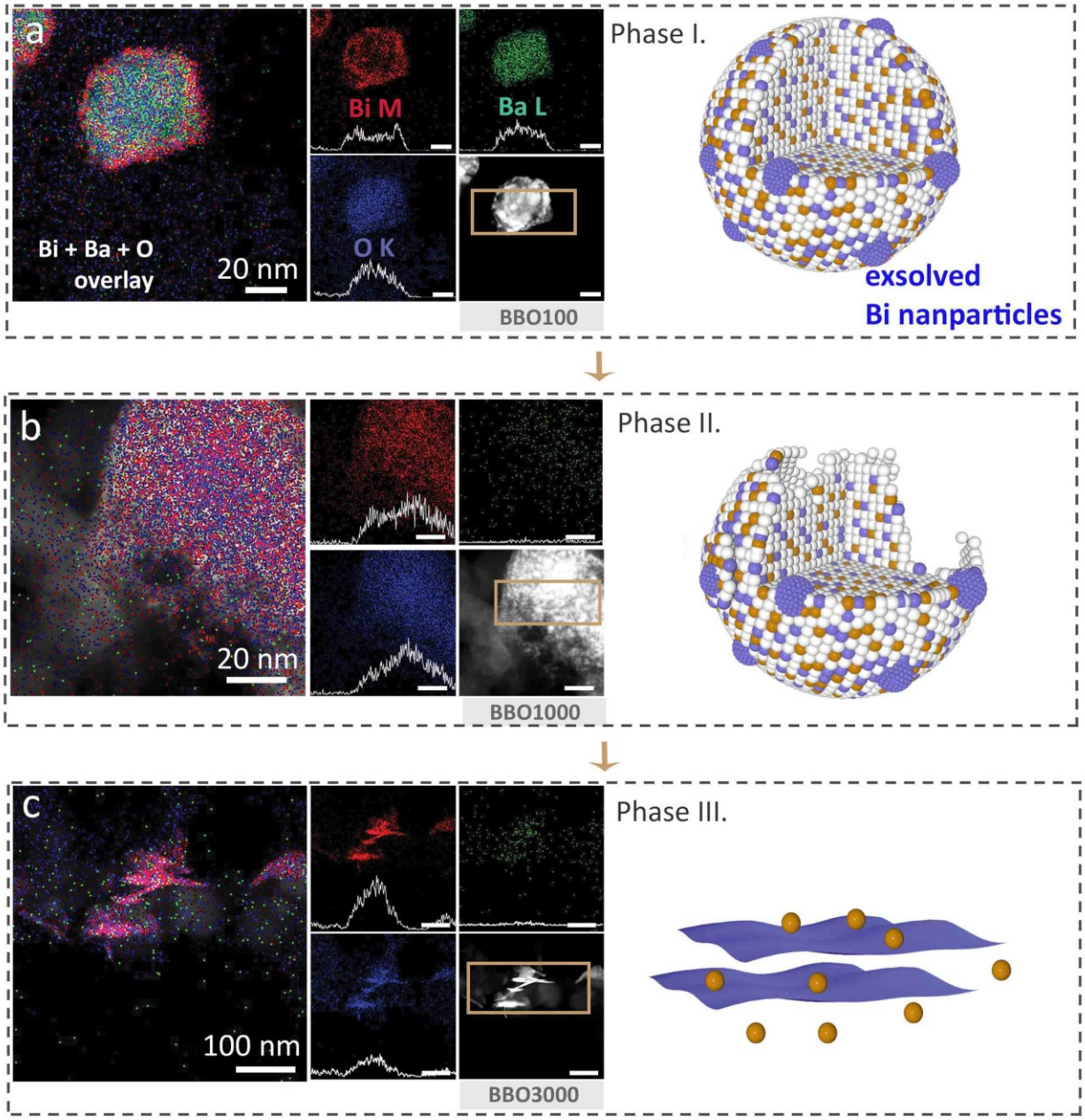

Figure 4.4 (a-c) HAADF-STEM dark field images, the EDX mappings and the corresponding schematic illustration of the structures of (a) BBO100, (b) BBO1000 and (c) BBO3000 to uncover the BBO reduction (cartoon: orange: Ba; purple: Bi; white: oxygen).

The dissolution of BBO scaffolds is further evidenced by comparing the C_{dl} values obtained over BBO samples with various reduction times (Figure 4.5). Interestingly, the C_{dl} value gradually decreases as the reduction reaction proceeds over BBO, i.e., the C_{dl} was calculated as 5.93 and 2.30 mF cm^{-2} over BBO100 and BB05000, respectively, and this can be attributed to the gradual loss of Ba sites. The ECSA value of all BBO-based samples was determined, as shown in Figure 4.5f. Despite the gradual loss of Ba sites, all BBO samples possess larger ECSA compared to that of the commercial Bi nanoparticles. Such morphology of 2D nanosheets is desirable for CO_2RR due to the maximized specific surface area, which guarantees larger contact areas between the catalysts surface and electrolyte. Moreover, the lamellar structures also endow the reduced catalyst thickness on electrode and lower the mass transfer resistance at the solid/liquid interface during CO_2RR, which in turn leads to a higher current density/reaction rate. In addition, the atomic sites at the edges of the 2D nanosheets possess multiple unsaturated chemical bonds and the dangling bonds, therefore, are more active in comparison to the atoms residing in the metal core,[104,109] thus achieving the higher catalytic activities. The edge atoms of the ultrathin nanosheets could also help reduce the activation barrier and stabilize certain reaction intermediates, making the reaction more feasible.[110]

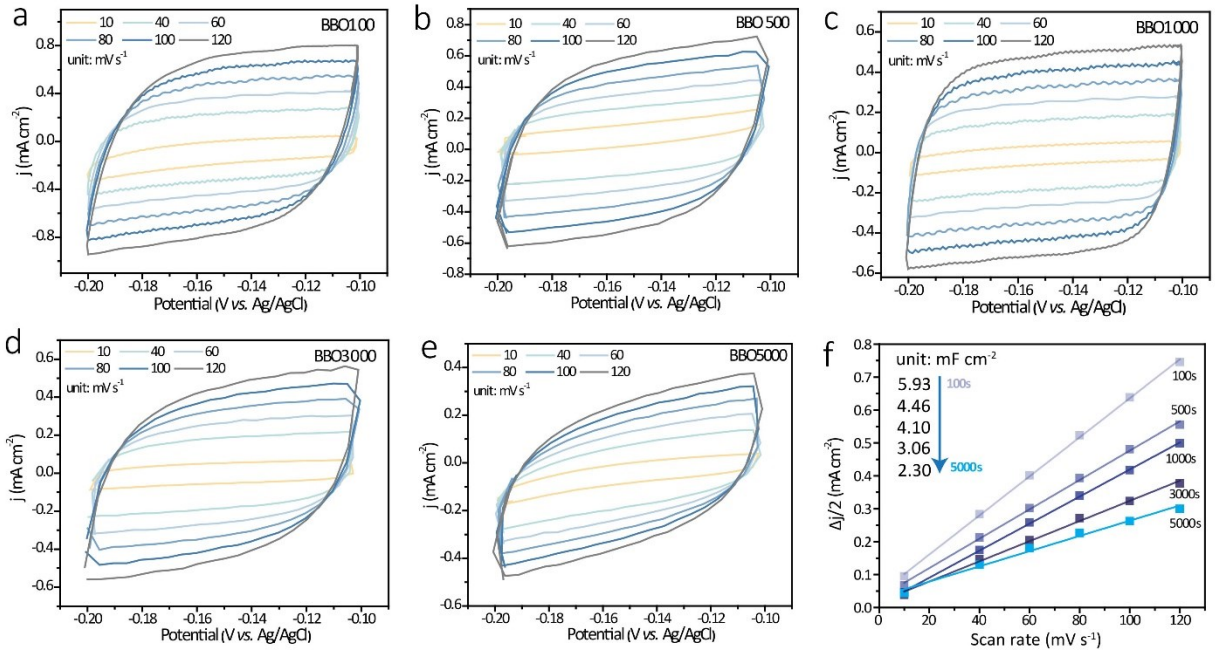

Figure 4.5 (a-e) CV analysis over BBO100, 500, 1000, 3000, and 5000 in non-Faradaic region. (f) The corresponding C_{dl} values.

The validity of the gradual Ba^{2+} loss is supported by quantifying the Ba^{2+} concentration in the used $KHCO_3$ (referred to the electrolyte used for BBO3000 preparation) by ICP-OES. The average Ba^{2+} concentration is determined to be 3.69 mg L^{-1} after reducing 1.0 mg BBO for 3000s. We repeated the electrolysis in CO_2-saturated DIW without $KHCO_3$ additive, and only identified a much lower Ba^{2+} concentration (0.097 mg L^{-1}). Therefore, both the external bias and the high conductivity of electrolyte appear to facilitate the Ba^{2+} release from BBO backbones. Furthermore, to rule out the self-dissolution of BBO in DIW, a fresh piece of BBO was placed in DIW for 3000 s without applied voltage and as expected, no detectable among of Ba^{2+} has been obtained, suggesting the structural stability of BBO under potential-free conditions in DIW. The analyses of XRD, Raman, XPS, and ICP-OES collectively confirmed the BBO-to-Bi conversion upon extended electrochemical

conditioning, accompanied by the Ba^{2+} release from the perovskite scaffolds due to the overall structural rearrangement. Based on these results, an overwhelming amount of BBO in the BBO3000 sample has been reduced to metallic Bi, denote as eBBO, and will be subjected to further electrolysis characterizations.

To briefly sum up, conventional exsolution process generally produces nanoparticles grown homogeneously on the surface of host perovskites, and the mild exsolution of B-site elements produces suitable number of vacancies while maintaining structural integrity.[106] However, from the above results and discussions, it is concluded that electrochemical conditioning can trigger Bi exsolution from BBO backbones in an instantaneous manner. Furthermore, Bi exsolution only ceases upon complete reorganization of BBO, which results in the complete phase transformation from BBO to Bi. The catalyst reconstruction route is, in essence, a Bi dissolution-renucleation-growth pathway. At the moderate potential of - 1.2 V, Bi in BBO is continuously reduced, and any remaining exsolvable Bi ions would keep diffusing from interior toward electrode/electrolyte interface until reaching an equilibrium, leading to the nucleation of Bi at electrode surface followed by the in situ preferential growth of Bi nanosheets. Meanwhile, the released Ba^{2+} ions are dissolved into the aqueous electrolyte and remain in the ionic form.

To understand whether the phase change of BBO affects the CO_2RR from a thermodynamic point of view, DFT-based calculations were performed to examine the Gibbs free energy changes of CO_2-to-FA conversion and HER on pristine BBO and the reconstructed BBO surface (Figure 4.6). BBO (100) and BBO (001) slabs were employed to represent the pristine BBO surface because Bi atoms, which are the active centers, can be well exposed on these two surfaces. Bi (003) slab was

adopted to represent BBO surface based on the previous HR-TEM results. The computational results show that the RDS for CO_2-to-FA conversion on Bi (003) is the first protonation step to produce *OCHO, which requires an energy of 1.050 eV, and the subsequent formation of FA is a barrierless step. For BBO (100), the *OCHO intermediate will adsorb to Bi atoms in all considered configurations. The RDS is also the first protonation step to form *OCHO but with a higher energy barrier of 1.21 eV compared to that of the eBBO, indicating that the activation of *CO_2 molecule to form *OCHO is more difficult on BBO (100). For BBO (001), we observed an interesting phenomenon: the *OCHO intermediate tends to coordinate with sub-surface Ba atoms rather than Bi atoms regardless of the initial adsorption site, and this is perhaps owing to the strong alkalinity of Ba atoms. However, it should be noted that Ba atoms are not the true active centers despite the easiest formation of *OCHO among all surfaces. We also simulated the free energy change of HER on these three different surfaces. For eBBO and BBO (100), the adsorption energies of *OCHO and *H show similar trend due to the existence of the scaling relation. Based on these results, we conclude that the reconstruction of BBO to produce eBBO is desirable, and the eBBO surface favors the FA production by providing suitable *OCHO adsorption energy and the barrierless desorption of FA.

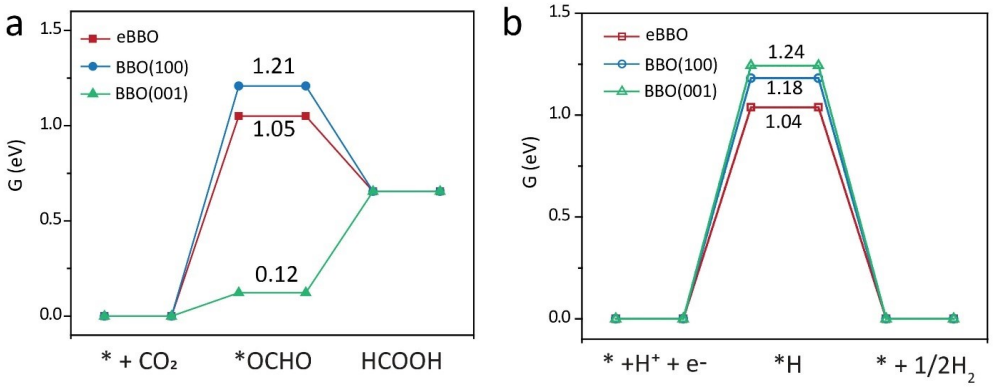

Figure 4.6 (a) Free energy diagrams of the CO_2-to-FA conversion. (b) Free energy diagrams of the HER. eBBO (red line), BBO (100) (blue line) and BBO (001) (green line).

To comprehensively evaluate the CO_2RR activity of the eBBO and to compare eBBO with the reported Bi-based catalysts, we firstly evaluated the electrocatalytic activities of eBBO in 0.1 M $KHCO_3$ electrolytes using the H-cell separated by a Nafion 117 membrane. As shown from the LSV curves in Figure 4.7a, the *j* of eBBO obtained in CO_2 bubbled electrolytes is comparatively higher than those in the argon bubbled media, indicating the occurrence of CO_2 conversion. The external potential was stepped down from -0.7 to -1.3 V to detect the product distributions of potentiostatic CO_2RR electrolysis (Figure 4.7b). The results unveil that the liquid phase is composed of FA over the entire measured voltage range, whereas H_2 and CO account for the rest gaseous phases. The FE_{FA} exceeds 90.0% as the potential shifts more negatively to -0.9 V, and the maximum FE_{FA} approaching 100% has been achieved at -1.2 V, accompanied with 0.3% of H_2 and 1.0% of CO. The FE_{FA} slightly deteriorates to 93.1% by further raising the potential to -1.3 V, and the enhanced HER at - 1.3 V may be ascribed to the limited CO_2 mass transfer. Furthermore, the high j_{FA} of - 20.7 mA cm^{-2} can be obtained at a moderate potential of -1.2 V, along with a FA

production rate of 533.2 μmol h^{-1} cm^{-2}. A control experiment using only argon as the feed gas produced almost exclusively H_2 and a trace amount of CO and FA (Figure S4.1a). The minor amounts of CO and FA came from the electrolysis of HCO_3^-, which is a common phenomenon in $KHCO_3$ based electrolyte owing to the dynamic equilibrium between dissolved CO_2 and HCO_3^-. Furthermore, no FA has been acquired over bare carbon paper substrate (Figure S4.1b), affirming the catalytic roles of eBBO rather than carbon substrate. It is well known that the evolution of H_2 from water splitting always outcompetes the CO_2RR and consequently, hampers the efficiency and selectivity of CO_2RR in aqueous media. For example, the maximum FE_{FA} has been identified as 85.7% at - 1.2 V for commercial Bi nanoparticles with larger particle sizes (Figure S4.1c and S4.1d). Clearly, the Bi ultrathin nanosheets benefit the CO_2RR by effectively suppressing the HER. Overall, the eBBO developed in this study exhibits a well-suppressed HER with FE_{H_2} maintaining at lower than 3.0% from -1.0 – -1.3, and FE_{FA} > 90% over a wide potential range of at least 400 mV in 0.1 M $KHCO_3$ solution, suggesting that the eBBO derived from perovskite is a good catalyst capable of selectively acquiring FA with high activity.

The electrochemical stability of catalysts is another important criterion to evaluate a catalyst for CO_2RR in addition to the catalytic selectivity. Thus, we examined the long-term durability of eBBO at the negative bias of -1.2 V, and the electrolyte was replaced with fresh ones periodically (around every 6.5 hours) during the test (Figure 4.4c). The eBBO achieves the stable operation over 60 h at an average current density of -21.0 mA cm^{-2} with a FE_{FA} retention of 90.0% (which corresponds to a FE_{FA} = 90.1% at the end of the 60h test). The above analysis indicates that eBBO possesses a great potential as a promising candidate for CO_2RR with the superior FA selectivity (FE_{FA} ≈ 99% at - 1.2 V) and durability (60h at - 1.2V with a FE_{FA} retention of 90%). The post-mortem

characterizations after the long-term stability tests of 12h and 60h (denoted as eBBO-12 and eBBO-60) were performed to study the eBBO at the different stages of CO_2RR.

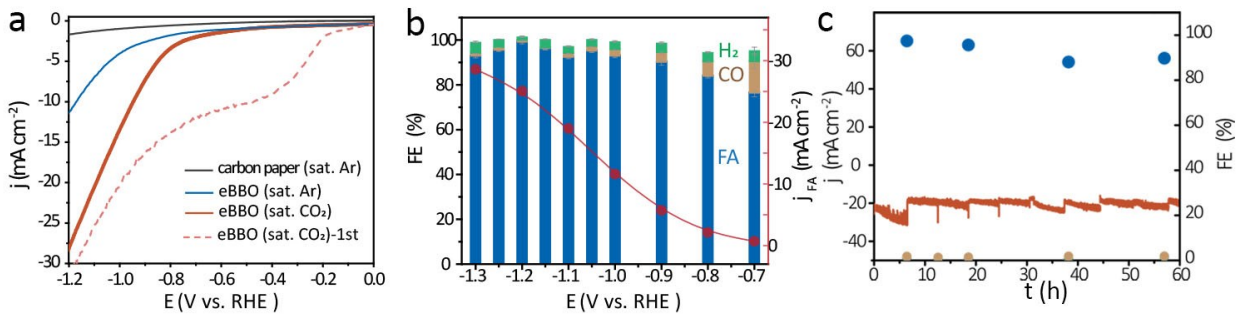

Figure 4.7 (a) LSV curves of eBBO at a scan rate of 0.05 V s^{-1}. (b) Potential-dependent FEs of H_2, CO, and FA on eBBO. (c) Long-term stability tests of eBBO at - 1.2 V in 0.1 M $KHCO_3$ electrolyte.

As shown in Figure 4.8a and 4.8b, the XRD and Raman spectra confirm the dominance of Bi^0 phase after long-time electrolysis of CO_2. The SEM image of eBBO-12 reveals the well-preserved lamellar structure of eBBO, which gradually evolved to porous Bi sheets composed of ultrasmall nanoparticles upon the extended reaction time of 60 h (Figure 4.8c-e), as further confirmed by the exposed (110) facet of Bi and EDX mappings (Figure 4.8f). Despite the emergence of the ultrasmall Bi nanoparticles, the nanosheets structures are still partly preserved. Therefore, the eBBO obtained in this study shows a good stability during the long-term tests at a very negative potential of -1.2 V. For comparison, the important merits of the recently reported Bi-based catalysts have been summarized in Table S1. More practically, the facile synthesis procedure and the low cost of $BaBiO_3$ render it suitable for industrial-scale implementations.

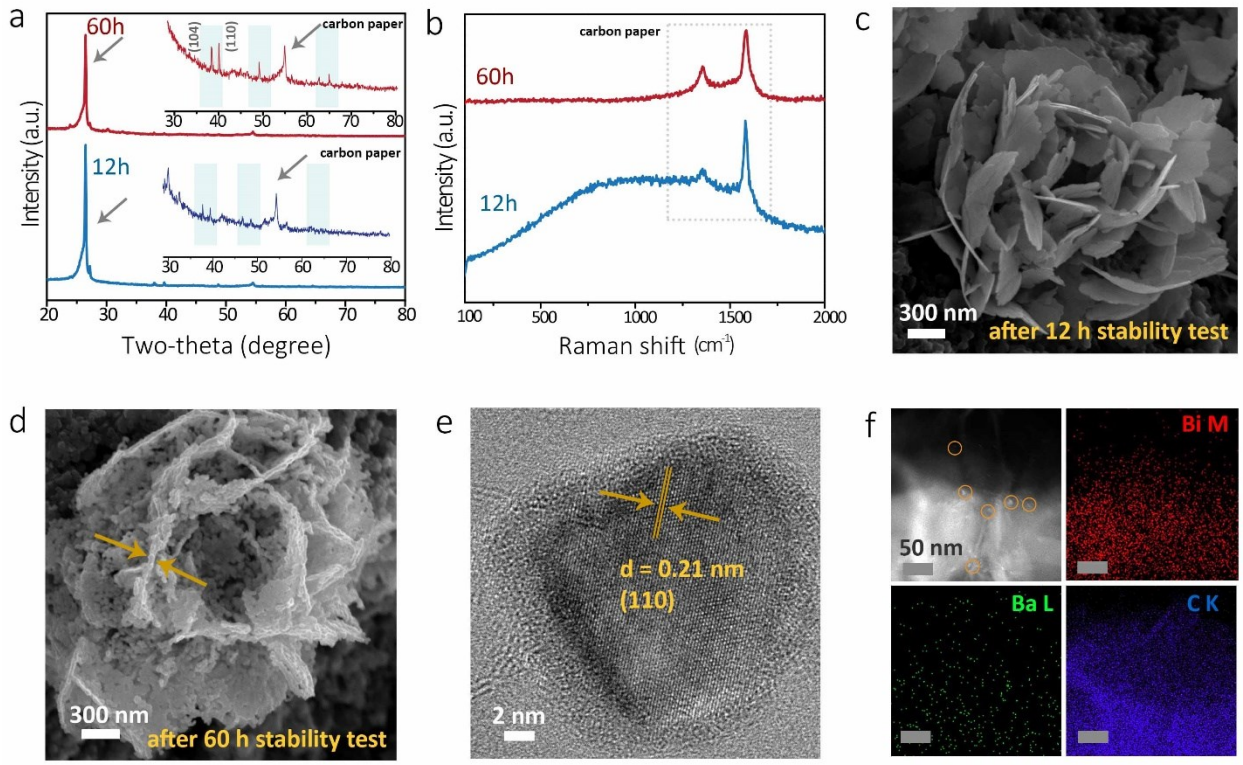

Figure 4.8 (a-f) Post-mortem characterizations eBBO-12 and eBBO-60. (a) XRD, (b) Raman, (c, d) SEM, (e) HR-TEM lattice fringes and (f) HAADF-STEM dark field image and the corresponding EDX mappings of eBBO-60h.

As stated before, zero net emission of CO_2 can be realized by utilizing renewable energy to drive CO_2RR. Inspired by the excellent CO_2-to-FA conversion on eBBO surface, we explored the opportunity to drive the reaction partially using clean and renewable solar energy by wiring the eBBO dark cathode with a low-cost $BiVO_4$ photoanode (deposited with FeOOH and NiOOH layers) for the OER reaction to construct a PEC (BVOh-FN|0.1 M $KHCO_3$|eBBO, Figure 4.9a). Thus, to unveil the optimal working conditions of BVOh-FN|0.1 M $KHCO_3$|eBBO, the illuminated/dark LSV signals of eBBO coupled with BVOh-FN were firstly collected at the cell potentials from 0 to 3.5 V (Figure 4.9b). It is observed that the dark current of BVOh-FN|0.1 M $KHCO_3$|eBBO remains

comparably small when the cell potentials stay below 2.0 V. As the potentials shift upward, the dark currents start to contribute a non-negligible portion to the I. The photocurrent, I_{photo}, determined by finding the difference between the currents measured under dark and light conditions in BVOh-FN|0.1M $KHCO_3$|eBBO is shown in Figure 4.9c (blue line). A closer examination reveals that I_{photo} reaches the maximal value at a cell voltage of around 2.75 V, which is the vertex of the parabola. To better distinguish between the contributions of solar and electricity energy inputs, the cathode potential and the corresponding I are monitored as a function of the applied potentials on photoanode, and the results are shown in Figure 4.9d. Apparently, the potential of dark cathode increases rapidly when the anodic potential increases from 0.5 to 1.1 V, but the rate gradually decreases as the anode potential exceeds 1.1 V (Point K). Furthermore, the current increase rate in the anodic potential range of 0.5 – 1.1 V is clearly much higher than that in the 1.1 – 2 V range, suggesting a more efficient utilization of solar energy in the potential range of 0.5 – 1.1 V. These results collectively point out that the maximal utilization of solar energy can be accomplished approximately at the point K where the cell voltage of around 2 V with a total current of 2.5 mA is achieved. This result is slightly at variance with the data obtained from LSV results, which is presumably ascribed to the rapid scan rate of LSV. In light of all the experimental evidence, the overall operational voltages should be in the range of 2.0 – 2.75 V in the BVOh-FN|0.1 M $KHCO_3$|eBBO for PEC device to truly benefit from solar energy.

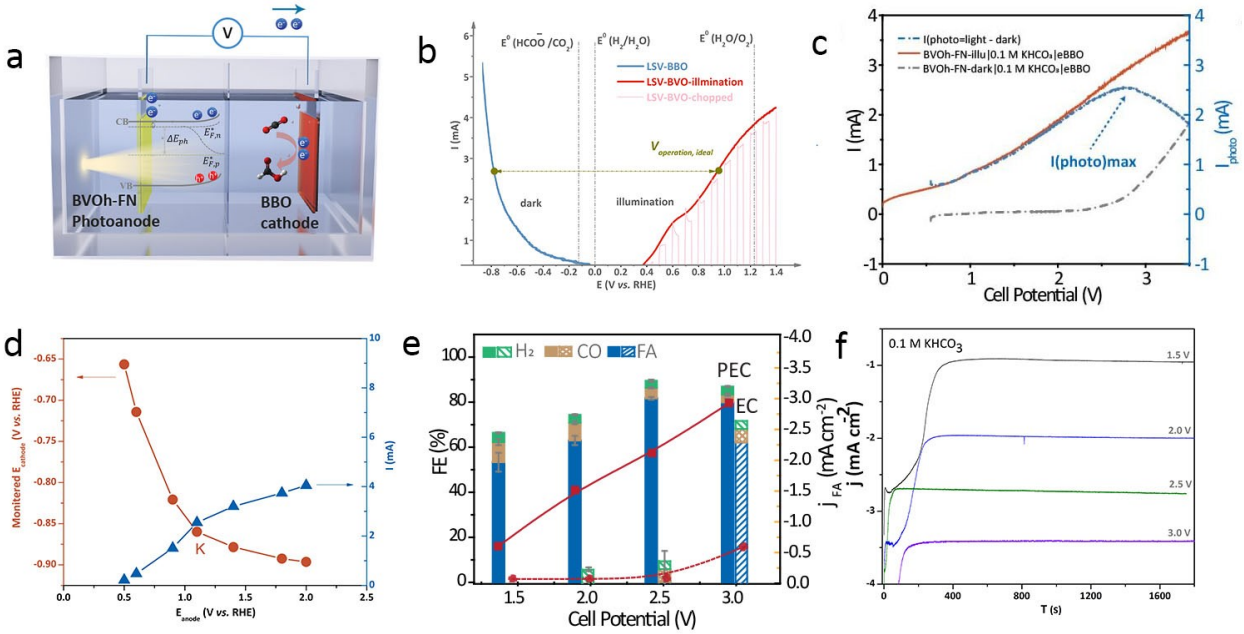

Figure 4.9 (a) Schematic illustration of the PEC device. (b) Illustration of the optimal working condition of BVOh-FN|0.1 M KHCO3|eBBO PEC cell. (c) LSV curves for BVOh-FN-illu|0.1 M $KHCO_3$|eBBO, BVOh-FN-dark|0.1 M $KHCO_3$|eBBO, and corresponded I_{photo} (photocurrent) as a function of cell potential in two-electrode cells. (d) Monitored potentials of eBBO cathode and the applied potential on photoanode as a function of the current. (e) Potential-dependent FEs and partial current densities for FA in BVOh-FN|0.1 M $KHCO_3$|eBBO PEC and EC cells. (f) Short-term electrochemical stabilities of BVOh-FN|0.1 M $KHCO_3$|eBBO PEC cell measured at different potentials.

The selectivity of products in PEC and EC under the optimized working conditions is shown in Figure 4.9e. It is found that FA can be generated with the FE_{FA} of 59.0% and 63.3% at the cell voltages of 1.5 and 2 V in PEC device, respectively, and the FE_{FA} gradually raises to 80.0% at a cell voltage of 2.5 V with j_{FA} of -2.1 mA cm^{-2}. Further increasing cell potential to 3 V yields a higher

FE_{FA} of 81.0%, and the j_{FA} reaches -2.9 mA cm^{-2}. Contrarily, no FA is detected in EC at 1.5 nor at 2 V, and FE_{FA} < 1.0 % is detected at 2.5 V with a negligible j_{FA} of - 0.015 mA cm^{-2}. It is only when the external bias reaches 3.0 V that the EC cell will start to contribute significantly to FA production (i.e., FE_{FA} = 60.1%). For reference, the total current densities are depicted in Figure 4.9f. Based on the above results, it can be concluded that solar energy can compensate for a portion of the external bias needed to drive the CO_2RR and can favorably shift the onset potential for FA generation to a smaller value, thereby achieving an appreciable current and FEs for target products compared to the pure electricity-driven approach. Consequently, the PEC cell realizes a high FA selectivity of 80% at the cell voltage of 2.5 V where trivial amount of FA is detected at the same potential in EC cell without solar irradiation.

The electrochemical performance of the eBBO electrode was examined in fresh electrolytes to preclude any possible perturbations of any surface or and naturally released Ba^{2+} in the electrolyte. For practical applications, the effects of Ba^{2+} should not be ignored since previous studies showed that the alkaline metal ions play a significant role in dictating the FE.[111–113] While many studies have focused on the monovalent cations (e.g., Li^+, Na^+, K^+, etc.), recent studies by Koper et al. showed that the multivalent with larger hydration radii might have even stronger impact over the performances of CO_2RR since they are more likely to stabilize CO_2, which is the key to initiate CO_2RR.[114] The hydrated radii of K^+ and Ba^{2+} are 3.31 and 4.04 Å at 25 °C,[115] respectively, and theoretically, the Ba^{2+}-CO_2 interactions should be more pronounced compared to that of the K^+-CO_2. However, in another study by Wallace et al., the CO_2RR can be greatly suppressed in the seawater-like electrolyte containing 20 mM $CaCl_2$ due to the formation of

calcium carbonate at the electrode surface at applied cathodic potentials.[116] Therefore, the concentration of certain multivalent cations must be well controlled to benefit CO_2RR.

To gain insights into how the released Ba^{2+} from BBO affects CO_2RR, a series of potential-controlled electrolysis from - 0.7 – - 1.3 V were conducted to examine the product distributions in 0.1 M $KHCO_3$ containing 0.025 mM $BaCl_2$ to mimic the naturally released Ba^{2+} when reducing 1.0 mg BBO. As shown in Figure 4.10a, the FE of FA, H_2 and CO obtained in the two electrolytes are almost overlapped, suggesting that the low Ba^{2+} concentration (i.e., 0.025 mM) has negligible effects on the CO_2 reduction in 0.1 M $KHCO_3$ media. However, in 0.1 M KCl-based electrolytes with/without 0.025 mM Ba^{2+} additive, a stark difference in FEs can be observed (Figure 4.10b). In general, the $\mathrm{FE}_{\mathrm{H}_2}$ values in Ba^{2+}-containing 0.1 M KCl solutions are always lower than that of the Ba^{2+}-free ones in the potential range of -0.9 to - 1.2 V, and meanwhile, the FE_{FA} is clearly boosted by Ba^{2+} in the electrolyte, especially at less negative potentials (i.e., -0.8 – -1.1 V). This observation is in accordance with previous studies.[117] The changes in the selectivity for FA at these potentials are closely related to the attenuated HER as the FE_{CO} remains relatively constant over the studied potential range (fluctuating within a relatively small range of ± 1.5 %), which is presumably owing to the capability of Ba^{2+} ions to repel H^+ near the electrode surface. Increasing the Ba^{2+} concentration to 2.5 mM (which is 100 times higher than the actual concentration detected in this study) has led to an even more prominent growth in FA production (Figure 4.10c), suggesting the Ba^{2+} additive has indeed contributed to the CO_2RR reaction in 0.1 M KCl. Notably, further increasing Ba^{2+} concentration to 25.0 mM results in the formation of $BaCO_3$ precipitates when the electrolysis was performed at - 1.3 V for 3000 s (Figure S4.2), which can be detrimental to CO_2RR since $BaCO_3$ could block the Bi active sites, retard efficient mass and electron transfers and thus,

impede efficient CO_2RR electrolysis. It should be noted that in real cases, however, such a high Ba^{2+} concentration in the electrolyte is unlikely to occur.

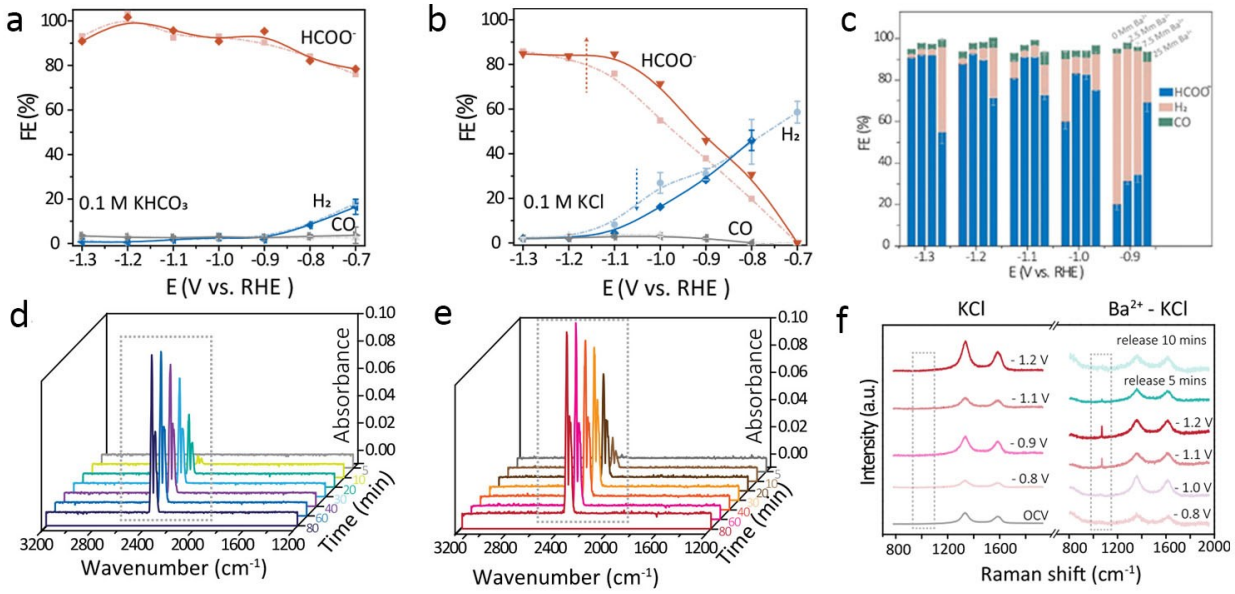

Figure 4.10 (a, b) Potential dependent FEs over eBBO in (a) 0.1 M $KHCO_3$ and (b) 0.1 M KCl electrolyte with (solid lines) or without 0.025 mM $BaCl_2$ (dash lines) addition. (c, d) Time-resolved FTIR studies of (c) eBBO and (d) Ba^{2+} - eBBO. (c) FEs of eBBO electrodes in 0 mM, 2.5 mM, 7.5 mM and 2.5 mM BaCl2 in KCl-based electrolytes. (d, e) Time-resolved FTIR studies of (c) eBBO and (d) Ba^{2+} - eBBO. (f) In situ Raman analysis of eBBO in 0.1 M KCl and Ba^{2+}-0.1 M KCl performed under various external potentials.

The understand how Ba^{2+} interplays with the CO_2 molecules, the time-resolved FTIR studies were carried out. Certain amount of $BaCl_2$ was dipped on the clean eBBO electrode and then dried overnight prior to usage (named Ba^{2+}-eBBO, assuming all the released Ba^{2+} has been adsorbed to the surface). As shown in Figure 4.10d and 4.10e, both eBBO and Ba^{2+}-eBBO samples show prominent peaks at 2200 – 2400 cm^{-1}, which can be attributed to the physical adsorption of CO_2.

The CO_2 adsorption responses of both samples could stabilize at around 60 mins, however, the signal intensities in Ba^{2+}-eBBO sample are apparently higher than that of the bare eBBO surface. For example, the peak heights in Ba^{2+}-eBBO were already larger than the bare eBBO when the reaction only proceeded for 10 mins. Therefore, the intensified FTIR signals in Ba^{2+}-eBBO indicate that Ba^{2+} favors the CO_2 adsorption, in line with previous studies.[118] To identify possible reaction intermediates of CO_2RR in 0.1 M KCl and 0.025 mM Ba^{2+} added 0.1 M KCl (Ba^{2+}-KCl), in situ Raman analysis was then performed over eBBO to gain mechanistic insights. As shown in Figure 4.10f, both the samples exhibit two characteristic Raman shifts at 1313 and 1616 cm^{-1} which are assigned to the glassy carbon substrate. In Ba^{2+}-KCl media, a marked Raman peak at around 1061 cm^{-1} can be clearly observed in a wide potential range, i.e., at - 0.8 V and more negative potentials. This peak is ascribed to the symmetric stretching oscillation of carbonate ($\nu_1 CO_3^{2-}$); whereas no $\nu_1 CO_3^{2-}$ bands can be identified on the eBBO surface measured in pure KCl electrolyte.[14,119] The formation of $BaCO_3$ can be ruled out, since the $\nu_1 CO_3^{2-}$ band gradually decreases and eventually vanishes upon releasing the applied potential (- 1.2 V). This observation indicates that the Ba^{2+} in the 0.1 M KCl electrolyte has led to enhanced adsorption of carbonate intermediate, which evidently promotes the CO_2-to-FA conversion. Song et al. reported similar results over S-doped Cu for highly selective production of FA, and their study shows that S-doped Cu exhibit much enhanced $\nu_1 CO_3^{2-}$ adsorption.[120]

In fact, previous studies have also carefully examined cation effects by analyzing their perturbations on internal electric field.[121–123] Although most of the reported studies are based on the monovalent cations/anions (e.g., Li^+, K^+, Cs^+, Na^+, Cl^-, I^-, Br^-), one can still expect the roles of multivalent ions in the electrical field to be even more significant. The "electrolyte-defined

selectivity" for CO_2RR is perhaps related to the different local CO_2 environment and CO_2-cation interactions near the catalyst surface in the two electrolytes. It is well acknowledged that $KHCO_3$ solutions can create a high local CO_2 concentration due to the equilibrium between bicarbonate and dissolved CO_2, meaning that the CO_2 consumed at surface can be rapidly replenished by bicarbonate.[124] As a result, the Ba^{2+} mediated CO_2 adsorption could only contribute a negligible amount to the total CO_2 concentration on electrode surface, and therefore the FEs of all products remain very similar in the electrolytes with/without Ba^{2+} addition. However, in 0.1 M KCl, the CO_2 is replenished by the dissolved CO_2, which is insufficient in amount compared to that in the $KHCO_3$-based solutions considering the low CO_2 solubility in the water-based electrolyte. In such a case, even the trace amount of Ba^{2+} (i.e., 0.025 – 2.5 mM) in 0.1 M KCl may lead to an effective enhancement in the local CO_2 concentration and therefore remarkably boost CO_2RR over HER, since Ba^{2+} has been shown to favor CO_2 adsorption based on the previous analysis. In a recent study by Bell et al., they also suggested that the local CO_2 concentration can be regulated by the hydrolysis of alkaline metal ions, and the CO_2 concentration improves with increasing the cation size.[125] To confirm our hypothesis, further studies that incorporate multiple in situ techniques are required to fully unveil the effects of Ba^{2+}. Nonetheless, based on our extensive electrochemical characterizations, it can therefore be concluded that the Ba^{2+} released from BBO should be beneficial to FA production in general despite that these effects are collectively dependent on the external potentials, type of electrolytes, as well as the Ba^{2+} concentration. It should be emphasized that final concentration of Ba^{2+} in the electrolytes is determined by the loading mass of catalyst, as well as the total volume of electrolyte, and these parameters may vary depending on the real operation conditions of CO_2RR.

Finally, we consider the eBBO with naturally released Ba^{2+} as one system, and the working mechanisms for CO_2-to-FA are proposed, as shown in Figure 4.11. Firstly, the adsorption of Ba^{2+} will take place at the eBBO surface at cathodic potentials. Secondly, the CO_2 dissolved in the electrolyte can be adsorbed more easier on Ba^{2+} sites and/or Bi sites adjacent to Ba^{2+}, leading to higher local CO_2 concentration compared to that of the bare Bi surface. Afterwards, the adsorbed CO_2 would gain one electron and form $CO_2^{\cdot-}$ intermediate, following the hydrogenation step to form $HCOO^{\cdot}$ (ads) which further proceeds the elementary step of $HCOO^{\cdot}$ (ads) + $e^- \rightarrow$ $HCOO^-$(ads), as proposed in the CO_2-to-FA mechanisms on Bi surface by a previous study.[126] In the final step, the $HCOO^-$(ads) desorbs from the surface and form the final product $HCOO^-$(aq). Over the entire process, both the Bi catalytic active sites and Ba^{2+} ions participate in the CO_2RR and work cooperatively to drive CO_2-to-FA conversion, and this mechanism could be extended to other perovskite-based materials for electrocatalytic CO_2RR at room temperature.

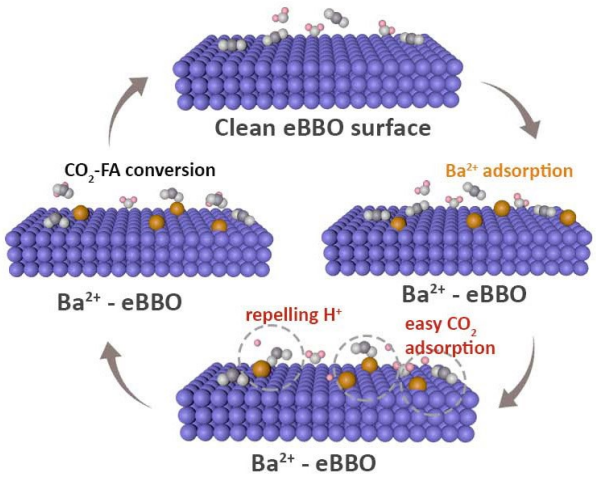

Figure 4.11 Proposed working mechanism of the eBBO with natural released Ba^{2+} in the electrolyte for the selective FA production from CO_2RR (cartoon: orange: Ba; purple: Bi; white: oxygen; grey: carbon; pink: hydrogen).

4.3. Conclusions

In summary, by a series of extensive physical and electrochemical characterizations, we are able to unveil: 1) the structural and phase evolution of pristine BBO perovskite under cathodic potentials, and that is, the electrochemical conditioning of pristine BBO leads to the in operando "dissolution-nucleation-growth" of Bi ions. The resulting eBBO with atomic-scale thickness provides an enlarged active area and more unsaturated active centers, which is among one of the best Bi-based catalysts for FA production reported so far. 2) The cooperative working mechanisms of A- and B- site species in voltage-reconstructed BBO perovskite that regulate the surface reactions. In contrast to the commonly accepted concept that only B-site elements are actively involved in CO_2RR, our experimental results and systematic analyses demonstrate that the multivalent A-site elements can concurrently participate in CO_2RR and benefit FA production

and furthermore, the Ba^{2+} concentration, external potentials and the type of electrolyte play the critical roles in enhancing the beneficial effect of Ba^{2+} on CO_2RR. Our studies show that perovskite-based materials that integrate both A- and B- site elements in one structure, should serve as an effective platform for efficient CO_2RR with mutual benefits coming from both elements.

4.4. Supporting information

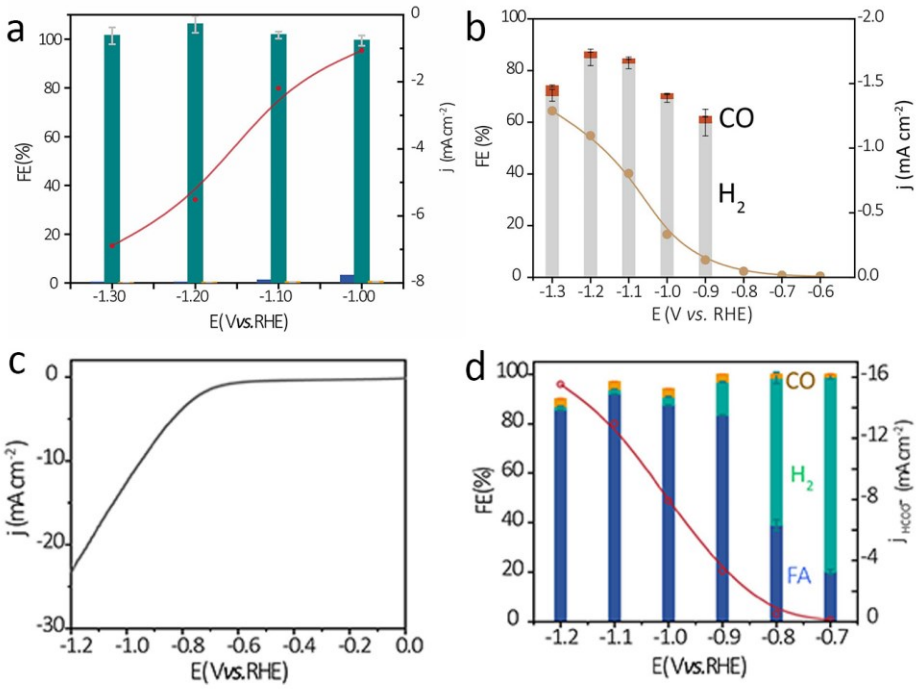

Figure S4.1 (a) Potential dependent FEs of products: H_2 (green), CO (yellow), and FA (blue) and current densities obtained over eBBO in argon saturated 0.1 M $KHCO_3$. (b) Potential dependent FEs of products: H_2 (grey) and CO (red) and total current densities obtained over bare carbon paper in CO_2 saturated 0.1 M $KHCO_3$. (c) LSV curve and (d) potential dependent FEs of H_2 (green), CO (yellow), and FA (blue) and current densities (red line) (b) of commercial Bi nanoparticles in 0.1 M $KHCO_3$ electrolyte.

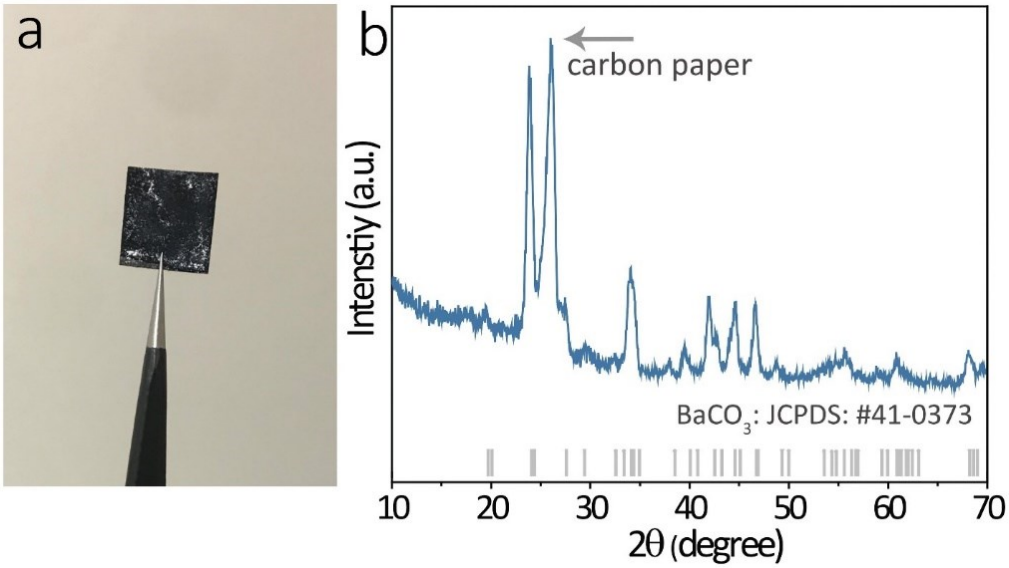

Figure S4.2 (a) Digital images of eBBO reduced in 25 mM $BaCl_2$ electrolyte at -1.3 V for 3000 s. (b) XRD patten of eBBO electrode reduced in 25 mM $BaCl_2$ for 3000 s.

Table S 4.1 Summary and comparison of Bi-based catalysts reported in literatures.

Electrocatalysts	Electrolyte	E with FEmax	FEmax		Potential window (FE > 90%)	Stability (h)
Bi_2O_3NSs@MCCM carbon matrix [126]	0.1 M $KHCO_3$	1.256 V	93.8%		300 mV	12h @-0.956V
Bi_2S_3derived Bi (SD-Bi) [127]	0.5 M $NaHCO_3$	-0.75V	84%		N.A.	24h@-0.75V
Bi_2S_3–Bi_2O_3 @rGO [128]	0.1 M KHCO3	-0.9 V	90.1%		< 100 mV	24h@-0.9 V
curved Bi nanotubes [129]	0.5 M $KHCO_3$	−1.0 V	97%		400 mV	10 h @- 1.0 V
Bi-rGO [130]	0.1 M $KHCO_3$	−0.8 V	98%		100 mV	15 h @ -0.8 V
Few-layer $Bi_2O_2CO_3$ [131]	0.5 M $NaHCO_3$	-0.7 V	85%		N.A.	12 h @-0.7 V
BiOCl nanoplates [132]	0.5 M $KHCO_3$	-0.9 V	92%		300 mv	12 h @ -0.9 v
2D Bi metal–organic framework [133]	0.1 M $KHCO_3$	-0.9 V	92.9%		100 mV	30h@-0.9 V
Metal–organic framework derived Bi [108]	0.5 M $KHCO_3$	-0.97 V	95(±3)%		200 mV	32h@-0.97 V
Bi Metal–organic framework Bi-BTC-D [134]	0.5 M $KHCO_3$	-0.86 V	95.5%		300 mV	12h@-0.86 V
$Ag_{0.95}BiS_{0.75}O_{3.1}$ nanorods [135]	0.1 M $KHCO_3$	-0.7 V	94.3%		300 mV	12h@-0.7V
This work	**0.1 M $KHCO_3$**	**V**	**FE_{HCOO^-}**	**FEtotal**	**400 mV**	**60 h@ -1.2 V (final FE_{HCOO^-} was 90.1%)**
		-1.3 V	**93.1%**	**98.8%**		
		-1.2 V	**~100.0 %**	**103.9%**		
		-1.1 V	**92.5%**	**96.9%**		
		-1.0 V	**93.0%**	**99.0%**		
		-0.9 V	**90.3%**	**98.4%**		
		-0.8 V	**84.0%**	**94.2%**		
		-0.7 V	**81.6%**	**100.1%**		

Table S 4.2 BBO (001) and BBO (100) slabs viewed from the a-axis, b-axis, and c-axis (red: oxygen, purple: bismuth, green: barium).

BBO (001)					
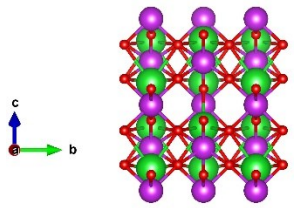	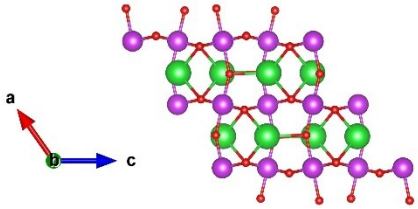	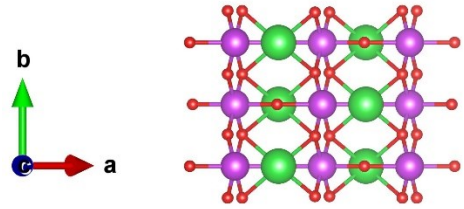			
BBO (100)					
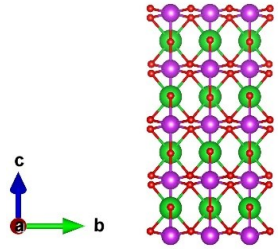	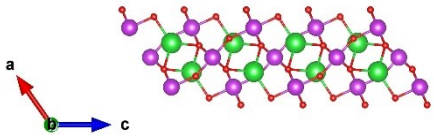	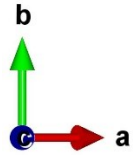	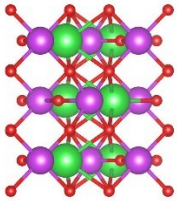		

Table S 4.3 Summary of the configurations and energies of *OCHO and *H intermediate adsorbed on BBO (001), BBO (100), and Bi (003) surface.

BBO (001)	
BBO (001) -*OCHO	
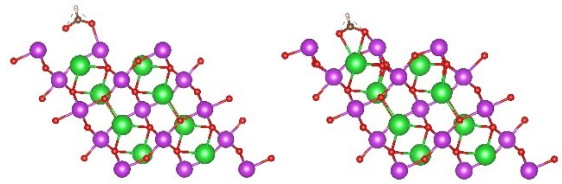	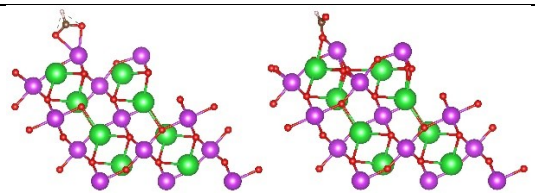
1. E_{DFT} = - 269.14 eV	2. E_{DFT} = -268.95 eV
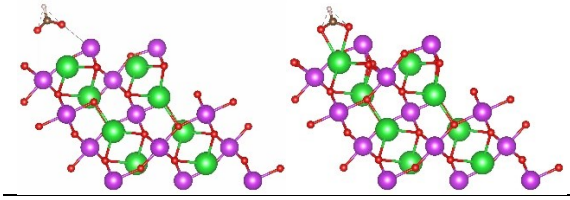	
3. EDFT = - 269.14 eV	
BBO (001) -*H	
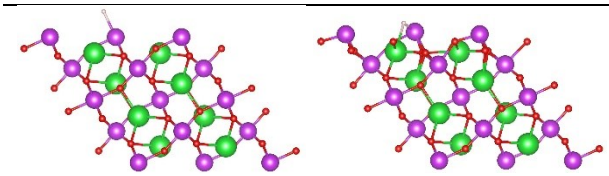	
4. EDFT = - 244.51 eV	
BBO (100)	
BBO (100) -*OCHO	
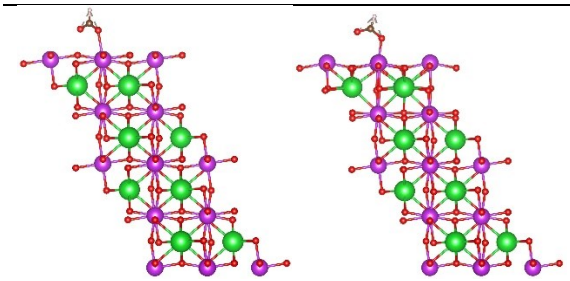	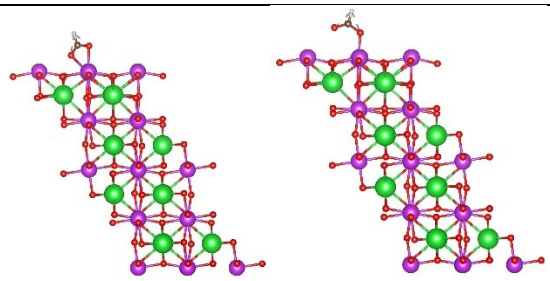
5. E_{DFT} = - 281.63 eV	6. E_{DFT} = - 281.64 eV

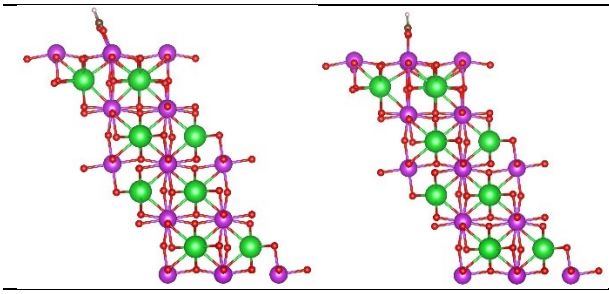

7. E_{DFT} = - 281.76 eV

BBO (100) -*H

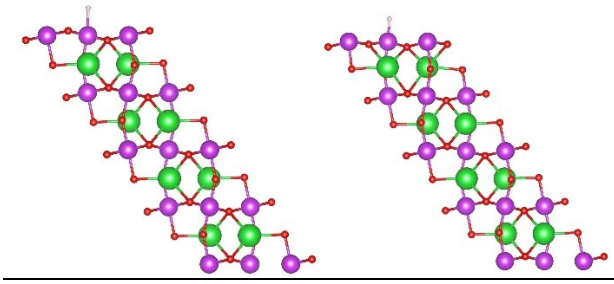

8. E_{DFT} = - 258.27 eV

Bi (003)

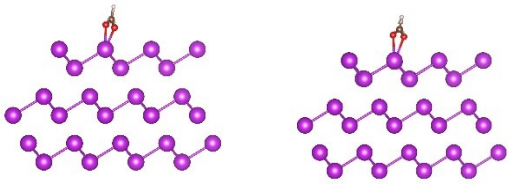

9. E_{DFT} = - 232.60 eV

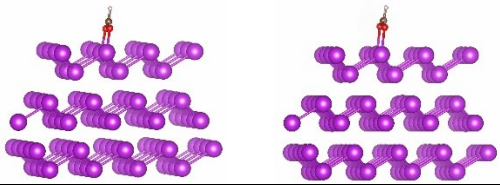

10. E_{DFT} = - 232.50 eV

Chapter 5. Nanosecond Laser Confined Bismuth Moiety with Tunable Structures on Graphene for Carbon Dioxide Reduction

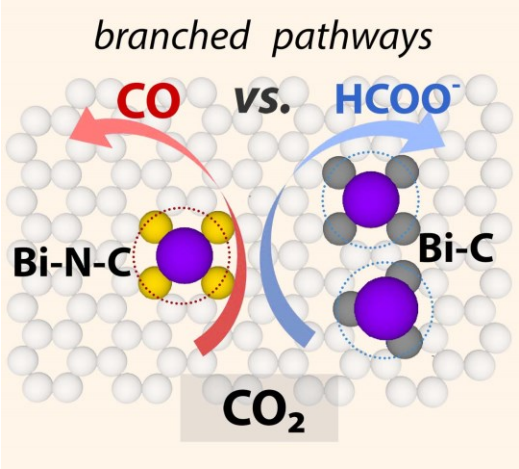

Figure 5.1 Illustration of the structure-performance relation over two Bi SACs (color of the atoms, purple: Bi; yellow: nitrogen; light grey: carbon on the substrates; dark grey: carbon coordinated to Bi).

5.1. Introduction

CO_2RR driven by renewable energy resources is a promising strategy to accelerate the advent of the ultimate carbon neutrality.[136] Catalysts supported by suitable substrates possess the well exposed active centers and unique metal-support interactions, rendering them a promising group of catalysts to drive CO_2RR.[3,137] Among all the candidates, Bi metal-based materials demonstrate overall excellent capabilities of converting CO_2 to versatile products, including FA and CO, with appreciable current density and selectivity.[92,138,139] To further improve atom turnover efficacy, mass-specific activity and reduce the production cost, the sizes of the

supported catalyst can be downsized from nano- to atomic-scale to expose more active sites for enhanced interplay between active sites and reactant. However, at the atomic dimension, the performance of the catalysts becomes extremely sensitive to the local environment where any subtle variations could lead to a paradigm-shift in the CO_2RR performances due to the modification of the electronic structure of the active speices.[140] This sheds light on the opportunities to fine-regulate the catalytic outcomes by rationally designing the metal-support interactions.

Previous studies have shown that coordination engineering is an effective strategy to regulate the metal-support interactions, thereby steering the catalytic outcomes. For instance, the nitrogen coordinated Sn SACs can produce FA in general while the Sn SA embedded in C_2O_2F can facilitate CO production.[55,141] Compared to Sn, Bi is even more attractive due to their better long-term stability and higher selectivity over FA in bulk forms.[142] Recent studies by Li et al.[82] and Wu et al.[143] reported that Bi atoms coordinated by nitrogen and/or sulfur atoms are promising toward CO production, in sharp contrast to another recent study claiming that only FA has been detected from CO_2RR over the Bi loaded carbon spheres.[144] The precise identification of the coordination effects requires the delicate control during materials synthesis to exclude other effects, which remains challenging. For instance, the conventional high-temperature annealing for coordination tuning would simultaneously affect the degree of the graphitization of carbon support. This, in turn, leads to the modification of both matrix and coordination structures, which complicates the understanding of these coordination effects. Furthermore, many of the reported synthesis routes reply on the initial synthesis of relevant metal organic frameworks, followed by the annealing, which oftentimes involve the usage of expensive linkers and/or solvents. Thus,

despite the achievements, the mechanisms of CO_2RR on Bi SACs currently remain elusive, and it is critical to completely understand the coordination effects on the activity of materials at the atomic level in order to advance CO_2RR technology.

In this study, the coordination-tuned CO_2RR has been comprehensively investigated using supported Bi as model catalysts. This is achieved by tailoring the type of the "glue atoms" (C and N) to Bi center *via* ultrafast laser agitation in nanoseconds. In our method, the graphene nanosheets absorb the photon energy and generate rich vacancy defects which serve as anchoring sites for Bi SAs immobilization; the bismuth salts simultaneously decompose under the high local temperature and in the reductive atmosphere induced by laser irradiation.[145] By applying graphene nanosheets with or without N dopants, the coordination structures of Bi SAs on graphene can be engineered, generating either carbon- (Bi-C) or nitrogen- (Bi-NC) bound Bi SACs, and the former catalysts selectively deliver FA as the major CO_2RR product with a TOF of 2.64 s^{-1} at 1.05 V with a high partial current density of ca. -29.3 mA cm^{-2}, exceeding most SACs reported in the literature. Theoretical simulations explicitly uncover that the coordination atoms modulate the electronic features of the Bi centers, thus determining the interactions between Bi and the intermediate species during the reaction. Consequently, Bi-C samples require the lowest energy to drive the CO_2-to-*OCHO (RDS), thus favouring the FA production, whereas the CO_2-to-*COOH (RDS) conversion to produce CO can be more easily achieved over Bi-NC with the lowest energy penalty associated with this step.

5.2. Results and Discussion

In general, the un-anchored Bi adatom supported by defect-free graphene nanosheets requires a low migration barrier energy of around 0.0 eV to move freely (0.5 eV is roughly the threshold energy of atom migration at ambient temperature).[146] In the presence of defects, vacancies or dopant atoms, in graphene, the trapping of Bi SA at such sites would occur more readily, thus inhibiting clustering and ultimately resulting in the enhanced stability owing to the robust covalency between Bi and the neighbouring atoms. We start by predicting the thermodynamic stability of Bi SA doped in ten different defective graphene models (in either single vacancy or double vacancies sites), using the E_b as the metric, and the results are shown in Figure 5.2a. The red-highlighted rectangular region at the bottom denotes the thermodynamic stability region ($E_b < 0$), wherein most of the investigated configurations exhibit good stability, with the exception of the BiN_3 structure that possesses a positive E_b and has therefore been excluded from further evaluation. Figure 5.2b reports the Bader charge of various models plotted as a function of their corresponding carbon content within the first-shell coordination sphere. Notably, a linear scaling relation is observed in four-atom coordinated Bi models, and an increase in the C percentage results in a corresponding decrease in the Bader charge of Bi atom, whereas no clear dependence of this nature is identified in the case of three-atom coordinated models. Electron-enriched Bi centers have been reported to exhibit higher activity toward FA conversion,[147] pointing to the feasibilities of coordination engineering for achieving higher FA productions.

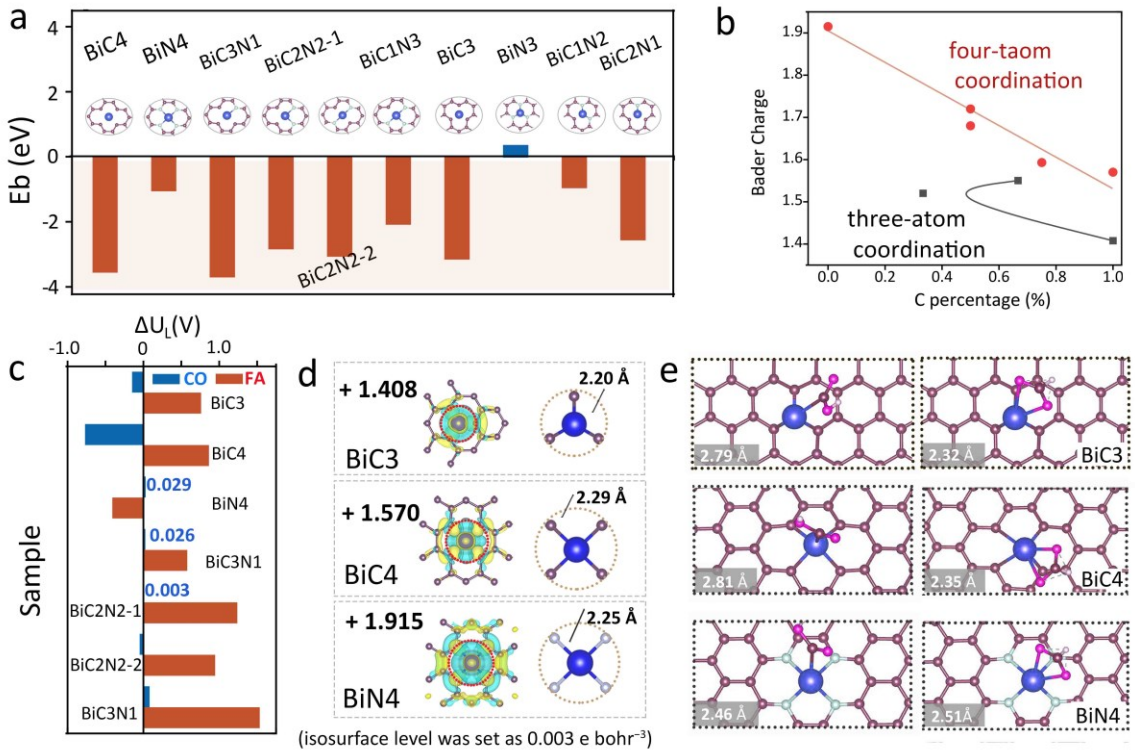

Figure 5.2 (a) DFT calculated E_b of Bi SAs trapped by various defective sites. Ten different models with Bi SAs occupying either single or double vacancies were evaluated (color, purple: carbon; blue: bismuth; silver: nitrogen). (b) Bader Charge as a function of the concentration of C atoms in all the first shell coordinated atoms. (c) DFT predicted ΔU_L over the surfaces of all models. Both CO2-to-FA (red) and CO2-to-CO (blue) pathways were computed. (d) DFT optimized Bi-C/N bond length and Bader charge analysis of BiC3, BiC4 and BiN4 (cyan and yellow regions refer to electron depletion and accumulation, respectively). (e) DFT calculated bond lengths of Bi -*OCHO and Bi -*COOH intermediates over BiC3, BiC4 and BiN4.

To gain the theoretical insights at the atomistic level, the Gibbs free energy diagrams of CO_2RR and HER were simulated on the basis of the well-accepted CHE model to elucidate the structure-function correlations of Bi-based SACs.[18,20] The complete Gibbs free energy diagrams of the three

reaction pathways, including CO_2-to-FA, CO_2-to-CO and H_2O-to-H_2 (HER) with the critical intermediates of *OCHO, *COOH/*CO and *H, were computed to provide an overview of the CO_2RR and HER reactions (Figure S5.1). We utilize the ΔU_L between CO_2RR (both FA and CO) and HER, defined as $\Delta U_L = U_L(CO_2RR) - U_L(HER)$, as a descriptor to compare their preferred occurrence, and higher CO_2RR selectivity is indicated by a more positive ΔU_L.[148] As depicted in Figure 5.2c, in order to selectively catalyze a particular reaction, the target catalysts should possess a positive ΔU_L value for that specific reaction. According to this criterion, BiC3 and BiC4 apparently stand out for the CO_2-to-FA reaction. BiC2N2-2 also meets the requirement, albeit with a less negative ΔU_L for CO. BiN4 appears to be the only viable catalyst suitable for the CO_2-to-CO reaction. Consequently, our attention is directed toward three exemplary catalysts, namely, BiC3, BiC4 and BiN4, for which the Bader charge distributions and DFT-optimized bond distances of Bi-C or Bi-N within the first coordination shell are depicted in Figure 5.2d.

In more details, the $*CO_2 \rightarrow$*OCHO conversion is determined as the endothermic process in both BiC3 and BiC4 samples, and their RDS have been identified as the production of *OCHO with the energy barriers of 0.58 and 0.62 eV, respectively, both are lower than the energy required to produce*COOH (1.50, and 2.26 eV, respectively). In addition, the second elementary step is barrierless over the BiC3 and BiC4 samples, thus confirming the favourable production of FA over CO at carbon-bound Bi centers. The binding of Bi atoms to the two O atoms in *OCHO is favored over binding to a single O atom, with an energy difference of 0.41 eV (taking BiC4 as an example), while Bi atom tends to coordinate with one C atom in *COOH. In contrast, $*CO_2 \rightarrow$*OCHO becomes downhill over BiN4 (-0.85 eV), and the further protonation of *OCHO to yield desorbed FA requires an energy of 1.05 eV. We further compare the CO_2-to-CO route over BiC3, BiC4 and

BiN4. The first elementary step to produce *COOH in the reaction is endothermic and is the RDS in all the studied models; the energy penalties associated with the *COOH generation over BiN4, BiC3, and BiC4 samples are 0.61, 1.50, and 2.26 eV, respectively. The second and third elementary steps from *COOH to *CO and the subsequent *CO release are exergonic over all the samples. The electronic interactions between Bi centers and intermediate species during the reaction are further rationalized by finding the bond lengths between the two components, with shorter distance predicting the stronger interactions. As demonstrated in Figure 5.2e, the BiC3 (2.32 Å) and BiC4 (2.35 Å) exhibit the shorter Bi-O (*OCHO) bond distance compared to BiN4 (2.51 Å), clearly indicating the enhancement of Bi-O interactions on BiC3 and BiC4. In contrast, the Bi-C (*COOH) bond lengths of both BiC3 (2.79 Å) and BiC4 (2.81 Å) are comparably longer than that of the BiN4 (2.46 Å), which points to the more enhanced interplay between BiN4 and *COOH. Furthermore, the orbital interactions between Bi centers and *OCHO/*COOH intermediate are examined by plotting the projected density of states (PDOS) of Bi p orbitals and *OCHO/*COOH over BiC3, BiC4 and BiN4, as shown in Figure 5.3. The Bi p orbitals, rather than the d orbitals which are commonly adopted for transition metals, were chosen based on the previous studies in which good correlations between the p orbital and *OCHO adsorption had been described over Bi surface.[109,149] As is shown, the interaction of *OCHO and Bi is stronger in BiC3 and BiC4 than in BiN4, as evidenced by the much larger overlapping area (*S*) of Bi p orbitals and *OCHO (*S* = 0.435 and 0.450 in BiC3 and BiC4, respectively). Additionally, the sharp coupling peak near Fermi energy level further manifests the preferred hybridization between Bi p orbital and *OCHO and thus the enhanced electronic interactions between Bi-C and *OCHO.[134] Consequently, the Bi centers in the BiC3 and BiC4 display stronger Bi-*OCHO interplay that benefits the charge transfer *via* the

Bi-O bond. Likewise, the larger orbital peak overlap of Bi-*COOH alongside the near-Fermi level coupling peaks in BiN4 (compared to those of the BiC3 and BiC4) collectively points to the more efficient charge transfer between Bi center and *COOH intermediate in BiN4 catalysts.

Based on this analysis, it becomes known that tuning the microenvironment around Bi centers can substantially influence the electronic interplay between central Bi atoms and the matrix, leading to different hybridizations between Bi and intermediates and therefor enabling the distinct catalytic capabilities of Bi SACs.

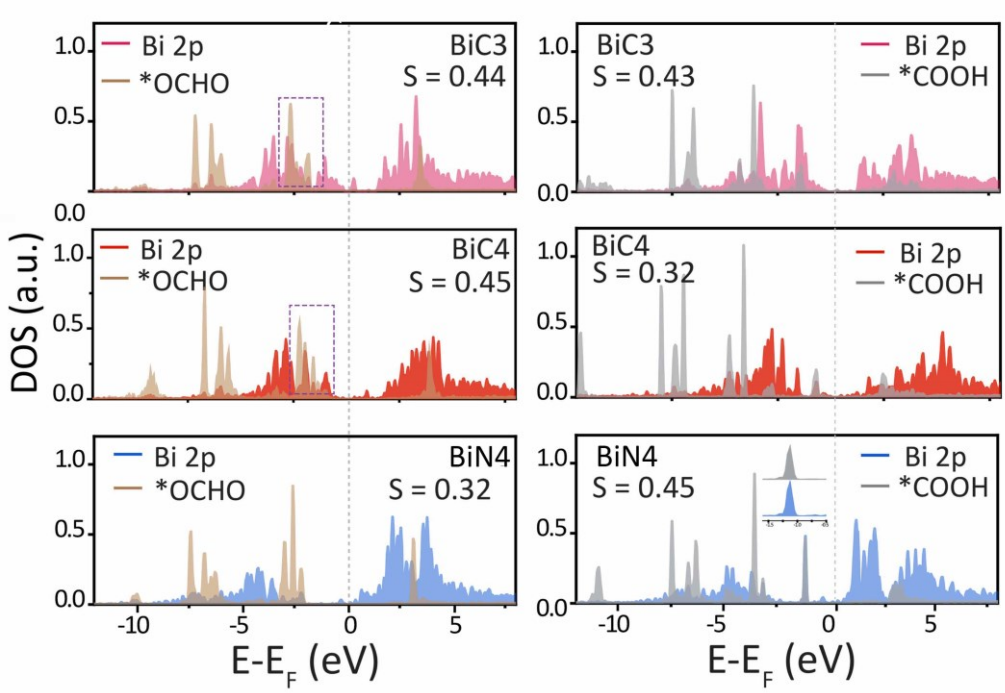

Figure 5.3 PDOS of Bi p orbitals and *OCHO and *COOH and their overlapped area after the adsorption of the two species over BiC3, BiC4 and BiN4.

To achieve a rational synthesis of the catalysts, we devised a systematic, two-step method that comprised of wet impregnation of a predetermined amount of metal ions precursor solutions onto carbonaceous matrix, followed by vacuum drying. The metal salt-impregnated carbon

supports were further subjected to high-energy laser pulses to decompose and reduce the metal ions (Figure 5.4).

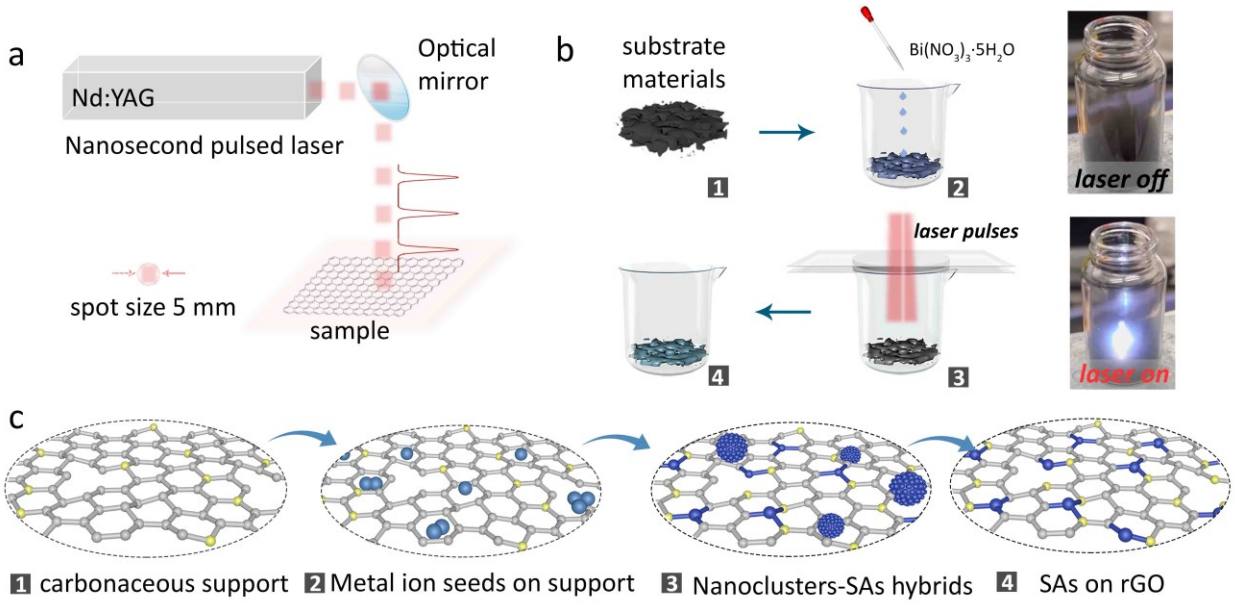

Figure 5.4 (a-c) Schematic illustration of (a) the laser setup, (b) the synthesis procedure (picture: the real-life images captured during laser irradiation) and (c) the evolution of "metal ion loaded graphene" hybrids during laser shocks.

The nanosecond pulse laser with a wavelength of 1064 nm was operated at the pulse duration of 5 ns. The spot size of the laser beam could be adjusted by changing the distance between the focus lens and the sample surface. The optimized spot size of the laser beam was 5 mm, and the laser pulse energy was 620 mJ to produce a power density of 0.64 GW cm^{-2}. The feasibility of this laser confinement strategy roots in the efficient adsorption of the photon energy and conversion to heat by graphene-based support, allowing for the creation of a transient and localized region with alternating heating and quenching environment as the laser switches on and off. The temperature rise was observed when reaching above 1500 K, thereby promoting the instant

reduction and nucleation of metal cations.[150] Due to the band structure of graphene, electrons from the valence band were excited to the conduction band when laser pulses were absorbed by graphene, leading to the ejection and liberation of electrons which further drive the reduction of metal cations through Auger-like mechanisms.[151] The digital images captured the graphene powder movement and the emergent of bright light resulted from the thermionic emission induced by laser stimulation. The method was firstly exemplified using 0.004 M of $Bi(NO_3)_3{\cdot}5H_2O$ as the Bi source, pristine or nitrogenated graphene as substrates (denoted as C and NC, respectively). To analyze the crystalline phase of the laser-treated samples, XRD was performed, as depicted in Figure 5.5. The broad peaks in the XRD spectra suggest the limited crystallinity and low concentrations of the Bi-related phases, which cannot be accurately indexed as metallic or Bi oxides. These samples are denoted as BiOx-C ($0 \leq x \leq 1.5$) for pristine graphene and BiOx-NC for nitrogenated graphene considering that surface Bi atoms would preferably coordinate with oxygen atoms due to their oxyphilic nature.

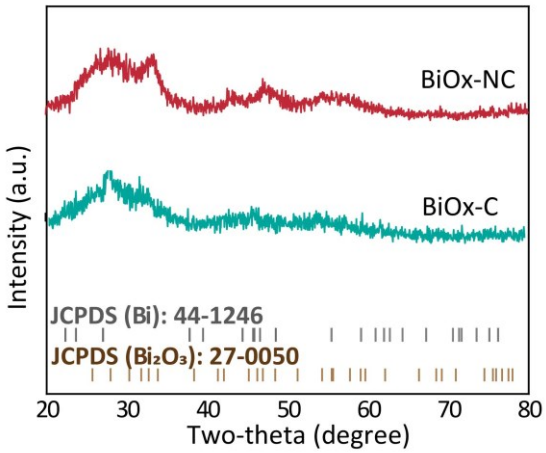

Figure 5.5 XRD patterns of as-synthesized BiOx-NC (red) and BiOx-C (green). The standard XRD patterns of Bi (JCPDS: 44-1246) and Bi_2O_3 (JCPDS: 27-0050) are provided for reference.

The morphologies of the catalysts were then analyzed using high-angle annular dark-field scanning transmission electron microscopy (HAADF-STEM), as illustrated in Figure 5.6. The images exhibit the presence of sub-5nm nanoclusters alongside a substantial number of bright atoms distributed on the free-standing nanosheets, which are discernable due to the different Z contrasts of Bi and adjacent light elements. The mean diameter of the luminous spots was determined to be 0.289 nm (with the diameter of a single Bi atom being 0.230 nm), thereby substantiating that the isolated dots are Bi SAs. Cluster-free Bi SAs samples can be obtained by refluxing BiOx-C and BiOx-NC with 0.5 M H_2SO_4, denoted as Bi-C and Bi-NC, respectively. HAADF-STEM images (Figure 5.6c and 5.6g) in conjunction with EDX elemental mappings in TEM (Figure 5.6d and 5.6h) further evidence the prevalence of Bi SAs across the entire architectures with a high degree of homogeneity and uniformity, reinforcing the excellent stability of Bi SAs against acid leaching. The loading mass of Bi has been measured using ICP-OES (Table S5.1). The slightly higher loading concentrations of Bi has been observed when using NC as the substrate, which can be attributed to the increased number of defects resulted from the introduction of N dopants to graphene. This is critical to stabilize and anchor the metal cations.

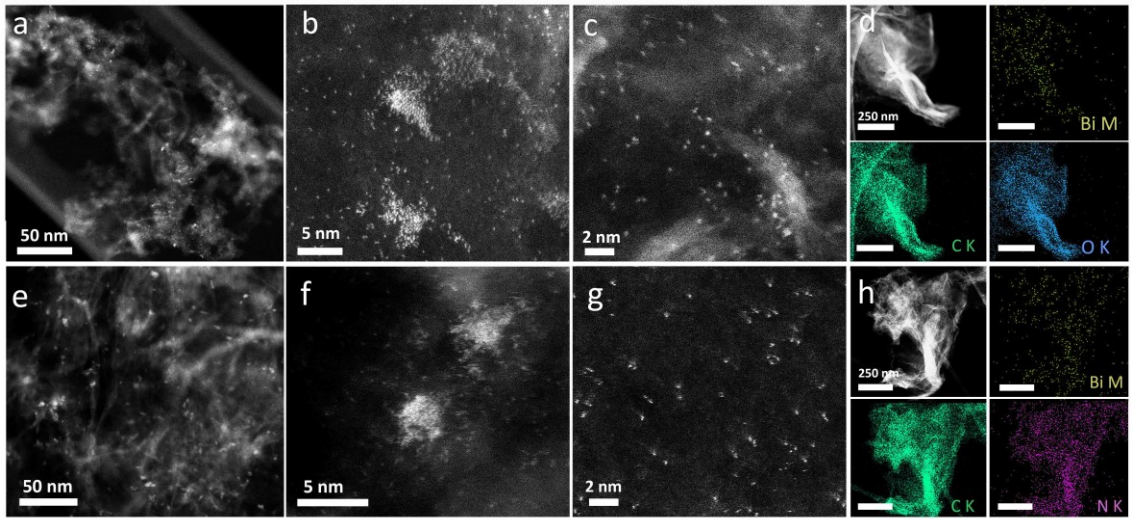

Figure 5.6 (a-c, e-g) HRTEM images of (a-c) Bi-C and (e-g) Bi-NC. (d, h) The corresponding EDX mappings of (d) Bi-C and (h) Bi-NC.

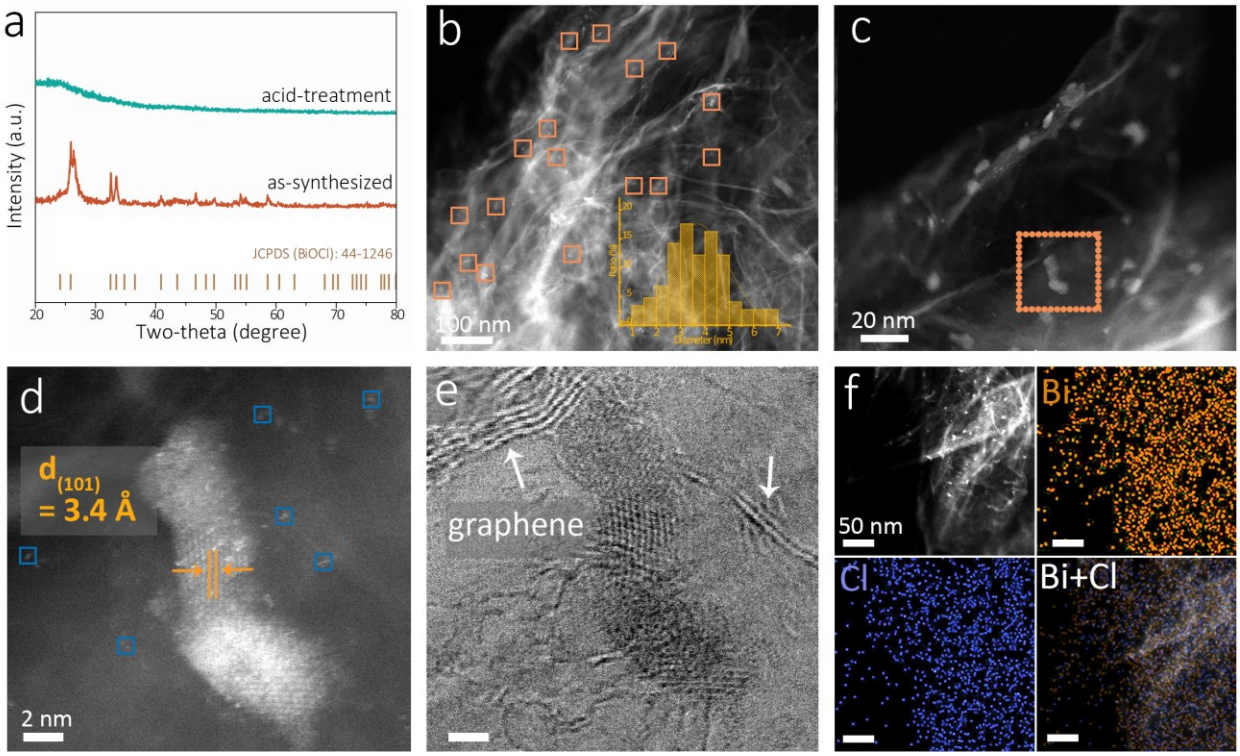

Figure 5.7 (a) XRD pattern of the sample before and after acid washing. (b-e) HAADF-STEM images. (f) The corresponded EDX mappings of Bi and Cl elements.

In the next series of experiments, the $Bi(NO_3)_3{\cdot}5H_2O$ precursor solution was substituted with $BiCl_3$ while keeping other parameters unchanged to investigate the possible impact of the precursor type on materials synthesis (Figure 5.7). The XRD peaks acquired from the irradiated $BiCl_3$/C exhibit the enhanced crystallinity and narrower width which can be unambiguously ascribed to the BiOCl phase, in contrast to the broad peak feature and low crystallinity obtained over $Bi(NO_3)_3{\cdot}5H_2O$/C. This phenomenon can be explained by the hydrolysis of $BiCl_3$ in the presence of atmospheric moisture.[152] The coexistence of Bi SAs and BiOCl clusters with the (101) facet exposed has been revealed by HR-TEM and EDX mapping, whereas no well-defined lattice plane has been identified in $Bi(NO_3)_3{\cdot}5H_2O$/C samples. It appears that the type of metal ions precursor has a significant role to play on the phase and crystallinity of the nanocrystals, while the generation of metal SAs is comparatively less influenced. The effectiveness of our method was also demonstrated using $BiCl_3$-CNTs (carbon nanotubes) and $BiCl_3$-CB (carbon black) precursor hybrids (Figure 5.8). As anticipated, a combination of Bi nanoclusters and SAs can be observed. Nevertheless, considering that the Cl source in $BiCl_3$ may be co-doped into the graphene lattice, the $Bi(NO_3)_3{\cdot}5H_2O$ precursor solution was chosen in order to exclude any possible interference with the graphene compositions.

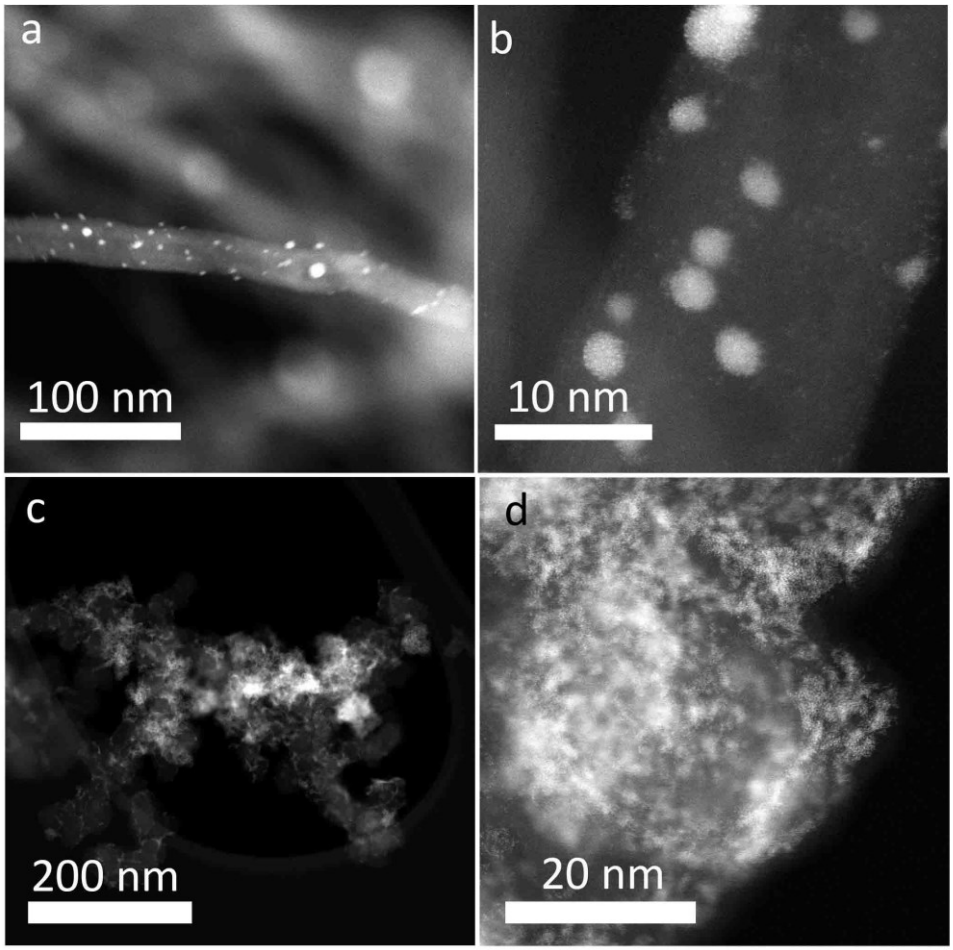

Figure 5.8 (a, b) HAADF-STEM images of Bi loaded on carbon nanotubes (Bi-CNTs) and (c, d) Bi loaded on carbon spheres (Bi-CS).

Compared to the traditional high-temperature annealing methods for catalyst synthesis, the laser treatment confers unique self-etching capabilities that promote the stabilization of metal atoms through the strong covalent bonds with neighboring defects generated *in situ*.[153] More specifically, graphene-based substrates tend to undergo etching in the presence of loaded metal ions, resulting in the generation of more defects.[154] In the annealing process, auxiliary etching agents are oftentimes required to modify the carbonaceous substrates to introduce more

defects,[55] whereas the ultrafast laser bombardment circumvents this requirement, reducing the metal ions and producing defects in a straightforward and simultaneous manner, as substantiated in the following Raman analysis, using the $Bi(NO_3)_3{\cdot}5H_2O/C$ sample as an example. As shown in Figure 5.9, the I_D/I_G values, which indicate the degree of defects (I_D at around 1355 cm^1 and I_G at around 1580 cm^{-1}), were determined as 0.78, 0.88 for the untreated C and NC powders, respectively, and these values increase to 0.95 and 0.99 after laser treatment in BiOx-C and BiOx-NC, respectively, indicating the creation of rich defects in the samples upon laser dosages. In brief, the ultrafast laser shock method proves to be an efficient means of synthesizing either SACs materials or cluster-SACs hybrids with flexible metal-substrate combinations within a short period of time, offering a promising path toward the fabrication of the SACs-based catalysts tailorable for various catalytic processes.

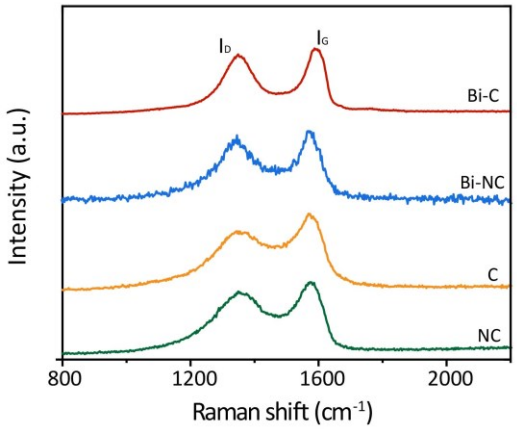

Figure 5.9 Raman spectra of Bi-C, Bi-NC, C and NC, and the corresponded ID/IG values.

To investigate the surface chemistries and electronic properties of the Bi atoms in the as-obtained samples, XPS was conducted, as shown in Figure S5.2. The high-resolution Bi 4f scans exhibit two peaks at the binding energies of 165.0 and 159.7 eV in BiOx-C; these peaks slightly shift to 165.4 and 160.0 eV in BiOx-NC, owing to the different electronegativities of N and C

elements. In parallel, these peaks appear at 164.4 and 159.1 eV in Bi-C, and slightly shift to 164.8 and 159.4 eV in Bi-NC. These results may indicate that the C atom(s) coordinated to the Bi SA, if any, have been partially substituted by N atom(s), resulting in an elevated oxidation state of $Bi^{\delta+}$ ($0 < \delta < 3$) species caused by the electron flow from Bi to N atoms. Hence, the individual Bi atoms in Bi-C and Bi-NC may possess varying coordination environment based on the choice of C or NC as supports.

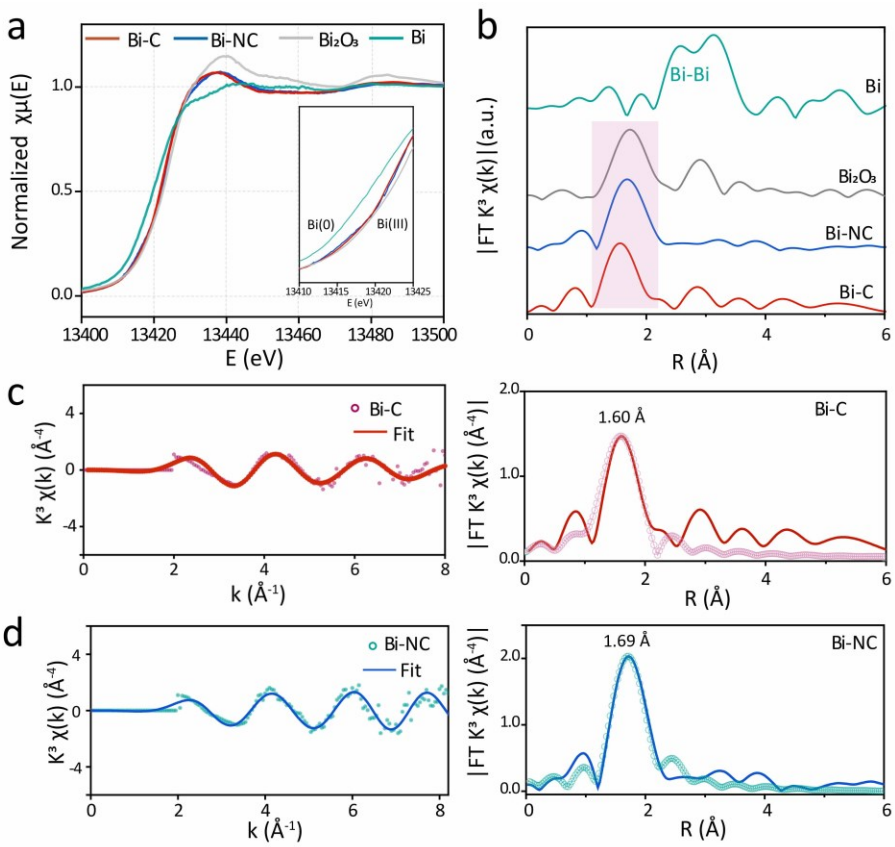

Figure 5.10 (a) Bi L-edge XANES spectra of Bi-C, Bi-NC, Bi_2O_3 and metallic Bi references (inset shows the enlarged near-edge patterns). (b) Fourier transformed κ3-weight EXAFS spectrum of Bi-C, Bi-NC, Bi_2O_3 and metallic Bi. (c, d) Fourier transformed κ3-weight EXAFS spectrum with the best fitting results of (c) Bi-C and (d) Bi-NC, respectively.

However, there is no direct evidence suggesting the Bi-C or Bi-N coordination species from XPS results, probably due to the low concentration of Bi atoms. To further gain insights into the electronic properties and local geometries of Bi-C and Bi-NC, XANES and EXAFS were performed. To semi-quantitatively determine the Bi oxidation states, the absorption edges of Bi-C and Bi-NC at $\mu = 0.5$ are adopted and compared with references of Bi and Bi_2O_3 (Figure 5.10a).[155] The adsorption edges of both Bi-C and Bi-NC situate between the Bi powder and Bi_2O_3 references, implying the low-valency of $Bi^{\delta+}$ ($0 < \delta < 3$). Moreover, the Bi-C spectrum slightly shifts toward lower energy compared to that of the Bi-NC, thus pointing to lower oxidation states of Bi atoms in the Bi-C powder. The intensities of the white lines in the spectra of Bi-C and Bi-NC also fall between the references of Bi and Bi_2O_3, providing additional evidence for these conclusions on oxidation states, consistent with the XPS analysis. FT-EXAFS spectra of Bi-NC, Bi-C and the reference Bi and Bi_2O_3 powder are plotted and analyzed to elucidate the possible structural information of Bi SAs (Figure 5.10b). The EXAFS of R-space for Bi powder reveals two the predominant peaks located at 2.59 and 3.21 Å, assigned to the scattering of Bi-Bi interatomic feature.[156] The absence of metallic Bi-Bi signals and the presence of only primary peaks located at 1.60 Å in Bi-C and 1.69 Å in Bi-NC suggest the discrete dispersion of Bi in both samples. The predominant peak in the FT-EXAFS spectrum of Bi-C symbolizes the scattering trajectory of Bi and its proximal light elements and can be attributed to the scattering of the Bi-C bonds. The major peak in the Bi-C spectrum shows a slight shift toward the lower energy compared to that of the Bi-NC, signifying a reduction in the first-shell scattering distance in the former samples. Although EXAFS method is not able to differentiate between N and C atoms in the first coordination sphere, the predominant peak can be tentatively associated with the first shell Bi-C path due to its

comparatively shorter distance, as simulated by DFT simulations (Table S5.2).[157,158] Due to the variability in the coordination environment of Bi, it is insufficient to accurately determine the fine structures of Bi-C and Bi-NC solely through EXAFS. Therefore, a combination of the EXAFS modeling and DFT calculations was performed to quantitatively assess the bond lengths and the coordination numbers around the central Bi atoms in Bi-C and Bi-NC (Figure 5.10c and Figure 5.10d). The results of the simulations are summarized in Table S3 in terms of fitting parameters, such as bond lengths, coordination numbers, and Debye Waller factors. The simulations indicate that a Bi atom in Bi-C is directly coordinated with C and the best fitting coordination number is 3.73 ± 0.17, indicating the coexistence of BiC3 and BiC4 species in Bi-C as the EXAFS is an average result. Therefore, we cautiously assign the primary peak at 1.60 Å to the Bi-C bonds. In the case of Bi-NC, the optimized fittings show that Bi center is coordinated by four N atoms (BiN4), leading to a coordination number of 4.02 ± 0.21. In a nutshell, the agreement among DFT calculations, XAFS and XPS findings unambiguously confirms the successful synthesis of Bi SACs with Bi-C and Bi-N coordination structures. In the following discussions, we use Bi-C for BiC3 and BiC4 samples, Bi-NC for BiN4 for simplicity.

The electrochemical performances of the Bi-C, Bi-NC, BiOx-C and BiOx-NC electrodes were evaluated in a gas-tight H-type cell using $KHCO_3$ as the electrolyte. CV scans were firstly performed in argon-saturated 0.1 M $KHCO_3$ electrolyte to probe the Bi^{3+}/Bi^0 redox capabilities (Figure 5.11). The well-defined redox peaks at approximately 0.50 and -0.06 V are attributed to the Bi^{3+}/Bi^0 conversions. These characteristic peaks are discernible over BiOx-C and BiOx-NC but are absent in the Bi-C and Bi-NC electrodes. This is due to the low concentrations of Bi species, in line with the characteristic “single atom” features in the Bi-C and Bi-NC samples. The absence of

the Bi^{3+}/Bi^0 redox peaks promoted us to compare the ECSA of Bi-C and Bi-NC electrodes by utilizing their C_{dl} values, which were extrapolated from the slope of the "Δj/2 – scan rate" plot acquired in non-Faradaic region. The Bi-C and Bi-NC apparently possess larger electrochemical surface areas (ECSA) values compared to the Bi-free substrates, suggesting the enhancement of ECSA by the incorporation of Bi heteroatoms. It is worth mentioning that the catalytic activity/selectivity of electrodes are not necessarily dependent on their ECSA values,[74,159] thus, more detailed characterizations need to be carried out to comprehensively evaluate the CO_2RR performances of Bi-C and Bi-NC.

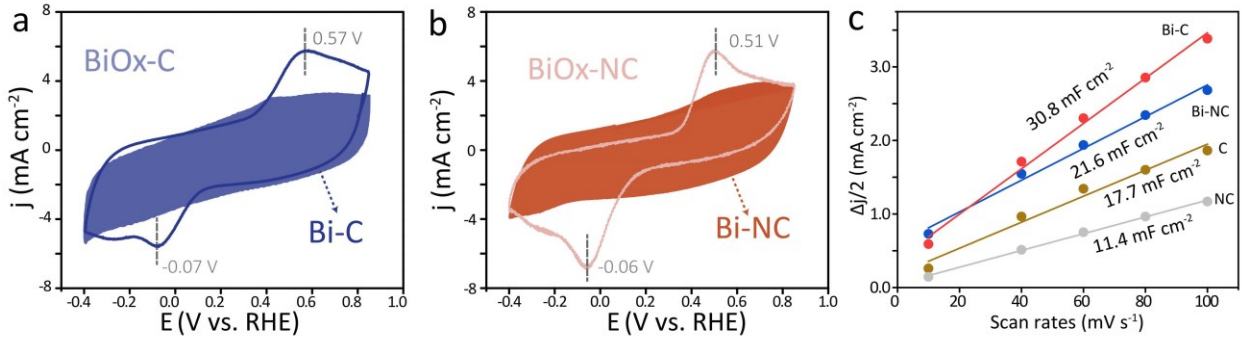

Figure 5.11 (a, b) CV scans of BiOx-C and Bi-C (a), and BiOx-NC and Bi-NC (b) at a scan rate of 20 mV s^{-1} in argon-saturated 0.1 M $KHCO_3$. (c) C_{dl} values of Bi-C, Bi-NC, C and NC electrodes.

Next, LSV was carried out in CO_2-saturated 0.1 and 0.5 M $KHCO_3$ electrolytes to distinguish the activities of the four samples (Figure 5.12a). The Bi-C and Bi-NC electrodes display considerably higher current responses and thus higher overall activities compared to BiOx-C and BiOx-NC electrodes, including both CO_2RR and HER, when the external potential surpasses -0.8 V. The potential-dependent FE toward the gas and liquid products in CO_2RR, obtained from the average of three independent tests, are presented in Figure 5.12b which highlights significant differences

in product distributions. To begin with, in 0.5 M $KHCO_3$, the Bi-C electrodes show overall high selectivity toward CO_2RR-to-FA conversion. Raising the potential from -0.7 to -0.9(5) V results in an enhancement in the FE_{FA} from 47.1 ± 1.2 % to 82.6 ± 0.3 % (peak value) on Bi-C, while further increasing the potentials from -0.9(5) to -1.2 V leads to the decline in FE_{FA} alongside the promotion of FE_{H_2}. In contrast, Bi-NC demonstrates limited selectivity toward FA with the maximum FE_{FA} of less than 33 ± 2.1 % (at -1.0 V), significantly lower than that of the Bi-C. As the external potential shifts more anodically, we start to observe a promotion of CO over Bi-NC, reaching the maximum FE_{CO} of 81.8 ± 3.0 % at - 0.5 V. The selectivity toward CO is even more enhanced when switching the 0.5 M $KHCO_3$ to 0.1 M $KHCO_3$, wherein the peaking FE_{CO} of 90.8 ± 2.6% at - 0.5 V alongside an ultrasmall overpotential of 0.190 V with appreciable FE_{CO} onset of 70.3% can be detected, accompanied by negligible amount of FA (less than 2.6%) over the entire measured potential range. On the other hand, the maximum FE_{FA} on Bi-C drops to 57.4 ± 0.1 % at a potential of - 1.0 V with a simultaneous increase in FE_{H_2} in 0.1 M $KHCO_3$, probably owing to the insufficient proton activation in more diluted electrolytes.[160]

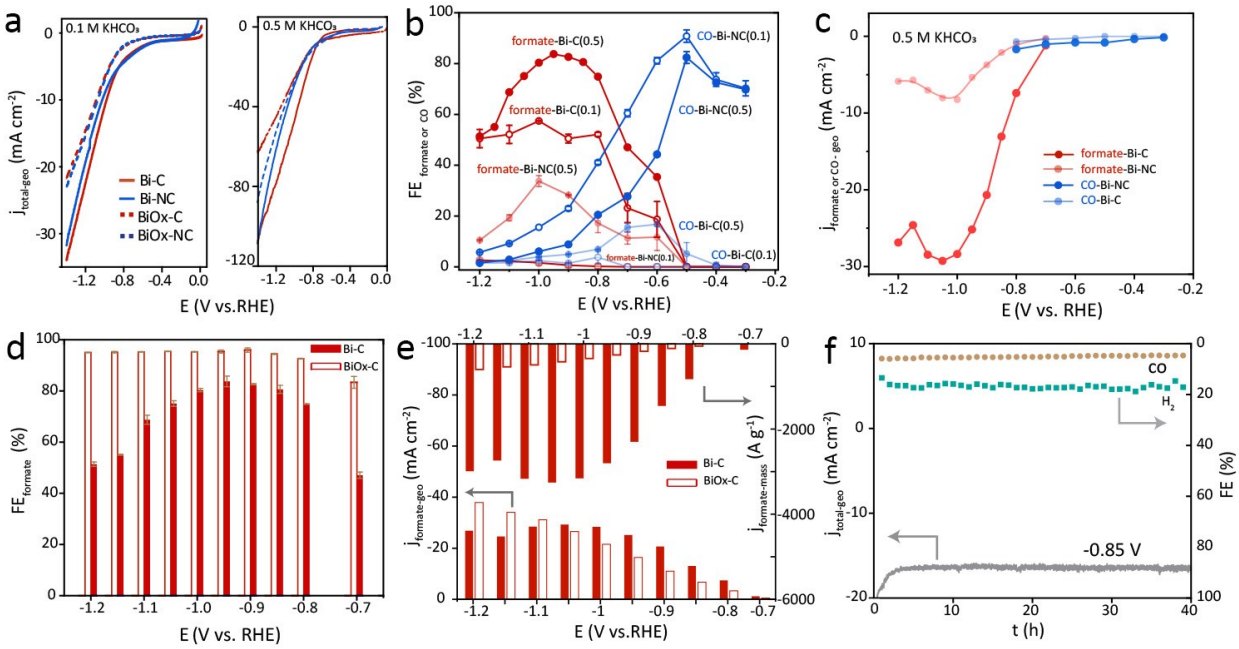

Figure 5.12 (a) LSV curves of BiOx-C, BiOx-NC, Bi-C and Bi-NC electrodes in CO_2-saturated 0.1 and 0.5 M $KHCO_3$. (b) FEs of FA or CO obtained over Bi-C and Bi-NC in either 0.1 or 0.5 M $KHCO_3$. (c) j_{FA-geo} and j_{CO-geo} of Bi-C and Bi-NC electrodes acquired in 0.5 M $KHCO_3$. (d) FE_{FA} obtained over BiOx-C and Bi-C in 0.5 M $KHCO_3$. (e) j_{FA-geo} and $j_{FA-mass}$ of BiOx-C and Bi-C electrodes acquired in 0.5 M $KHCO_3$. (f) Long-term stabilities of Bi-C at a cathodic potential of - 0.85 V in 0.5 M $KHCO_3$.

It has been noticed that the area-specific current densities decrease considerably in 0.1 M $KHCO_3$, contributing to the decreased production rates over both FA and CO, albeit the apparent enhancement of FE_{CO} achieved in this case. Since the production rate is an important metric attesting the performance and potentials for industrialization of a catalyst, we further calculate the partial current densities of FA or CO obtained in 0.5 M $KHCO_3$, normalized by the geometric area of the electrodes (j_{FA-geo} or j_{CO-geo}), and the results are presented in Figure 5.12c. Bi-C clearly stands out as the best catalyst driving the FA production with the maximum j_{FA-geo} of -

29.3 mA cm^{-2} at -1.05 V. The Bi-NC, on the other hand, demonstrates the higher j_{CO-geo} at more positive potential ranges (i.e., -0.3 - -0.7 V) but with insignificant values.

Subsequently, we compare the performance of Bi-C to BiOx-C electrodes with the anticipation that the latter sample would also exhibit good catalytic properties, as suggested by previous research highlighting the potentials of Bi-based clusters/bulk materials.[161,162] As shown in Figure 5.12d, both Bi-C and BiOx-C show overall appreciable selectivity toward CO_2RR-to-FA conversion. On BiOx-C, the formation of FA accounts for more than 90% of the total FEs across a wide potential range of -0.8 to -1.2 V, with only minor amounts of CO and H_2 (less than 5%) in presence. Regarding j_{FA-geo}, the Bi-C exhibits the highest j_{FA-geo} between cathodic potentials of -0.7 to -1.05 V, as illustrated in Figure 5.12e. As the potential decreases further to -1.2 V, the j_{FA-geo} plateaus and then slightly decreases probably due to mass transfer limitations. On the other hand, the j_{FA-geo} of BiOx-C continues to grow as the potential shifts more negatively, exceeding that of the Bi-C at -1.1 V. We postulate that these disparities can be attributed to the different concentrations of Bi in the BiOx-C and Bi-C samples. It is generally acknowledged that highly negative potentials can significantly enhance the charge transfer and reaction kinetics of FA, thus resulting in a state of saturation for the number of available sites in Bi-C when the potential surpasses -1.05 V. Conversely, in the case of BiOx-C, a surplus of sites for CO_2 adsorption and turnover remains available. Therefore, the j_{FA-geo} of BiOx-C keeps increasing even when further reducing the potentials. In addition, Bi-C exhibits the highest FA partial current density normalized by mass ($j_{FA-mass}$), thus indicating the highest cost-effectiveness of the Bi-C. In order to estimate the intrinsic activities of Bi atoms in Bi-C, the TOF was calculated based on the total mass of Bi (Figure 5.13). The results reinforce the high intrinsic activity of Bi atoms in the Bi-C for

the CO_2-to-FA conversion with the TOF of Bi-C reaching a peak value of 2.6 s^{-1} at -1.05 V. Considering the much higher current densities achieved in 0.5 M $KHCO_3$ electrolyte and the high activities of CO_2-to-FA conversion over Bi-C, the long-term stability has been assessed over a period of 40 hours (Figure 5.12f). The results reveal that the Bi-C catalyst demonstrates appreciable long-term durability, maintaining an average FE_{CO} (ca. 2.5%) and FE_{H_2} (ca. 18%) values with the average total current density of -16.5 mA cm^{-2} and achieving a total FE_{FA} of 81.2% at the end of the measurement. The obtained total FE_{FA} is slightly higher than the FE_{FA} measured during potentiostatic analysis, which could be the systematic error from different batches of samples.

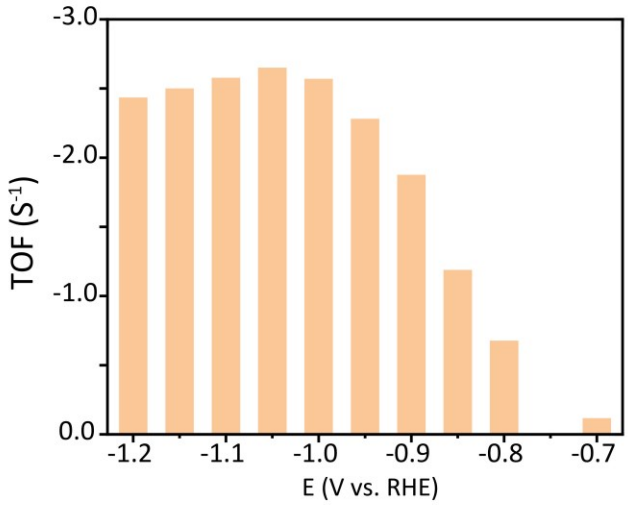

Figure 5.13 TOF of Bi-C at various applied potentials.

5.3. Supporting information

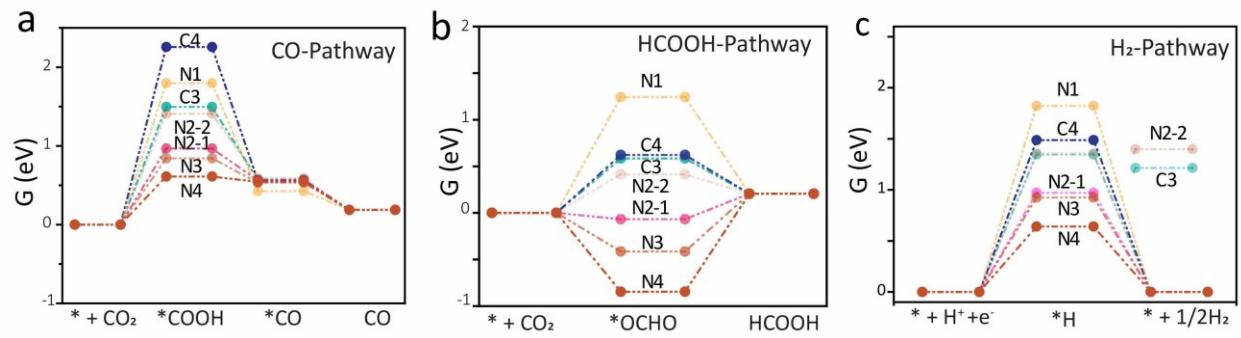

Figure S5.1 DFT computed Gibbs free energy of the individual reaction steps of CO, FA, and H_2 pathway over ten different Bi SACs models.

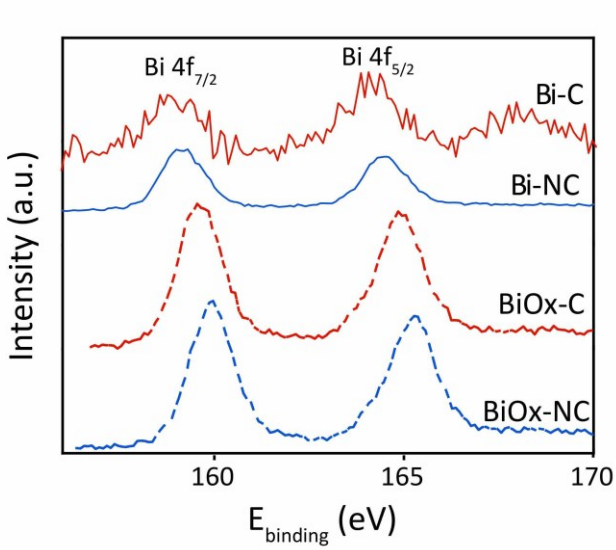

Figure S5.2 XPS analysis of BiOx-C, BiOx-NC, Bi-C and Bi-NC.

Table S 5.1 Bi loading mass of BiOx-C, BiOx-NC, Bi-C and Bi-NC.

Sample	Loading Mass (w.t.%)
BiOx-C	6.3 %
BiOx-NC	8.8 %
Bi-C	0.9 %
Bi-NC	2.1 %

Table S 5.2 EXAFS fitting parameters for Bi-NC and Bi-C.

Sample	Scattering Path(s)	CN	R (Å)	σ^2 (10^{-3}Å^2)	ΔE_0 eV)	R factor
Bi-NC	Bi-N	4.02 $\pm$ 0.21	2.25$\pm$ 0.06	13	-6	0.008
Bi-C	Bi-C	3.73 $\pm$ 0.17	2.29 $\pm$ 0.025	6	-2.3	0.005

Chapter 6. Volcano-shaped Carbon Dioxide Reduction on Cobalt Phthalocyanine with Curvature Induced Atomic Spacing Regulation

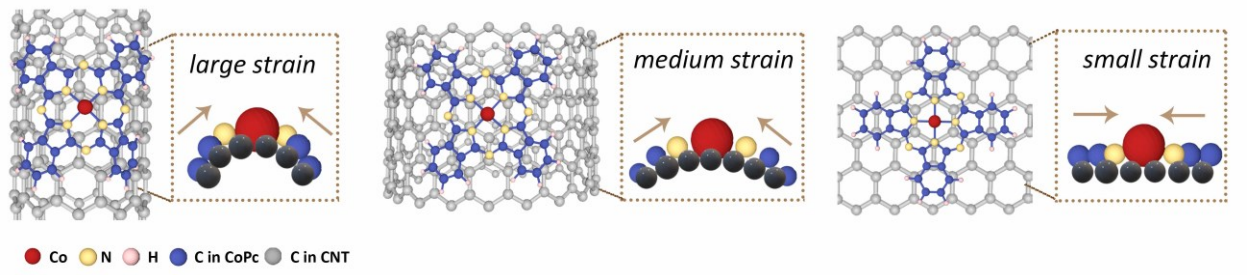

Figure 6.1 Illustration of the curvature-tuned geometric deformation in CoPc (color of the atoms: red: Co; yellow: nitrogen; light grey: carbon on the substrates; blue: carbon in CoPc).

6.1. Introduction

Electrocatalysts with the atomically distributed "metal-ligand" active centers (e.g., MNxCy, M = metal, N = nitrogen and C = carbon), mainly the metal macrocycle-based catalysts (e.g., n=metalloporphyrin, metallophthalocyanines, etc.) and inorganic SACs have been actively investigated in CO_2RR for their high catalytic activities, efficient atom utilization and low cost compared to the noble metal-based counterparts.[163] "Ideal" MNxCy generally adopts the planar, and centrosymmetric geometry with equal M-N/C bond length and N/C(1)-M-N/C(2) bond angle. In practical scenarios, however, MNxCy motif tends to deviate from the "perfect" structure and deforms, as widely observed in the materials synthesized/pyrolyzed at different temperatures,[164,165] to the MNxCy with asymmetrical coordination (different atom type and number),[166,167] and MNxCy immobilized on supports with different porosities and curvatures,[72,73] etc. Under non-static conditions, MNxCy deforms even more severely due to adsorption/desorption behaviours.[168,169] Bond length of M-N/C, among the other geometric

parameters, has been previously used as a useful indicator, predicting the CO_2RR activities. For instance, Wang et al. reported that Zn-N distances vary depending on the annealing temperature, which affect the electronic properties of Zn centers and further dictate the catalytic activities.[170] On the basis of DFT, Zhu et al. predicted that cobalt porphyrin nanotubes with larger/smaller curvatures afford longer/shorter first-shell Co-N distances, which could preferably reduce the CO_2 to CO or CH4, respectively.[72] Despite these understandings, the net effects of local structures of MNxCy on CO_2RR performance are oftentimes overlooked due to the performance enhancement brought about by other factors, mainly the ligand/coordination effects, and thus remain largely elusive.

One interpretation for the "structure-dictated" CO_2RR in the MNxCy upon geometric deformation is the "strain effect". In the simplest case, the deviations in bond length from its equilibrium state would lead to compressed/tensile MNxCy, further affecting metal-intermediate hybridizations and ultimately the CO_2RR performances, in resemble to the well-known "strain engineering" in bulk catalysts. However, strain engineering in MNxCy-based materials has been lagging mainly due to the entanglement between strain and other effects as mentioned above. The ligand effect, for instance, occurs readily when local strain is introduced *via* doping heteroatoms,[171] or annealing MOF-based precursors at various temperatures. The latter is a convenient synthesis method but tends to modify the physiochemical properties of support, the number of coordinated atoms, and/or to introduce catalytic inequivalent species (e.g., nanoclusters, etc.).[172] Many previous studies have demonstrated that the annealing temperature greatly affects the degree of the graphitization of carbon support, which changes the CO_2RR performances.[46,170] In addition, the lack of synthesis methods to achieve effective build-up of

internal strain in MNxCy as well as the limited access to advanced techniques to probe the local deformations further restrains the understanding of strain-performance relations.

In an attempt to unveil the potential links between local structures and CO_2RR in MNxCy, a series of cobalt phthalocyanine/carbon nanotubes (CoPc-CNTs) are chosen as ideal platforms in this study to introduce deformation around central Co atoms, and the magnitude is controlled by varying the radii/curvatures of the CNTs matrix. The CoPc-CNTs are prepared *via* self-assembly at room temperatures without harsh conditionings, thus preserving the intact CoN8C8 structures with identical and well-defined coordination inherited from the CoPc molecule. This eliminates any potential ligand effects caused by different coordination environment. The nonplanar distortion and symmetry reduction of this structure in CoPc can be readily interpreted as the buildup of strain around the Co centers. With this model electrocatalyst, we applied systematic and comprehensive physical and electrochemical characterizations in conjunction with DFT simulations to fully uncover their strain-function relations. A typical volcano trend over the intrinsic CO_2RR activities and the magnitude of strain around Co centres based on interatomic distance has been established, where the apex point is a mildly compressed CoN8C8 with reduced Co-N/C bond lengths. This optimal sample (Co-CNT2) yields a 1.2-fold and 2.4-fold $j_{co\text{-}ECSA}$ and TOF, respectively, at a typical potential of - 0.8 V compared to its least strained counterparts (Co-CNT4). Furthermore, it is shown that the long-term stability of Co-CNT2 has been greatly improved owing to the retarded CoPc demetallation process during CO_2 electrolysis. This study highlights and confirms the importance of controlling the internal strain and geometric distortion of catalysts in the applications of CO_2RR, which demonstrates the untapped potentials of strain engineering in MNxCy-based structures to realize further achievements in CO_2RR.

6.2. Results and Discussion

We started by optimizing the structures of CoPc/CNT and CoPc/rGO *via* DFT-based methods to provide sight into whether CNT could effectively generate deformed structures. The armchair (7*7) CNT passivated with H at the edge sites and $\sqrt{2}$ (8*5) rGO were employed to model the curved and planar substrates, respectively. Although the size of CNTs was smaller than the one in practical cases (to cope with the limited computational resources), the goal is to provide basic insights into the CoPc/support interactions, and the conclusion can serve as a basis for the rational design of Co-CNTx series with the structures of varying degree of distortion. Two typical CoPc orientations (denoted as CoPc-CNT-o1 and CoPc-CNT-o2, with a 45° difference), each with three different adsorption sites (top, bridge, and hex), were explored to determine the most energetically stable configurations.[173] As shown in Figure 6.1, the dome-shaped conformation of the CoPc molecule was obtained upon its hybridization with CNT. For Co-rGO, no apparent distortion/bending of CoPc was observed, in line with the previous studies.[173] Next, we examined the bond distance change in the first (Co-N_{1st}), second (Co-C_{2nd}), and third (Co-N_{3rd}) coordination shells of Co, and this local structure is denoted as CoN8C8 for simplicity. Using Co-rGO as the reference, we observed anisotropic bond length reductions in both Co-CNT-o1 and Co-CNT-o2, where the largest degree of bond change takes place along the radial direction (X), and the medium/moderate bond shrinkage occurs along the 45°direction (green arrows). No apparent changes were observed along axial direction (Y). Take the Co-$N1_{st}$ for example: In CoPc-rGO, the Co-$N1_{st}$ is 1.932 Å. In Co-CNT-o1, this value reduces to 1.926 Å. In Co-CNT-o2, the Co-$N1_{st}$ along X and Y direction is 1.931 and 1.914 Å, respectively. The same propensity applies to the Co-C_{2nd} and Co-N_{3rd}. The trends in bond length changes (in whichever shell) follow the same trends in the

degree of CoPc curving in the three different directions, suggesting the positive correlations between CoPc curvature and bond reduction. Therefore, we can postulate that regulating the CNT radii could effectively induce various anisotropic curvature in CoPc, leading to average bond distance reduction and thus intramolecular strain.

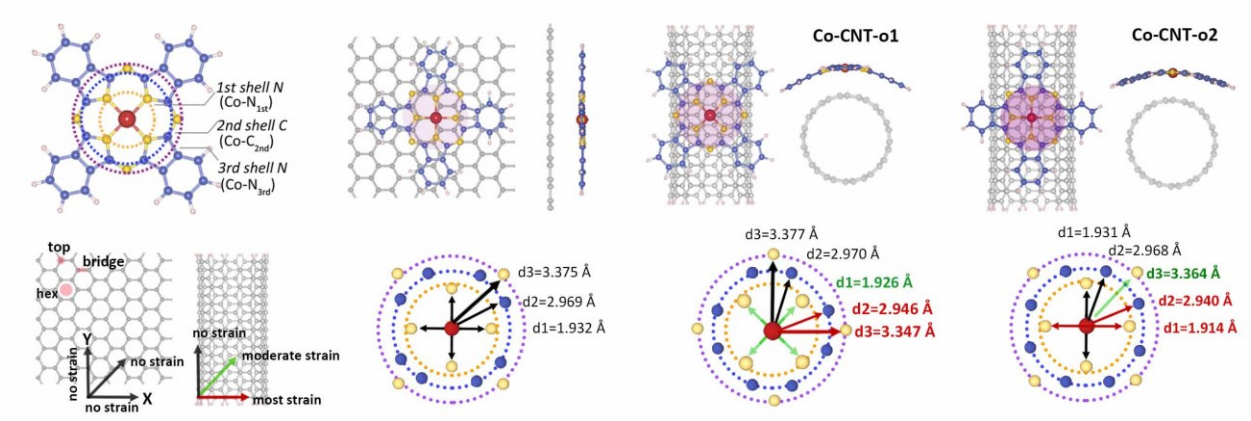

Figure 6.1 (a) Illustrations of the CoPc structure and the optimized bond distance in CoPc-rGO, Co-CNT-o1 and Co-CNT-o2. (b) Co k-edge XANES spectra, (c) enlarged Co k-edge XANES spectra at the near edge region and (d) Fourier transformed κ3-weight EXAFS spectra of CoPc and CoPc-CNTx. (e) Magnitude of the average bond distance change with respect to the equilibrated bond distance in CoPc-CNTx.

Co-CNTx electrocatalysts (x = 1, 2, 3, 4, pre-cleaned CNT with the average radii of 2, 4, 10 and 20 nm) and the control sample Co-rGO were synthesized through the hybridization of CoPc molecules and carbon substrates in dimethylformamide at room temperature and pressure.[77] Further reducing the radius of CNTs to < 1 nm leads to apparent CoPc aggregation and therefore, they are excluded in the next series of experiments. As presented in the XRD (Figure 6.2), all the as-obtained samples exhibit the characteristic diffraction peaks of CNT, and no CoPc phase has

been detected, indicating the molecular dispersion and relatively low concentration of the loaded CoPc molecules.

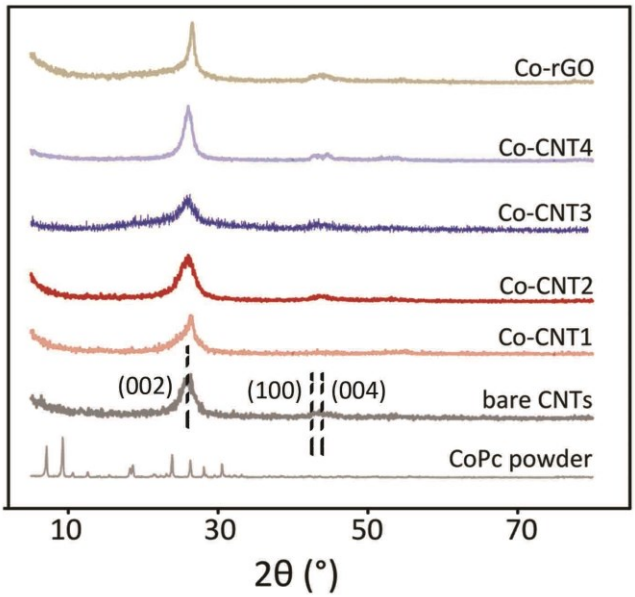

Figure 6.2 XRD spectra of Co-CNTx, Co-rGO, bare CNTs and CoPc powder.

TEM and SE-TEM discloses the aggregates-free morphologies of the electrocatalysts (Figure 6.3), which is critical (i) to reduce the inter-molecule interactions among CoPc and preserve its molecular dispersion, (ii) to guarantee efficient charge transfer between CoPc and support. The presence of the atomically distributed Co ions is confirmed by the Z-contrast AC-HAADF STEM graphs. The loading mass of Co atoms in Co-CNTx is determined ICP-OES (Table S1), suggesting a CoPc concentration of 2.0 - 3.5 nmol cm^{-2}. This is consistent with the non-stacking and monodispersing features of CoPc, which is important to understand their geometrical effects.[174,175]

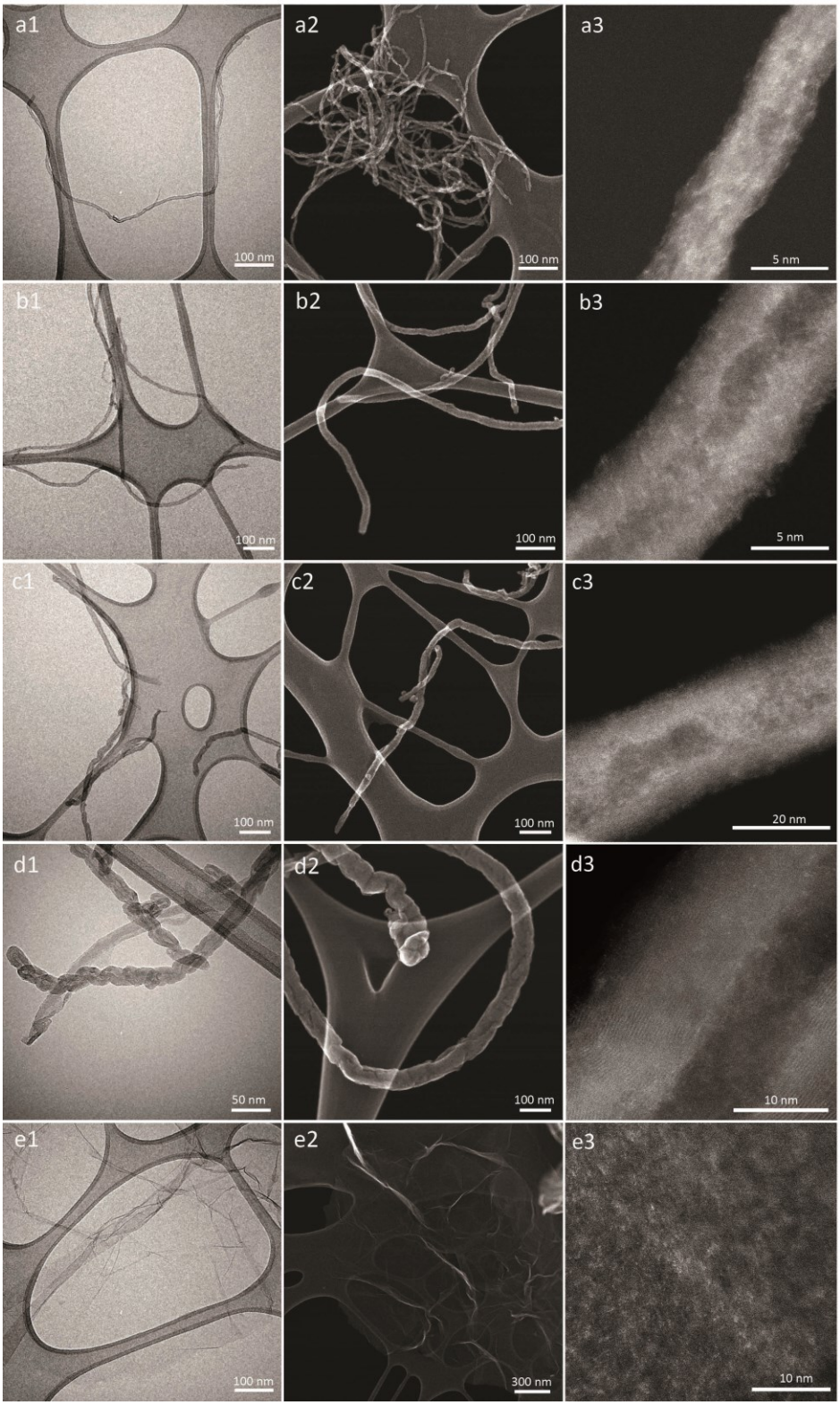

Figure 6.3 TEM and SE-TEM images of Co-CNT1 (a), Co-CNT2 (b), Co-CNT3 (c), Co-CNT4 (d) and Co-rGO (e).

Ex situ Co K-edge XAS was performed owing to its high sensitivity toward the three-dimensional atomistic arrangement around the X-ray absorber, which provides opportunities in decoding the atomic structures of around Co centers.

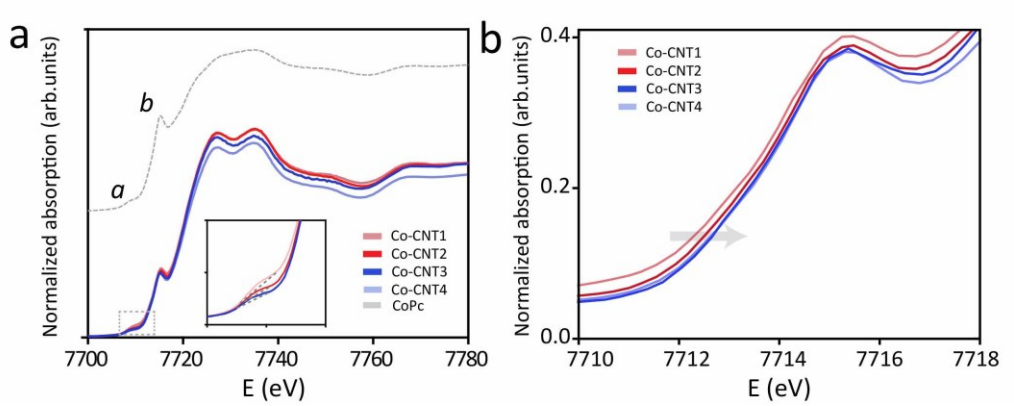

Figure 6.4 (a) Co k-edge XANES spectra and (b) enlarged Co k-edge XANES spectra at the near edge region of CoPc and CoPc-CNTx.

As shown in Figure 6.4a, the weaker pre-edge peak (peak *a*) at ca. 7709 eV is assigned to the dipole forbidden 1s → 3d transitions which reflect the hybridization of the empty 3d metal states, the amplitude of which increases with the decrease in symmetry in CoN4.[176] Co-CNT1 exhibits the strongest peak intensity (insert), thus affording the most severe metal site distortion from centrosymmetric to non-centrosymmetric coordination environment.[177,178] The gradual decrease in peak intensity from Co-CNT2 to Co-CNT3 and Co-CNT4 indicates the continuous reduction in the degree of distortions. As further demonstrated in Figure 6.4b, the second pre-edge peak (peak *b*) in XANES emerged at ca. 7715 eV represents the electric dipole transition of 1s → $4p_z$, a fingerprint feature that probes the square-planar bonding motif of CoN4 with D_{4h} symmetry in CoPc molecules. The intensity of this peak is the strongest in Co-CNT1 and attenuates in the other samples. This is a sign of the presence of symmetry-breaking and deformed CoN4 geometry,

alongside the changes in the π-electron conjugation in molecularly dispersed CoPc, which are presumably triggered by the different magnitude of strain within CoPc. In addition to these features, the valence states of Co can be extrapolated from the adsorption edge energy of XANES spectrum, which is determined by finding the energy shifts in adsorption edge. The adsorption edges slightly shift rightward as the CNT radius increases from Co-CN1 to Co-CNT2. This variation, albeit subtle, indicates more localized electrons around the Co centers as the CNTs radius decreases, thus lowering oxidation states of Co ions. The Co-CNT3 and Co-CNT4 take on similar values, suggesting the similar oxidation states in these two samples. These observations agree well with the previous reports on the Zn-N4 geometries and Zn K-edge XAS studies, which suggests a correlation between Zn-N4 bond length and valence states of Zn.[170] The high-resolution Co 2p XPS spectra possess similar profiles (Figure 6.5), indicating the prevailing +2 oxidation states of Co ions. However, insignificant peak shifts have been detected by XPS, this is probably due to the different sensitivities of XPS and XAS techniques.

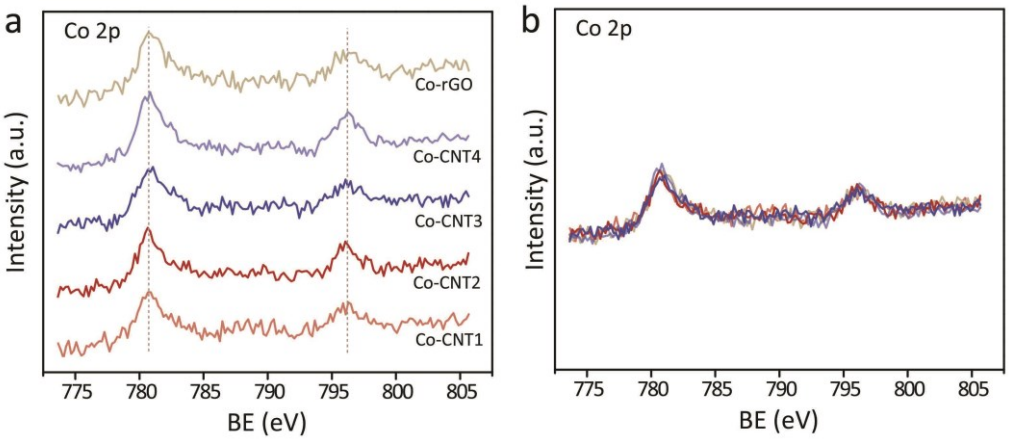

Figure 6.5 XPS high resolution Co 2p spectra of Co-CNTx and Co-rGO.

The Co K-edge κ3 weighted FT-EXAFS, which directly reflect the distances between Co center and adjacent atoms, are presented to support the hypothesis on the strained CoN8C8 motifs in Co-CNTx (Figure 6.6a). The FT-EXAFS spectrum of bare CoPc exhibits one major peak at ca. 1.44 Å, assigned to the Co-N_{1st} scattering path in CoPc. The position of this primary peak gradually shifts leftward as the radius of CNTs decreases. These are clear indications of the Co-N_{1st} distance decrease and bond shrinkage. In addition to the decreased Co-N_{1st} bond lengths, similar trend is also observed over the Co-C_{2nd} and Co-N_{3rd} shell.[176,179,180] This suggests that the overall CoPc molecular is subjected to certain degree of compression when hybridized with CNT, leading to the more compact molecules with altered bond length. The bond distance reduction when coupled with highly curved substrates has been identified in another recent study.[181] The magnitude of deformation within the CoN8C8 can be interpreted with shearing and/or linear strain induced by the changes in bond angle and/or bond length. Probing the bond distance in CoPc is more straightforward and experimentally feasible compared to bond angel and thus, the magnitude of linear strain is adopted as a descriptor and calculated based on the R values of all three shells: $\varepsilon = (\Delta R)/R_{zero}$, where ΔR stands for the difference in final (strained) and equilibrium (R_{zero}) bond distance, respectively. The R value measured from Co-CNT4 was adopted as the equilibrium/initial distance, considering that the radius of CNT4 is large enough to afford a near-planar surface and thus, the ε around Co center in Co-CNT4 is set as a reference point and equals to zero (Co-rGO is ruled out for comparison, as will be discussed in the following section). Based on the above rationale, the magnitude of $\bar{\varepsilon}$ around Co is semi-quantitatively determined based on the value of bond distance change averaged from three different shells adopted from the XAFS results (Figure 6.6b). To briefly sum up, the magnitude of strain within

CoPc molecules changes as a function of the radius of the CNT. Co-CNT1 and Co-CNT2 are categorized as group 1, where these geometric effects are more prominent. Co-CNT3 and Co-CNT4 possess similar geometric properties and are categorized as group 2.

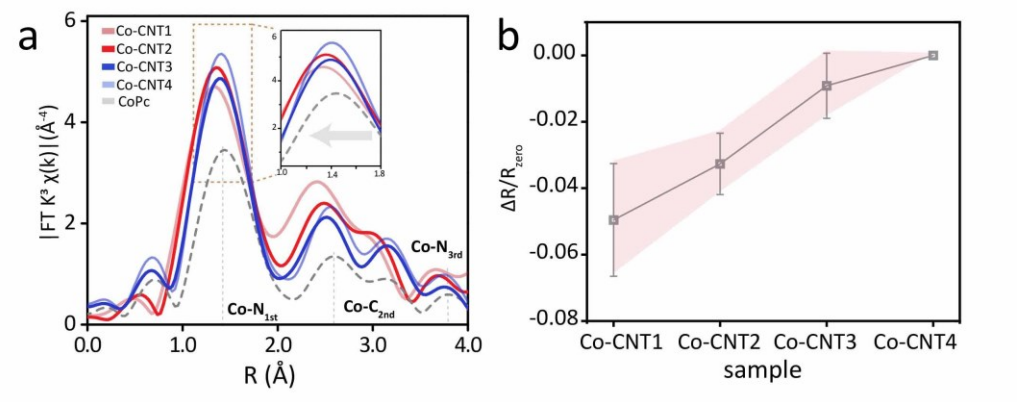

Figure 6.6 (a) Fourier transformed κ3-weight EXAFS spectra of CoPc and CoPc-CNTx. (b) Magnitude of the average bond distance change with respect to the equilibrated bond distance in CoPc-CNTx.

The LSV was collected in CO_2 saturated 0.5 M $KHCO_3$ to pre-examine the area-specific catalytic capabilities toward CO_2RR and HER over different samples. As shown in Figure 6.7a, Co-CNT1 demonstrates the highest overall activity, followed by Co-CNT2. Co-CNT3 and Co-CNT4 show similar LSV results, both are lower than Co-CNT1 and Co-NT2. Co-rGO delivers the lowest $j_{total\text{-}geo}$. Chronoamperometric CO_2 electrolysis covering a range of cathodic potentials (-0.5 - -1.05 V) was performed. Potentials beyond -1.05 V progressively erode the catalysts, which rises severe stability issues, when it is below -0.5 V the current density is too low and may lead to significant errors. Therefore, -0.5 - -1.05 V is an appropriate range for CO_2RR studies. In details, Co-CNT2 delivers optimal Faradic Efficiency toward CO among all samples, particularly at more cathodic potentials from - 0.95 to - 1.05 V. Co-CNT3 also demonstrates good FEco, but it only delivers

comparable FEco to Co-CNT2 within a narrower potential range (-0.6 - -0.9 V). Mass transfer limitations due to different specific surface areas/porosities of carbon support cannot sufficiently explain the observed FEco differences at -0.9 - -1.05 V, as Co-CNT1 possesses the smallest radius which would otherwise delivers the highest FEco. Co-CNT4, Co-rGO and CoPc display inferior FEco compared to Co-CNT2 at all the measured potentials.

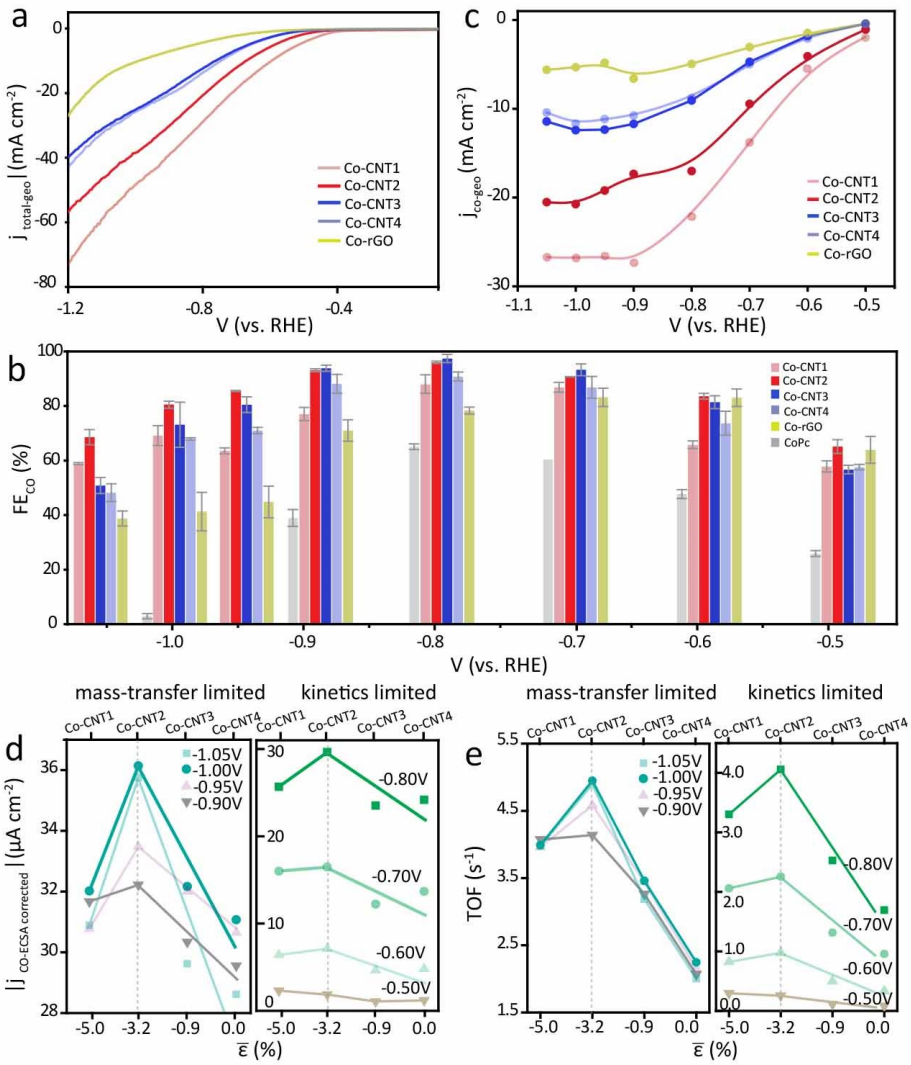

Figure 6.7 (a) LSV obtained in Co-CNTx and Co-rGO. (b) FEco of Co-CNTx, Co-rGO and CoPc averaged from three independent measurements. (c) $j_{co\text{-}geo}$ of Co-CNTx and Co-rGO. (d) $j_{co\text{-}ECSA}$ - $\bar{\varepsilon}$ plot, and (e) TOF - $\bar{\varepsilon}$ plot over measured potential range.

As shown in Figure 6.7c, Co-CNT1 shows the highest $j_{co\text{-}geo}$, followed by Co-CNT2. Co-CNT3 and Co-CNT4 demonstrate comparable $j_{co\text{-}geo}$ while Co-rGO shows the smallest $j_{co\text{-}geo}$. Note that ideally, Co-rGO is suitable to study the geometry-induced effects owing to the planar surface of rGO,[182] however, the apex FEco in Co-rGO emerges at ca. - 0.6 - - 0.7 V, slightly deviates from the - 0.8 V observed in the Co-CNTx series. This may be presumably explained by the different electron transfer patterns within CNT/rGO supported catalysts, as further evidenced by the EIS **(Figure 6.8,** Table S2). The fitted results show that all the samples possess similar Rs values (which reflect the resistance of electrolyte), but different Rp values with Co-rGO (99.47 Ω cm^2) being considerably larger than the others. As the charge transfer strongly affects the reaction kinetics on the catalyst's surface,[183,184] the Co-rGO will be ruled out to ensure fair comparisons of the electrocatalysts' performances. It is noted that Co-CNTx samples also show different Rp, which increases monotonically as the radius of CNTs increases, similar to the trends observed in $j_{total\text{-}geo}$ and $j_{co\text{-}geo}$.

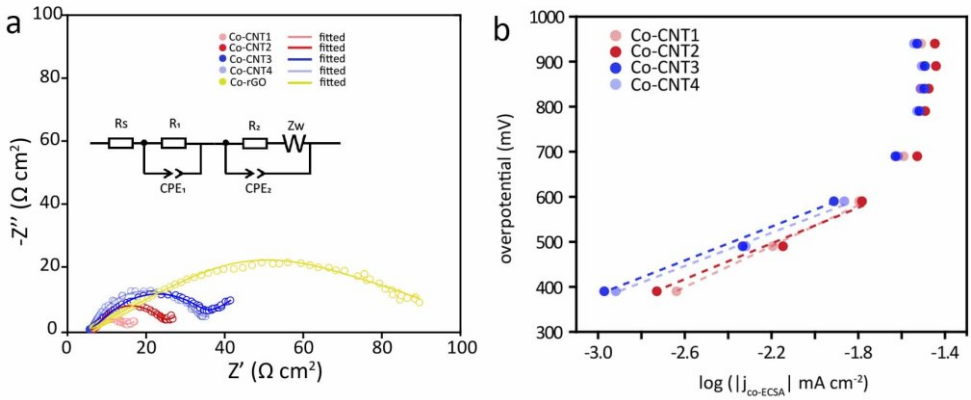

Figure 6.8 (a) EIS of Co-CNTx and Co-rGO. (b) Tafel slope of Co-CNTx.

In addition to the measurements of $j_{total\text{-}geo}$, $j_{co\text{-}geo}$ and FE_{co}, the intrinsic activities remain as the most important metrics attesting the performances of the electrocatalysts. The activities were firstly determined by calculating the $j_{co\text{-}ECSA}$, which is more pertinent to our goal.[185,186] As shown in Figure 6.7d, the $j_{co\text{-}ECSA}$ as a function of the $\bar{\varepsilon}$ was plotted to unveil the activity-strain relation. A volcano-type relation can be clearly observed between the magnitude of $\bar{\varepsilon}$ and the values of $j_{co\text{-}ECSA}$. At the representative potential of - 0.8 V where the mass transfer limitations can be generally neglected, the $j_{co\text{-}ECSA}$ in Co-CNT2 is approximately 1.22-fold improvement compared to that in the Co-CNT4 at the same voltage. To further assess the TOF as a function of deformation, the values of TOF were calculated based on the total mass of Co atoms. Using the total mass of Co for TOF calculations generally gives its lower bound values, but it is reasonable in this study due to the high-level molecular dispersion and excellent exposure of CoPc.[187] As shown in Figure 6.7e, the volcanic relation has also been spotted in the TOF-strain plot where Co-CNT2 shows the maximum TOF value at all the measured potentials. Moreover, such a relation is more prominent in the kinetically limited region (-0.5 - -0.8 V). For instance, at - 0.8 V, Co-CNT2 shows a TOF of 4.1 s^{-1}, which is 2.4-fold (1.7 s^{-1}), 1.6-fold (2.5 s^{-1}) and 1.2-fold (3.3 s^{-1}) enhancement compared to Co-CNT4, Co-CNT3 and Co-CNT1, respectively, corroborating the highest intrinsic activities of Co atoms in the Co-CNT2 samples. To probe the reaction kinetics of CO formation, Tafel analysis derived from the $j_{co\text{-}ECSA}$ and overpotentials ($E^0(CO_2/CO)$ = -0.11 V vs RHE, pH 7.3) is presented in Figure 6.8b. Co-CNT2 shows the smallest Tafel slope of 118 mV dec^{-1} among Co-CNT1 (139 mV dec^{-1}) and Co-CNT4 (155 mV dec^{-1}), comparable to Co-CNT3 (119 mV dec^{-1}), indicating the same RDS of CO_2 activation and concurrent electron transfer step in all Co-CNTx. The Tafel values are close to the theoretical value of 118 mV dec^{-1}, further verifying the highly molecular distributions

of CoPc with negligible mass transfer limitations, which is the premise to study the geometric effect on CO_2RR.

To provide mechanistic insights to the experimental observations, we seek to model the process using DFT-based methods. Studying the real systems (where the radii of the CNT could be up to ca. 20 nm) is quite challenging, therefore, we seek to mimic the various deformed CoN8C8 structures with a series of simplified models (Figure 6.9a), where the pyrrolic-type CoN8C8 motifs are embedded in graphene, and then regulating bond length by applying certain amount of "compressive strain" (i.e., -1%, -2%, -3%, -4%, -5%, -6%) and "tensile strain" (i.e., +1% and +2%). In these models, we could achieve: 1) fine regulation of the inter-atomic distance, which is the major observation in our previous discussion, and 2) perseverance of the whole basic CoN8C8 motif, including the characteristic isoindole nitrogen (N_i) and *meso*-nitrogen (N_m) sites. Thus, the calculations should provide useful insights into the local geometric effects on CO_2RR. As shown in Figure 6.9b, all models share the same RDS which is the protonation of CO_2 to form *COOH, but with different energy penalty associated with the RDS. When the ε changes stepwise from 0% to -3%, the energy barrier reduces correspondingly, suggesting that the CO_2RR has become easier to occur as the bond length decreases. For models with $-4\% < \varepsilon < -6\%$, the strain effects are less prominent toward Gibbs free energy change, as manifested by the similar energy barriers of each individual step. The RDS results are also in line with Tafel results, suggesting that the barrier energy associated with the RDS step can be readily tuned by applying compression, thus enabling higher activity and catalytic turnover.

To gain further insight into the long-term performances of Co-CNTx, the stability tests at the cathodic potential of -0.95 V were conducted over a time span of 4 hours to initially probe the degradation patterns. The samples are donated as Co-CNTx-4h. The expedited degradation of MNxCy-rich catalysts has been reported to occur at more negative potentials, e.g., -0.9 V [188] and -1.0V [189]; this allows the easier observations of the degradation patterns within reasonable timescale.

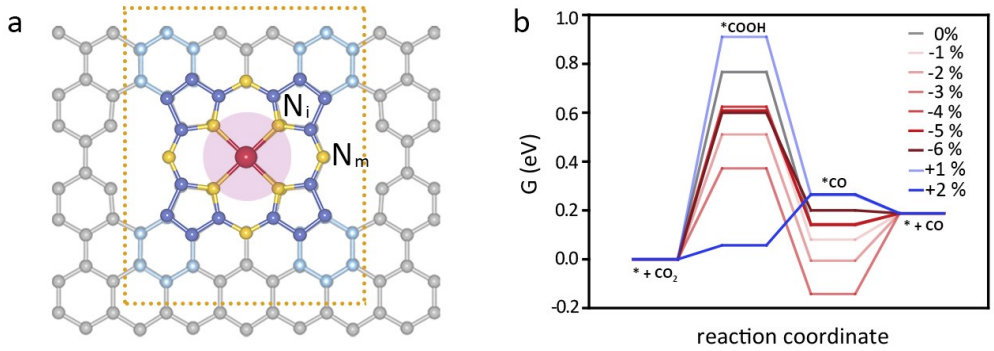

Figure 6.9 (a) Simplified models with CoN8C8 embedded in graphene. (b) Gibbs free energy change of CO_2-to-CO calculated based on simplified models with different degree of compression or tension.

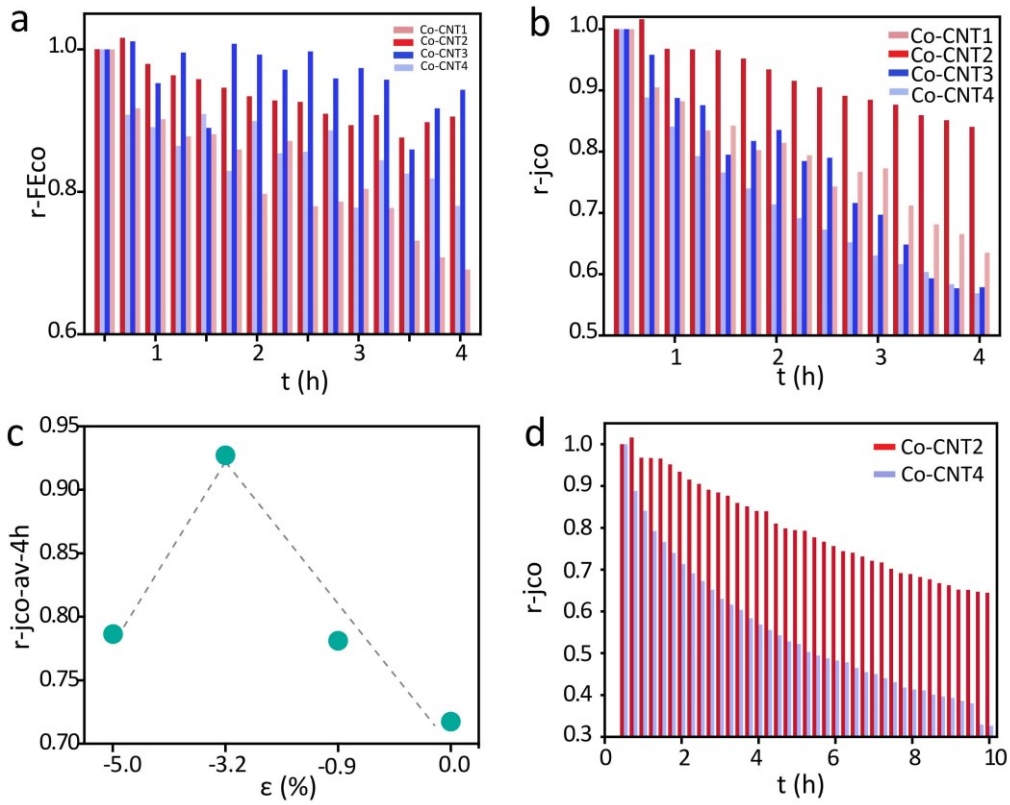

Figure 6.10 (a) r-FEco and (b) r-jco of Co-CNTx measured at -0.95 V in the initial four hours. (c) The r-jco-av-4h with respect to the magnitude of deformation. (d) r-jco of Co-CNT2 and Co-CNT4 over the course of 10 h electrolysis.

As shown in Figure 6.10a, the FEco values were monitored and normalized with respect to their stable values acquired at 0.5 h, defined as the FEco retention (r-FEco). The r-FEco continuously decreases in all samples over time, while Co-CNT2 and Co-CNT3 retain the r-FEco above 90%. The discrepancies in the CO degrading profiles are further strengthened by comparing the retention of jco (denoted as r-jco, taking the jco at 0.5 h as the initial value) during electrolysis, which could more accurately reflect the changes in activity (Figure 6.10b). Co-CNT2 shows the highest r-jco, following the Co-CNT1, while Co-CNT3 and Co-CNT4 possess similar r-jco. A volcanic feature can be extrapolated based on the average r-jco (r-jco-av-4h, Figure 6.10c). We mapped the

degradation profiles of Co-CNT2 and Co-CNT4, the two catalysts with the highest and lowest r-jco, respectively, by extending the reaction time to 10h (denoted as Co-CNTx-10h). As shown in Figure 6.10d, the Co-CNT2 degrades at a rather homogeneous and mild rate while the Co-CNT4 demonstrates a more aggressive degradation profile over the course of CO_2RR. The rate of degradation, *r*, calculated based on the slope of Figure 3c takes on the values of 3.6% and 6.7% h^{-1} in Co-CNT2 and Co-CNT4, respectively, pointing to a nearly doubled degradation rate in Co-CNT4.

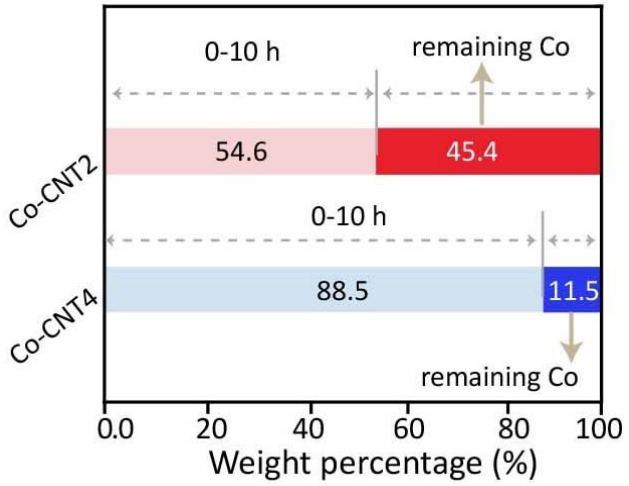

Figure 6.11 Co centration in the electrolyte of Co-CNT2-10h and Co-CNT4-10h.

An assortment of degradation mechanisms are intertwined and collectively contribute to the overall performance decay in catalysts with monomerically distributed active centers.[190–192] ICP-OES reveals that the Co-CNT2-10 and Co-CNT4-10 have the Co leaching rates of 7e-5 and 1.4e-4 mg h^{-1}, respectively, corresponding to the overall Co mass losses of 54.6% and 88.5% (Figure 6.11). One route for the Co leaching is the "direct" Co release from the macrocycle core,[190] which leaves behind the base-free H_2Pc matrix. As shown in Figure 6.12, the SERS of Co-CNT2-10h and Co-CNT4-10h can hardly be indexed into the H_2Pc spectrum colored in grey and yet, a few newly

emerged peaks (blue dots) at 1600, 1030, 998, 850 and 800 cm^{-1} closely pertain to the C-C stretching, ring breathing and deformation in benzene-related vibrations.[193,194] This strongly supports the "indirect" leaching pathway, which is likely promoted by the irreversible electricity-driven fragmentation of the CoPc and the simultaneous generation of benzene-based units.[77] In addition, the CoPc and benzene-related vibrations coexist in Co-CNT2-10h, whereas in Co-CNT4-10h, no CoPc has been detected because the majority of CoPc has eroded and the amount of remaining CoPc fallen below the SERS detection limit. Metallic Co formation can be ruled by XAFS and TEM (Figure S6.1).[17,173] Physical detachment is unlikely the major cause differentiating the *r* values based on the analysis of the reaction rates and binding energy.[72,173] Therefore, the various CoPc fragmentation rates in these samples are the major contributor to the different decay rates.

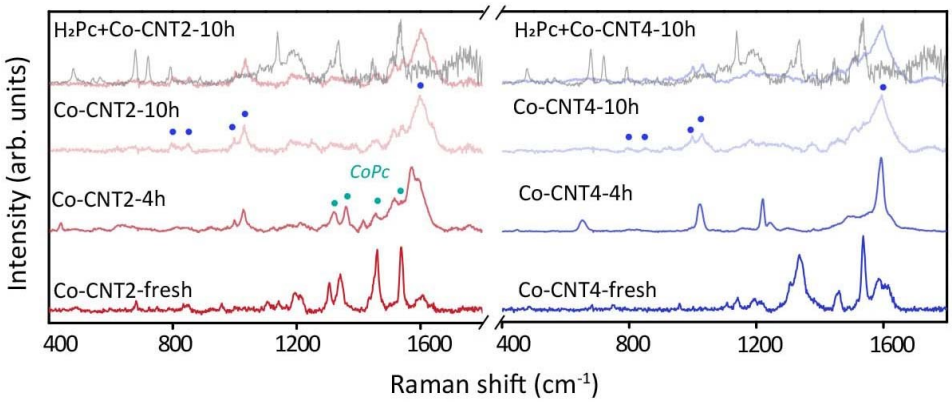

Figure 6.12 SERS spectra of Co-CNT2 and Co-CNT4 before, and after degradation studies of 4h and 10h.

While the origin of CoPc fragmentation under cathodic potentials is still open for discussion, we tentatively discuss the possible reasons leading to different CoPc demetallation rates when coupled with different CNTs. The emergence of the benzene-related signals in SERS alongside ICP-OES results collectively suggest that certain bonds have dissociated and yielded the free-

standing benzene-related pieces and Co ions. The possible pathways of CoPc fragmentation reported previously point to the protonation of the N_i and/or N_m atoms, further leading to weakened Co-N_i, C-N_i and/or C-N_m bond strength.[195,196] The absence of H_2Pc vibrations in SERS rules out the sole rapture of Co-N_i. The protonation attack at N_m and scission of C-N_m bonds are more probably based on the SERS results and DFT calculations.[195] Hence, Bader charge analysis was performed to examine the charge transfer between C-N_m bonds in two model catalysts with either planar or curved CoPc geometries. On average, the N_m atoms gain 0.80 and 0.86 |e| in flat and curved samples, respectively, suggesting that the charge transfer from C to N_m in the strained samples is indeed more favorable due to its stronger C-N_m interactions. In addition, the overall charge transfer capabilities in Co-CNTx could also affect stability (see EIS results). Given the same number of total electrons, Co-CNT2 is inclined to allocate a relatively larger portion of electrons to reduce CO_2, owing to its more efficient charge transfer and higher intrinsic activities. As a result, fewer electrons will be utilized to drive the detrimental self-corrosion process. Therefore, we postulate that the more compact CoPc structure and efficient charge transfer endowed by the local deformation helps improve the stability of catalysts during electrolysis. More investigations will be needed to fully uncover the degradation mechanisms of the CoPc-CNTx systems.

6.3. Conclusions

This study reports the enhanced intrinsic activity and stability of CoPc-CNT hybrids with the curvature-induced compressively distorted CoN8C8 moiety in the application of CO_2RR. The conclusions made based on the results from this study are threefolds: Firstly, CNTx with various radii can induce different magnitude of curvature/deformation/bond length reduction in CoPc, which can be readily interpreted as the intramolecular strain within the CoC8N8 motif, and such

strain effects are more prominent when the radius of CNT is below 4 nm. Secondly, the optimal magnitude of strain could boost the intrinsic activity of the Co centers in terms of CO_2-to-CO conversion, displaying the volcanic feature in the activity-strain relations. Thirdly, optimal strain is one of the parameters contributing to the stabilization the overall CoPc structures against demetallation during CO_2RR.

6.4. Supporting information

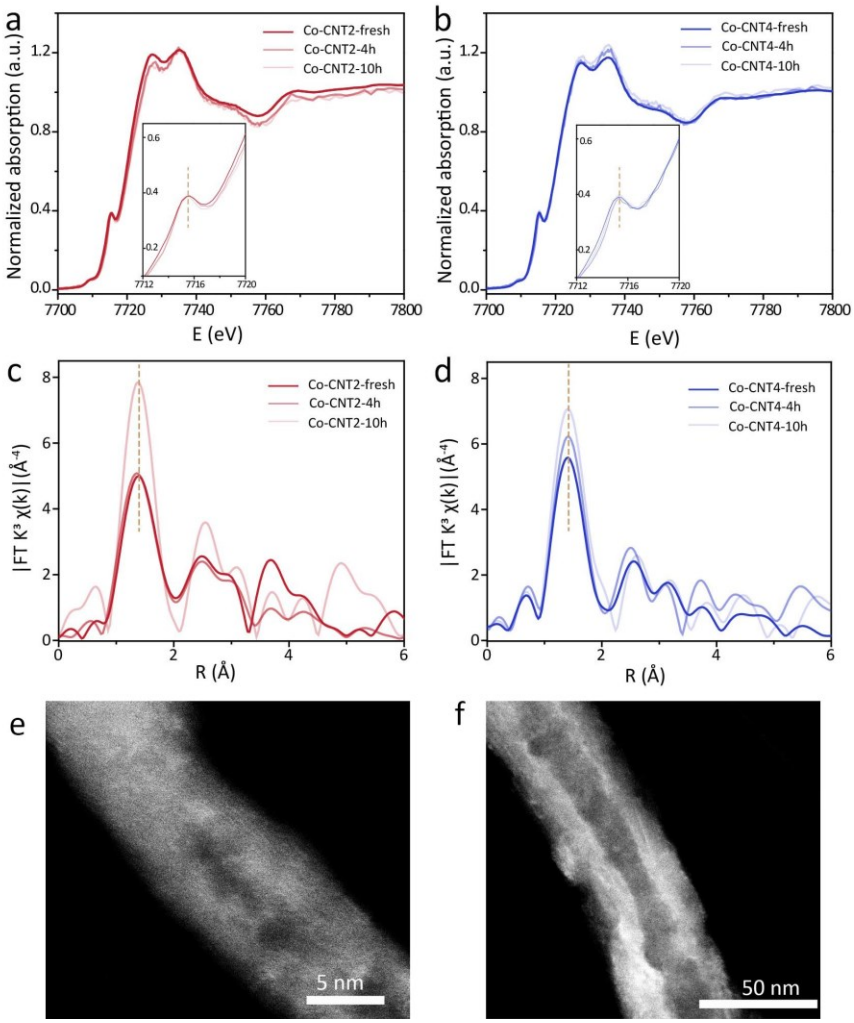

Figure S6.1 (a-d) Ex situ XAFS (a-b) and EXAFS (c-d) of Co-CNT2-4h, Co-CNT2-10h, Co-CNT4-4h, Co-CNT4-10h. (e, f) of STEM images of Co-CNT2-10h and Co-CNT4-10h.

Table S6.1 Co concentrations in Co-CNTx and obtained by ICP-OES analysis.

Sample	Co (mg L^{-1})
Co-CNT1	0.514
Co-CNT2	0.322
Co-CNT3	0.276
Co-CNT4	0.398

Table S6.2 Fitted Rs and Rp values in Co-CNTx and Co-rGO.

Sample	Rs	Rp
Co-CNT1	5.92	12.88
Co-CNT2	6.11	20.32
Co-CNT3	4.81	22.46
Co-CNT4	6.65	28.66
Co-rGO	5.81	99.47

Chapter 7. Summary and Future Prospects

7.1. Summary

The work in this dissertation focused on the development of innovative electrocatalysts and the investigations of their structure-performance correlations. Bismuth-based materials have attracted significant research interest as efficient catalysts for producing value-added chemicals, primarily FA and CO, from CO_2. However, their scalability and industrialization have been hindered by complex production procedures and low product yields. To tackle these challenges, a perovskite-type catalyst, BBO, has been synthesized using a facile sol-gel approach and identified as a suitable candidate for CO_2RR. Through a combination of XRD, SEM, TEM and XPS techniques, the dynamic evolution of BBO under applied potentials was revealed, leading to the formation of Bi nanosheets (eBBO) alongside the release of A-site element (Ba) during electrolysis, both of which accounted for the phase transition from BBO to metallic Bi with layered structures (eBBO/Bi nanosheets). Another advantage of BBO is the ability to release Ba^{2+} naturally. The FA production can be significantly boosted in the Ba^{2+}-contained electrolyte, particularly at low cathodic potentials. Time-resolved FTIR and *in situ* Raman analysis reveal that the Ba^{2+} benefits the CO_2 adsorption, which ultimately contributes to the improved CO_2-to-FA conversion.

To further enhance atom turnover efficacy, mass-specific activity, and reduce the production cost, downsizing the catalysts from nano- to atomic-scale to expose more active sites has been identified as a viable approach. This strategy involves exposing more active sites to promote better interaction between active sites and reactants. However, at the atomic dimension, the performance of the catalysts becomes extremely sensitive to the local environment, where any

subtle variations could lead to a paradigm-shift in the CO_2RR performances due to the modifications of the electronic structure of the active species. Using supported Bi as model catalysts, the coordination-tuned CO_2RR has been comprehensively investigated by tailoring the type of the "glue atoms" (C and N) to Bi center. Through DFT calculations, the mechanistic bifurcation routes have been identified over Bi SAs, which selectively produces either FA or syngas when bound to C or N atoms, respectively. Theoretical analysis suggests that the tunable selectivity arises from the different coupling states and metal-supported interactions between the central Bi atom and adjacent atoms, which modify the hybridizations between the Bi center and *OCHO/*COOH intermediates, alter the energy barriers of the rate-determining steps and ultimately trigger branched reaction pathways after CO_2 adsorption. A novel ultrafast laser shock method was developed to achieve the immobilization of Bi SAs with tunable ligand atoms. Particularly, Bi-C with carbon atoms as the ligand atoms tend to produce the FA from CO_2RR with negligible account of CO detected, and Bi-NC with nitrogen atoms as the ligand atoms can drive the CO production at small over potentials and achieve the maximal CO selectivity at a low cathodic potential of - 0.5 V. There are two important implications of this work. First, an annealing-free method was developed to fabricate the SACs within short periods of time. This strategy can be broadly applied to prepared SACs electrocatalysts with different types of metal atoms that are tailorable to various electrochemical process. Second, the mechanistic insights of the aqueous-based CO_2RR performances on the surface of p-blocking Bi SAs were provided, and a general classification of p-blocking SACs were proposed based on the selectivity toward CO_2RR.

In the case of Bi-C and Bi-NC, it has been assumed that these SACs would adopt ideal geometric structures with equal bond length angle. However, in practical scenarios, local deformations

around the central active atoms in SACs often occur due to the presence of different ligand atoms. The net effects of geometric variations have largely been overlooked due to the challenges in disentangling geometric effects from other factors. Additionally, there is a lack of synthesis methods that can effectively regulation the geometries, and advanced techniques are also needed to probe the local deformations. To address the challenges, a series of CoPc-CNTs are chosen as ideal platforms in this study to introduce deformation around central Co atoms, and the magnitude is controlled by varying the radii/curvatures of the CNTs matrix. With this model electrocatalyst, we applied systematic and comprehensive physical and electrochemical characterizations in conjunction with DFT simulations to fully uncover their strain-function relations. A typical volcano trend over the intrinsic CO_2RR activities and the magnitude of strain around Co centres based on interatomic distance has been established, where the apex point is a mildly compressed CoN8C8 with reduced Co-N/C bond lengths. This study highlights and confirms the importance of controlling the geometric distortion of catalysts in the applications of CO_2RR, which demonstrates the untapped potentials of strain engineering in MNxCy-based structures to realize further achievements in CO_2RR.

7.2. Future Prospects

Multiple future directions can be proposed for the room-temperature CO_2RR research, which possess the potential to enhance our comprehension of the operational mechanisms of CO_2RR in practical systems and expedite the lab-to-fab transfer of CO_2RR methodology and ultimately achieve global carbon neutrality.

7.2.1. Operando CO_2RR study

Operando study provides value insights into both the mechanisms of CO_2RR and the ever-evolving dynamics of electrocatalysts in practical scenarios. On one hand, future research could focus on examining the *in situ* physiochemical features of catalyst to uncover the connections between CO_2RR activity and materials properties, as this knowledge is essential for the rational design of electrocatalysts to reach the desired performance. On the other hand, efforts should be exerted into investigating the reaction pathways, particularly the C_{2+} products, which remain elusive nowadays.

7.2.2. Stability study

The unsatisfactory long-term stability (>1000 h) of electrocatalysts in the context of CO_2RR has significantly impeded the practical implementation of this technique. The degradation of materials represents a critical concern for the industry, which has been unfortunately overlooked for some time. In contrast to the well-established electrocatalysts employed in other chemical synthesis reactions, those utilized in CO_2RR are comparatively less understood with regard to their degradation mechanisms.

7.2.3. Materials development based on artificial intelligence

The conventional trial-and-error approach to developing well-performing electrocatalysts toward a target reaction is considerably inefficient and time-consuming. The exploration of novel, unknown and untested materials could be greatly expedited through the implementation of big data analysis, drawing from the vast data pool of theoretical simulation results, and established experiential data in the literature. The integration of artificial intelligence into materials design represents a new epoch in the advancement of next-generation electrocatalysts for CO_2RR.

7.2.4. New electrolyser configurations

To enable large-scale operation of CO_2RR, electrolysers must be meticulously designed to surmount the challenges of low CO_2 solubility and sluggish CO_2 mass transfer in liquid-based electrolytes. While the implementation of a flow cell configuration does partially address these issues, other hindrances such as flooding, and carbonate depositions require careful considerations. Hence, substantial progress in the design of electrolysers is vital to propel the study of CO_2RR going forward.

Bibliography

(1) US Department of Commerce, Global Monitoring Laboratory, Carbon Cycle Greenhouse Gases, Trends in Atmospheric Carbon Dioxide, website, https://gml.noaa.gov/ccgg/trends/gl_gr.html.

(2) Government of Canada (2023-01-27), Net-Zero Emissions by 2050, website, https://www.canada.ca/en/services/environment/weather/climatechange/climate-plan/net-zero-emissions-2050.html.

(3) Masel, R. I.; Liu, Z.; Yang, H.; Kaczur, J. J.; Carrillo, D.; Ren, S.; Salvatore, D.; Berlinguette, C. P. An Industrial Perspective on Catalysts for Low-Temperature CO_2 Electrolysis. *Nat. Nanotechnol.* **2021**, *16*, 118–128.

(4) Bushuyev, O. S.; De Luna, P.; Dinh, C. T.; Tao, L.; Saur, G.; Van De Lagemaat, J.; Kelley, S. O.; Sargent, E. H. What Should We Make with CO_2 and How Can We Make It? *Joule* **2018**, *2*, 825–832.

(5) Shin, H.; Hansen, K. U.; Jiao, F. Techno-Economic Assessment of Low-Temperature Carbon Dioxide Electrolysis. *Nat. Sustain.* **2021**, *4* (10), 911–919.

(6) Joaquin, R.; Bell, A. T. Electrocatalytic CO_2 Reduction to Fuels: Progress and Opportunities. *Trends Chem.* **2020**, *2* (9), 825–836.

(7) Aresta, M. Carbon Dioxide as Chemical Feedstock. Germany, WILEY-VCH Verlag GmbH & Co. KGaA, Weinheim, **2010**, ISBN: 978-3-527-32475-0.

(8) Nitish, G.; Gerog, K.; Heenen, H. H.; Karen, C. Improving the Intrinsic Activity of Electrocatalysts for Sustainable Energy Conversion: Where Are We and Where Can We Go? *Chem. Sci.* **2022**, *13*, 14–26.

(9) Clark, E. L.; Resasco, J.; Landers, A.; Lin, J.; Chung, L.-T.; Walton, A.; Hahn, C.; Jaramillo, T. F.; Bell, A. T. Standards and Protocols for Data Acquisition and Reporting for Studies of the Electrochemical Reduction of Carbon Dioxide. *ACS Catal.* **2018**, *8*, 6560–6570.

(10) Van Daele, K.; De Mot, B.; Pupo, M.; Daems, N.; Pant, D.; Kortlever, R.; Breugelmans, T. Sn-Based Electrocatalyst Stability: A Crucial Piece to the Puzzle for the Electrochemical CO_2 Reduction toward Formic Acid. *ACS Energy Lett.* **2021**, *6*, 4317–4327.

(11) Popović, S.; Smiljanić, M.; Jovanovič, P.; Vavra, J.; Buonsanti, R.; Hodnik, N. Stability and Degradation Mechanisms of Copper-Based Catalysts for Electrochemical CO_2 Reduction. *Angew. Chem. Int. Ed.* **2020**, *132* (35), 14844–14854.

(12) Nitopi, S.; Bertheussen, E.; Scott, S. B.; Liu, X.; Engstfeld, A. K.; Horch, S.; Seger, B.; Stephens, I. E. L.; Chan, K.; Hahn, C.; Nørskov, J. K.; Jaramillo, T. F.; Chorkendorff, I. Progress and Perspectives of Electrochemical CO_2 Reduction on Copper in Aqueous Electrolyte. *Chem. Rev.* **2019**, *119*, 7610–7672.

(13) Kortlever, R.; Shen, J.; Jan Schouten, K. P.; Calle-Vallejo, F.; M Koper, M. T. Catalysts and Reaction Pathways for the Electrochemical Reduction of Carbon Dioxide. *J. Phys. Chem. Lett.* **2015**, *6*, 4073–4082.

(14) Chernyshova, I. V; Somasundaran, P.; Ponnurangam, S. On the Origin of the Elusive First Intermediate of CO_2 Electroreduction. *Proc. Natl. Acad. Sci. U.S.A.* **2018**, *115*, E9261–E9270.

(15) Andrew A. Peterson, Frank Abild-Pedersen, Felix Studt, J. R. and J. K. N. How Copper Catalyzes the Electroreduction of Carbon Dioxide into Hydrocarbon Fuels. *Energy Environ. Sci.* **2010**, *3*, 1311–1315.

(16) Kuhl, K. P.; Toru, H.; Cave, E. R.; Abram, D. N.; Kibsgaard, J.; Jaramillo, T. F. Electrocatalytic Conversion of Carbon Dioxide to Methane and Methanol on Transition Metal Surfaces. *J. Am. Chem. Soc.* **2014**, *136*, 14107–14113.

(17) Chen, X.; Hu, X.-M.; Daasbjerg, K.; Ahlquist, M. S. G. Understanding the Enhanced Catalytic CO_2 Reduction upon Adhering Cobalt Porphyrin to Carbon Nanotubes and the Inverse Loading Effect. *Organometallics* **2020**, *39*, 1634–1641.

(18) Feaster, J. T.; Shi, C.; Cave, E. R.; Hatsukade, T.; Abram, D. N.; Kuhl, K. P.; Hahn, C.; Nørskov, J. K.; Jaramillo, T. F. Understanding Selectivity for the Electrochemical Reduction of Carbon Dioxide to Formic Acid and Carbon Monoxide on Metal Electrodes. *ACS Catal.* **2017**, *7*, 4822−4827.

(19) Nie, X.; Luo, W.; Janik, M. J.; Asthagiri, A.; Lowrie, W. G. Reaction Mechanisms of CO_2 Electrochemical Reduction on Cu(111) Determined with Density Functional Theory. *J. Catal.* **2014**, *312*, 108–122.

(20) Peterson, A. A.; Abild-Pedersen, F.; Studt, F.; Rossmeisl, J.; Nørskov, J. K. How Copper

Catalyzes the Electroreduction of Carbon Dioxide into Hydrocarbon Fuels. *Energy Environ. Sci.* **2010**, *3* (9), 1311–1315.

(21) Nie, X.; Esopi, M. R.; Janik, M. J.; Asthagiri, A. Selectivity of CO_2 Reduction on Copper Electrodes: The Role of the Kinetics of Elementary Steps. *Angew. Chem. Int. Ed.* **2013**, *52* (9), 2459–2462.

(22) Hammer, B.; Nørskov, J. K. Advances in Catalysis, Academic Press, volume 45, **2000**, ISBN: 978-0-12-007845-5.

(23) Vayenas, C.G.; White, R.E.; Gamboa-Aldeco, M.E. Modern Aspects of Electrochemistry no.42, Springer, **2008**, ISBN: 978-0-387-49488-3

(24) Senocrate, A.; Battaglia, C. Electrochemical CO_2 Reduction at Room Temperature: Status and Perspectives. *J. Energy Storage* **2021**, *36*, 102373.

(25) Yang, Q.; Wu, Q.; Liu, Y.; Luo, S.; Wu, X.; Zhao, X.; Zou, H.; Long, B.; Chen, W.; Liao, Y.; Li, L.; Shen, P. K.; Duan, L.; Quan, Z. Novel Bi-Doped Amorphous SnOx Nanoshells for Efficient Electrochemical CO_2 Reduction into Formate at Low Overpotentials. *Adv. Mater.* **2020**, *2002822*, 1–7.

(26) Xing, Y.; Kong, X.; Guo, X.; Liu, Y.; Li, Q.; Zhang, Y.; Sheng, Y.; Yang, X.; Geng, Z.; Zeng, J. Bi@Sn Core–Shell Structure Witasts the Electroreduction of CO_2 into Formic Acid. *Adv. Sci.* **2020**, 1902989.

(27) Zhong, M.; Tran, K.; Min, Y.; Wang, C.; Wang, Z.; Dinh, C.-T.; De Luna, P.; Yu, Z.; Rasouli, A. S.; Brodersen, P.; Sun, S.; Voznyy, O.; Tan, C.-S.; Askerka, M.; Che, F.; Liu, M.; Seifitokaldani, A.; Pang, Y.; Lo, S.-C.; Ip, A.; Ulissi, Z.; Sargent, E. H. Accelerated Discovery of CO_2 Electrocatalysts Using Active Machine Learning. *Nature* **2020**, *581* (7807), 178–183.

(28) Lum, Y.; Ager, J. W. Sequential Catalysis Controls Selectivity in Electrochemical CO_2 Reduction on Cu. *Energy Environ. Sci.* **2018**, *11* (10), 2935–2944.

(29) Morales-Guio, C. G.; Cave, E. R.; Nitopi, S. A.; Feaster, J. T.; Wang, L.; Kuhl, K. P.; Jackson, A.; Johnson, N. C.; Abram, D. N.; Hatsukade, T.; Hahn, C.; Jaramillo, T. F. Improved CO_2 Reduction Activity toward C2+ Alcohols on a Tandem Gold on Copper Electrocatalyst. *Nat. Catal.* **2018**, *1* (10), 764–771.

(30) Nellaiappan, S.; Kumar Katiyar, N.; Kumar, R.; Parui, A.; Deo Malviya, K.; Pradeep, K. G.;

Singh, A. K.; Sharma, S.; Sekhar Tiwary, C.; Biswas, K. High-Entropy Alloys as Catalysts for the CO_2 and CO Reduction Reactions: Experimental Realization. *ACS Catal.* **2020**, *17*, 36.

(31) Pedersen, J. K.; Batchelor, T. A. A.; Bagger, A.; Rossmeisl, J. High-Entropy Alloys as Catalysts for the CO_2 and CO Reduction Reactions. *ACS Catal.* **2020**, *10*, 2169–2176.

(32) Hanjun, L.; Honggang, H.; Yao, C.; Feili, L.; Hui, F.; Longsheng, Z.; Nan, Z.; Shuxing, B.; Tianxi, L. High-Entropy Alloy Aerogels A New Platform for Carbon Dioxide Reduction. *Adv. Mater*. **2023**, *35*, 2209242.

(33) Pi, Y.; Guo, J.; Shao, Q.; Huang, X. All-Inorganic $SrSnO_3$ Perovskite Nanowires for Efficient CO_2 Electroreduction. *Nano Energy* **2019**, *62*, 861–868.

(34) Zhu, Y.; Zhou, W.; Dong, Z.; Zhang, X.; Chen, Z.; Liu, Z.; Li, F.; Fan, J.; Jiao, M.; Liu, L. Nanosized $LaInO_3$ Perovskite for Efficient Electrocatalytic Reduction of CO_2 to Formate. *J. CO_2 Util.* **2023**, *68*, 102342.

(35) Yan, J.; Wang, X.; Guan, Y.; Liu, Y.; Wang, L.; Shao, Q.; Huang, Q. Structure-Evolved $YbBiO_3$ Perovskites for Highly Formate-Selective CO_2 Electroreduction. *Dalt. Trans*. **2023**, *52* (16), 5277–5286.

(36) Schwartz, M.; Cook, R. L.; Kehoe, V. M.; MacDuff, R. C.; Patel, J.; Sammells, A. F. Carbon Dioxide Reduction to Alcohols Using Perovskite-Type Electrocatalysts. *J. Electrochem. Soc.* **1993**, *140* (3), 5188.

(37) Mignard, D.; Barik, R. C.; Bharadwaj, A. S.; Pritchard, C. L.; Ragnoli, M.; Cecconi, F.; Miller, H.; Yellowlees, L. J. Revisiting Strontium-Doped Lanthanum Cuprate Perovskite for the Electrochemical Reduction of CO_2. *J. CO_2 Util.* **2014**, *5*, 53–59.

(38) Chen, S.; Su, Y.; Deng, P.; Qi, R.; Zhu, J.; Chen, J.; Wang, Z.; Zhou, L.; Guo, X.; Xia, B. Y.; Yu Xia, B. Highly Selective Carbon Dioxide Electroreduction on Structure-Evolved Copper Perovskite Oxide toward Methane Production. *ACS Catal.* **2020**, *23*, 12.

(39) Zhu, J.; Wang, Y.; Zhi, A.; Chen, Z.; Shi, L.; Zhang, Z.; Zhang, Y.; Zhu, Y.; Qiu, X.; Tian, X.; Bai, X.; Zhang, Y.; Zhu, Y. Cation-Deficiency-Dependent CO_2 Electroreduction over Copper-Based Ruddlesden-Popper Perovskite Oxides. *Angew. Chemie Int. Ed.* **2021**, *60*, 2–12.

(40) Whittingham, A. W. H.; Smith, R. D. L. Electrochemically Induced Phase Changes in La_2CuO_4 During Cathodic Electrocatalysis. *ChemElectroChem* **2019**, *6* (19), 5116–5123.

(41) Singh, R. P.; Arora, P.; Nellaiappan, S.; Shivakumara, C.; Irusta, S.; Paliwal, M.; Sharma, S. Electrochemical Insights into Layered La_2CuO_4 Perovskite: Active Ionic Copper for Selective CO_2 Electroreduction at Low Overpotential. *Electrochim. Acta* **2019**, *326*, 134952.

(42) Xu, Z.; Chen, P.; Gan, L.; Songtao, Y.; Pinger, Y.; Shuai, Y.; Mohsen, S.; Zhiqiang, W.; Tsun-Kong, S.; Zheng, G. High-rate CO_2-to-CH_4 Electrosynthesis by Undercoordinated Cu Sites in Alkaline-Earth-Metal Perovskites with Strong Basicity. *Adv. Energy Mater*. **2023**, 2204417.

(43) Sun, C.; Alonso, J. A.; Bian, J.; Sun, C. W.; Bian, J. J.; Alonso, J. A. Recent Advances in Perovskite-Type Oxides for Energy Conversion and Storage Applications. *Adv. Energy Mater.* **2021**, *11* (2), 2000459.

(44) Lang, R.; Du, X.; Huang, Y.; Jiang, X.; Zhang, Q.; Guo, Y.; Liu, K.; Qiao, B.; Wang, A.; Zhang, T. Single-Atom Catalysts Based on the Metal−Oxide Interaction. *Chem. Rev.* **2020**, *120*, 11986–12043.

(45) Zheng, T.; Jiang, K.; Ta, N.; Hu, Y.; Zeng, J.; Liu, J.; Wang, H. Large-Scale and Highly Selective CO_2 Electrocatalytic Reduction on Nickel Single-Atom Catalyst. *Joule* **2019**, *3*, 265–278.

(46) Koshy, D. M.; Chen, S.; Lee, D. U.; Stevens, M. B.; Abdellah, A. M.; Dull, S. M.; Chen, G.; Nordlund, D.; Gallo, A.; Hahn, C.; Higgins, D. C.; Bao, Z.; Jaramillo, T. F. Understanding the Origin of Highly Selective CO_2 Electroreduction to CO on Ni,N-doped Carbon Catalysts. *Angew. Chem. Int. Ed.* **2020**, *132* (10), 4072–4079.

(47) Gu, J.; Hsu, C. S.; Bai, L.; Chen, H. M.; Hu, X. Atomically Dispersed Fe^{3+} Sites Catalyze Efficient CO_2 Electroreduction to CO. *Science* **2019**, *364* (6445), 1091–1094.

(48) Li, K.; Zhang, S.; Zhang, X.; Liu, S.; Jiang, H.; Jiang, T.; Shen, C.; Yu, Y.; Chen, W. Atomic Tuning of Single-Atom Fe−N−C Catalysts with Phosphorus for Robust Electrochemical CO_2 Reduction. *Nano Lett.* **2022**, *22*, 1557–1565.

(49) Qin, X.; Zhu, S.; Xiao, F.; Zhang, L.; Shao, M. Active Sites on Heterogeneous Single-Iron-Atom Electrocatalysts in CO_2 Reduction Reaction. *ACS Energy Lett.* **2019**, *4*, 1778–1783.

(50) Pan, Y.; Lin, R.; Chen, Y.; Liu, S.; Zhu, W.; Cao, X.; Chen, W.; Wu, K.; Cheong, W.-C.; Wang, Y.; Zheng, L.; Luo, J.; Lin, Y.; Liu, Y.; Liu, C.; Li, J.; Lu, Q.; Chen, X.; Wang, D.; Peng, Q.; Chen, C.; Li, Y. Design of Single-Atom Co–N5 Catalytic Site: A Robust Electrocatalyst for CO_2 Reduction with Nearalya 100% CO Selectivity and Remarkable Stability. *J. Am. Chem. Soc.*

2018, *140* (12), 4218–4221.

(51) Zhang, B.; Zhang, J.; Shi, J.; Tan, D.; Liu, L.; Zhang, F.; Lu, C.; Su, Z.; Tan, X.; Cheng, X.; Han, B.; Zheng, L.; Zhang, J. Manganese Acting as a High-Performance Heterogeneous Electrocatalyst in Carbon Dioxide Reduction. *Nat. Commun.* **2019**, *10*, 2980.

(52) Feng, J.; Gao, H.; Zheng, L.; Chen, Z.; Zeng, S.; Jiang, C.; Dong, H.; Liu, L.; Zhang, S.; Zhang, X. A Mn-N3 Single-Atom Catalyst Embedded in Graphitic Carbon Nitride for Efficient CO_2 Electroreduction. *Nat. Commun.* **2020**, *11*, 4341.

(53) Ju, W.; Bagger, A.; Hao, G.-P.; Varela, A. S.; Sinev, I.; Bon, V.; Cuenya, B. R.; Kaskel, S.; Rossmeisl, J.; Strasser, P. Understanding Activity and Selectivity of Metal-Nitrogen-Doped Carbon Catalysts for Electrochemical Reduction of CO_2. *Nat. Commun.* **2017**, *8*.

(54) ByoungJoon, P.; Ying, W.; Yechan, L.; Kyung-Jong, N.; Ara, C.; Myeong Gao, J.; Rui, H.; Kug-Seung, L.; Jeong Woo, H. Effective Screening Route for Highly Active and Selective Metal−Nitrogen-Doped Carbon Catalysts in CO_2 Electrochemical Reduction. *Small* **2021**, 2103705.

(55) Ni, W.; Gao, Y.; Lin, Y.; Ma, C.; Guo, X.; Wang, S.; Zhang, S. Nonnitrogen Coordination Environment Steering Electrochemical CO_2-to-CO Conversion over Single-Atom Tin Catalysts in a Wide Potential Window. *ACS Catal.* **2021**, *11*, 5221.

(56) Zu, X.; Li, X.; Liu, W.; Sun, Y.; Xu, J.; Yao, T.; Yan, W.; Gao, S.; Wang, C.; Wei, S.; Xie, Y. Efficient and Robust Carbon Dioxide Electroreduction Enabled by Atomically Dispersed $Sn^{\Delta+}$ Sites. *Adv. Mater.* **2019**, *31* (15), 1808135.

(57) Shang, H.; Wang, T.; Pei, J.; Jiang, Z.; Zhou, D.; Wang, Y.; Li, H.; Dong, J.; Zhuang, Z.; Chen, W.; Wang, D.; Zhang, J.; Li, Y. Supporting Information Design of a Single-Atom Indium D+-N 4 Interface for Efficient Electroreduction of CO_2 to Formate. *Angew. Chem. Int. Ed.* **2020**, *59* (50), 22465–22469.

(58) Kang, X.; Wang, B.; Hu, K.; Lyu, K.; Han, X.; Spencer, B. F.; Frogley, M. D.; Tuna, F.; Mcinnes, E. J. L.; Dryfe, R. A. W.; Han, B.; Yang, S.; Schrö, M. Quantitative Electro-Reduction of CO_2 to Liquid Fuel over Electro-Synthesized Metal−Organic Frameworks. *J. Am. Chem. Soc.* **2020**, *142*, 17384–17392.

(59) Lu, P.; Tan, X.; Zhao, H.; Xiang, Q.; Liu, K.; Zhao, X.; Yin, X.; Li, X.; Hai, X.; Xi, S.; Wee, A. T. S.;

Pennycook, S. J.; Yu, X.; Yuan, M.; Wu, J.; Zhang, G.; Smith, S. C.; Yin, Z. Atomically Dispersed Indium Sites for Selective CO_2 Electroreduction to Formic Acid. *ACS Nano* **2021**, *15* (3), 5671–5678.

(60) Li, S.; Lu, X.; Zhao, S.; Ceccato, M.; Hu, X.-M.; Roldan, A.; Liu, M.; Daasbjerg, K. P-Block Indium Single-Atom Catalyst with Low-Coordinated In−N Motif for Enhanced Electrochemical CO_2 Reduction. *ACS Catal.* **2022**, *21*, 27.

(61) Jiang, Z.; Wang, T.; Pei, J.; Shang, H.; Zhou, D.; Li, H.; Dong, J.; Wang, Y.; Cao, R.; Zhuang, Z.; Chen, W.; Wang, D.; Zhang, J.; Li, Y. Discovery of Main Group Single Sb-N 4 Active Sites for CO_2 Electroreduction to Formate with High Efficiency. *Energy Environ. Sci*. **2020**, *13*, 2856.

(62) Jia, M.; Hong, S.; Wu, T.-S.; Li, X.; Soo, Y.-L.; Sun, Z.; Li, R.; Chemcomm, /; Communication, C. Single Sb Sites for Efficient Electrochemical CO_2 Reduction. *Chem. Commun.* **2019**, *55*, 12024.

(63) Guan, A.; Chen, Z.; Quan, Y.; Peng, C.; Wang, Z.; Sham, T.-K.; Yang, C.; Ji, Y.; Qian, L.; Xu, X.; Zheng, G. Boosting CO_2 Electroreduction to CH_4 via Tuning Neighboring Single-Copper Sites. *ACS Energy Lett.* **2020**, *5*, 1044–1053.

(64) Qiu, X.-F.; Zhu, H.-L.; Huang, J.-R.; Liao, P.-Q.; Chen, X.-M. Highly Selective CO_2 Electroreduction to C_2H_4 Using a Metal−Organic Framework with Dual Active Sites. *J. Am. Chem. Soc.* **2021**, *143*, 7242–7246.

(65) Zhao, K.; Nie, X.; Wang, H.; Chen, S.; Quan, X.; Yu, H.; Choi, W.; Zhang, G.; Kim, B.; Chen, J. G. Selective Electroreduction of CO_2 to Acetone by Single Copper Atoms Anchored on N-Doped Porous Carbon. *Nat. Commun.* **2020**, *11*, 2455.

(66) Xu, H.; Rebollar, D.; He, H.; Chong, L.; Liu, Y.; Liu, C.; Sun, C.-J.; Li, T.; Muntean, J. V; Winans, R. E.; Liu, D.-J.; Xu, T. Highly Selective Electrocatalytic CO_2 Reduction to Ethanol by Metallic Clusters Dynamically Formed from Atomically Dispersed Copper. *Nat. Energy* **2020**, *5*, 623–632.

(67) Ma, L.; Hu, W.; Mei, B.; Liu, H.; Yuan, B.; Zang, J.; Chen, T.; Zou, L.; Zou, Z.; Yang, B.; Yu, Y.; Ma, J.; Jiang, Z.; Wen, K.; Yang, H. Covalent Triazine Framework Confined Copper Catalysts for Selective Electrochemical CO_2 Reduction: Operando Diagnosis of Active Sites. *ACS Catal.* **2020**, *10*, 4534–4542.

(68) Yan, Y.; Zhao, Z.; Zhao, J.; Xu, Y.; Xu, Y.; Zhao, Y.; Tang, W.; Lee, J.-M. Constrained C_2 adsorbate orientation enables CO-to-acetate electroreduction. *Nature* **2021**, *18*, 4.

(69) Bai, X.; Zhao, X.; Zhang, Y.; Ling, C.; Zhou, Y.; Wang, J.; Liu, Y. Dynamic Stability of Copper Single-Atom Catalysts under Working Conditions. *J. Am. Chem. Soc*. **2022**, 17140–17148.

(70) Shang, H.; Wang, T.; Pei, J.; Jiang, Z.; Zhou, D.; Wang, Y.; Li, H.; Dong, J.; Zhuang, Z.; Chen, W.; Wang, D.; Zhang, J.; Li, Y. Design of a Single-Atom Indium$^{\delta+}$–N_4 Interface for Efficient Electroreduction of CO_2 to Formate. *Angew. Chem. Int. Ed.* **2020**, *59* (50), 22465–22469.

(71) Lakshmanan, K.; Huang, W.-H.; Chala, S. A.; Taklu, B. W.; Moges, E. A.; Lee, J.-F.; Huang, P.-Y.; Lee, Y.-C.; Tsai, M.-C.; Su, W.-N.; Hwang, B. J. Highly Active Oxygen Coordinated Configuration of Fe Single-Atom Catalyst toward Electrochemical Reduction of CO_2 into Multi-Carbon Products. *Adv. Funct. Mater.* **2022**, 2109310.

(72) Zhu, G.; Li, Y.; Zhu, H.; Su, H.; Chan, S. H.; Chan, H.; Sun, Q. Curvature-Dependent Selectivity of CO_2 Electrocatalytic Reduction on Cobalt Porphyrin Nanotubes. *ACS Catal*. **2016**, *6*, 6294−6301.

(73) Xiong, W.; Hongfang, L.; Huimin, W.; Yi, J.; You, H.; Zhang, S.; Hou, Y.; Gao, M.; Zhang, T.; Cao, R. Hollow Mesoporous Carbon Sphere Loaded Ni–N4 Single-Atom: Support Structure Study for CO_2 Electrocatalytic ReducRongtion Catalyst. *Small* **2020**, *16*, 2003943.

(74) Hao, Z.; Chen, J.; Zhang, D.; Zheng, L.; Yi, Y.; Yin, Z.; He, G.; Jiao, L.; Wen, Z.; Lv, X.-J. Coupling Effects of Zn Single Atom and High Curvature Supports for Improved Performance of CO_2 Reduction. *Sci. Bull.* **2021**, *66* (16), 1649–1658.

(75) Zhang, Y.; Jang, H.; Ge, X.; Zhang, W.; Li, Z.; Hou, L.; Zhai, L.; Wei, X.; Wang, Z.; Kim, M. G.; Liu, S.; Qin, Q.; Liu, X.; Cho, J.; Zhang, Y.; Hou, L.; Wei, X.; Wang, Z.; Liu, S.; Qin, Q.; Liu, X.; Jang, H.; Kim, M. G.; Ge, X.; Zhang, W.; Li, Z.; Zhai, L. Single-Atom Sn on Tensile-Strained ZnO Nanosheets for Highly Efficient Conversion of CO_2 into Formate. *Adv. Energy Mater*. **2022**, 2202695.

(76) Kim, T.W., Choi, K.S. Nanoporous $BiVO_4$ photoanodes with dual-layer oxygen evolution catalysts for solar water splitting, *Science* **2014**, *24*, 990-994.

(77) Wu, Y.; Jiang, Z.; Lu, X.; Liang, Y.; Wang, H. Domino Electroreduction of CO_2 to Methanol on a Molecular Catalyst. *Nature* **2019**, *575*, 639.

(78) Fairley, N.; Fernandez, V.; Richard-Plouet, M.; Guillot-Deudon, C.; Walton, J.; Smith, E.; Flahaut, D.; Greiner, M.; Biesinger, M.; Tougaard, S.; Morgan, D.; Baltrusaitis, J. Systematic and Collaborative Approach to Problem Solving Using X-Ray Photoelectron Spectroscopy. *Appl. Surf. Sci. Adv.* **2021**, *5*, 100112.

(79) Ravel, B.; Newville, M. ATHENA, ARTEMIS, HEPHAESTUS: Data Analysis for X-Ray Absorption Spectroscopy Using IFEFFIT. *J. Synchrotron Radiat.* **2005**, *12* (4), 537–541.

(80) Wang, V.; Xu, N.; Liu, J. C.; Tang, G.; Geng, W.-T. VASPKIT: A User-Friendly Interface Facilitating High-Throughput Computing and Analysis Using VASP Code. *Comput. Phys. Commun.* **2021**, *267*, 108033.

(81) Momma, K.; Izumi, F. VESTA 3 for Three-Dimensional Visualization of Crystal, Volumetric and Morphology Data. *J. Appl. Crystallogr*. **2011**, *44* (6), 1272–1276.

(82) Zhang, E.; Wang, T.; Yu, K.; Liu, J.; Chen, W.; Li, A.; Rong, H.; Lin, R.; Ji, S.; Zheng, X.; Wang, Y.; Zheng, L.; Chen, C.; Wang, D.; Zhang, J.; Li, Y.; Zhang, E.; Wang, T.; Yu, K. Bismuth Single Atoms Resulting from Transformation of Metal−Organic Frameworks and Their Use as Electrocatalysts for CO_2 Reduction. *J. Am. Chem. Soc.* **2019**, *141*, 28.

(83) Liu, X.; Wang, C. Z.; Hupalo, M.; Lu, W. C.; Tringides, M. C.; Yao, Y. X.; Ho, K. M. Metals on Graphene: Correlation between Adatom Adsorption Behavior and Growth Morphology. *Phys. Chem. Chem. Phys.* **2012**, *14* (25), 9157–9166.

(84) Gao, Z. Z.-Y.; Yang, W.-J. W.; Ding, X.-L. X.; Lv, G.; Yan, W. W.-P. Support Effects on Adsorption and Catalytic Activation of O_2 in Single Atom Iron Catalysts with Graphene-Based Substrates. *Phys. Chem. Chem. Phys.* **2018**, *20*, 7333.

(85) Grimme, S.; Antony, J.; Ehrlich, S. A Consistent and Accurate Ab Initio Parametrization of Density Functional Dispersion Correction (DFT-D) for the 94 Elements H-Pu. *J. Chem. Phys.* **2010**, *132*, 154104.

(86) Rosen, J.; Hutchings, G. S.; Lu, Q.; Rivera, S.; Zhou, Y.; Vlachos, D. G.; Jiao, F. Mechanistic Insights into the Electrochemical Reduction of CO_2 to CO on Nanostructured Ag Surfaces. *ACS Catal.* **2015**, *5*, 15.

(87) Fan, M.; Prabhudev, S.; Garbarino, S.; Qiao, J.; Botton, G. A.; Harrington, D. A.; Tavares, A. C.; Guay, D. Uncovering the Nature of Electroactive Sites in Nano Architectured Dendritic

Bi for Highly Efficient CO_2 Electroreduction to Formate. *Appl. Catal. B Environ.* **2020**, *274*, 119031.

(88) Birdja, Y. Y.; Pérez-Gallent, E.; Figueiredo, M. C.; Göttle, A. J.; Calle-Vallejo, F.; Koper, M. T. M. Advances and Challenges in Understanding the Electrocatalytic Conversion of Carbon Dioxide to Fuels. *Nat. Energy* **2019**, *4* (9), 732–745.

(89) Wang, P.; Qiao, M.; Shao, Q.; Pi, Y.; Zhu, X.; Li, Y.; Huang, X. Phase and Structure Engineering of Copper Tin Heterostructures for Efficient Electrochemical Carbon Dioxide Reduction. *Nat. Commun.* **2018**, *9*.

(90) Chen, Z.; Gao, M. R.; Duan, N.; Zhang, J. J.; Zhang, Y. Q.; Fan, T.; Zhang, J. J.; Dong, Y.; Li, J.; Liu, Q.; Yi, X.; Luo, J. L. Tuning Adsorption Strength of CO_2 and Its Intermediates on Tin Oxide-Based Electrocatalyst for Efficient CO_2 Reduction toward Carbonaceous Products. *Appl. Catal. B Environ.* **2020**, *277*, 119252.

(91) Yang, F.; Elnabawy, A. O.; Schimmenti, R.; Song, P.; Wang, J.; Peng, Z.; Yao, S.; Deng, R.; Song, S.; Lin, Y.; Mavrikakis, M.; Xu, W. Bismuthene for Highly Efficient Carbon Dioxide Electroreduction Reaction. *Nat. Commun.* **2020**, *11*.

(91) Gong, Q.; Ding, P.; Xu, M.; Zhu, X.; Wang, M.; Deng, J.; Ma, Q.; Han, N.; Zhu, Y.; Lu, J.; Feng, Z.; Li, Y. Y.; Zhou, W.; Li, Y. Y. Structural Defects on Converted Bismuth Oxide Nanotubes Enable Highly Active Electrocatalysis of Carbon Dioxide Reduction. *Nat. Commun.* **2019**, *10*, 2807.

(93) Wu, Z.; Wu, H.; Cai, W.; Wen, Z.; Jia, B.; Wang, L.; Jin, W.; Ma, T. Engineering Bismuth–Tin Interface in Bimetallic Aerogel with a 3D Porous Structure for Highly Selective Electrocatalytic CO_2 Reduction to HCOOH. *Angew. Chem. Int. Ed.* **2021**, *60* (22), 12554–12559.

(94) Grabowska, E. Selected Perovskite Oxides: Characterization, Preparation and Photocatalytic Properties-A Review. *Appl. Catal. B Environ.* **2016**, *186*, 97–126.

(95) Deka, D. J.; Kim, J.; Gunduz, S.; Aouine, M.; Millet, J. M. M.; Co, A. C.; Ozkan, U. S. Investigation of Hetero-Phases Grown via in-Situ Exsolution on a Ni-Doped (La,Sr)FeO_3 Cathode and the Resultant Activity Enhancement in CO_2 Reduction. *Appl. Catal. B Environ.* **2021**, *286*, 119917.

(96) Hwang, J.; Rao, R. R.; Giordano, L.; Katayama, Y.; Yu, Y.; Shao-Horn, Y. Perovskites in Catalysis and Electrocatalysis. *Science* **2017**, *358* (6364), 751–756.

(97) Wang, J.; Cheng, C.; Huang, B.; Cao, J.; Li, L.; Shao, Q.; Zhang, L.; Huang, X. Grain-Boundary-Engineered La_2CuO_4 Perovskite Nanobamboos for Efficient CO_2 Reduction Reaction. *Nano Lett.* **2021**, *21*, 980–987.

(98) Liu, S.; Gao, R.-T.; Sun, M.; Wang, Y.; Nakajima, T.; Liu, X.; Zhang, W.; Wang, L. In Situ Construction of Hybrid $Co(OH)_2$ Nanowires for Promoting Long-Term Water Splitting. *Appl. Catal. B Environ.* **2021**, *292*, 120063.

(99) Vavra, J.; Shen, T. H.; Stoian, D.; Tileli, V.; Buonsanti, R. Real-Time Monitoring Reveals Dissolution/Redeposition Mechanism in Copper Nanocatalysts during the Initial Stages of the CO_2 Reduction Reaction. *Angew. Chem. Int. Ed.* **2020**, *60*, 1347–1354.

(100) Jiang, H.; He, Q.; Zhang, Y.; Song, L. Structural Self-Reconstruction of Catalysts in Electrocatalysis. *Acc. Chem. Res.* **2018**, *51*, 2968–2977.

(101) Zhang, A.; Liang, Y.; Li, H.; Zhang, B.; Liu, Z.; Chang, Q.; Zhang, H.; Zhu, C.-F.; Geng, Z.; Zhu, W.; Zeng, J. In-Situ Surface Reconstruction of InN Nanosheets for Efficient CO_2 Electroreduction into Formate. *Nano Lett.* **2020**, *39*, 3.

(102) Chang, C.-J.; Lin, S.-C.; Chen, H.-C.; Wang, J.; Zheng, K. J.; Zhu, Y.; Chen, H. M. Dynamic Reoxidation/Reduction-Driven Atomic Interdiffusion for Highly Selective CO_2 Reduction toward Methane. *J. Am. Chem. Soc.* **2020**, *142*, 12119-12132.

(103) Gao, D.; Scholten, F.; Roldan Cuenya, B. Improved CO_2 Electroreduction Performance on Plasma-Activated Cu Catalysts via Electrolyte Design: Halide Effect. *ACS Catal.* **2017**, *7*, 5112–5120.

(104) Cao, C.; Ma, D. D.; Gu, J. F.; Xie, X.; Zeng, G.; Li, X.; Han, S. G.; Zhu, Q. L.; Wu, X. T.; Xu, Q. Metal–Organic Layers Leading to Atomically Thin Bismuthene for Efficient Carbon Dioxide Electroreduction to Liquid Fuel. *Angew. Chem. Int. Ed.* **2020**, *132* (35), 15014–15020.

(105) Zhu, J.; Zhang, W.; Li, Y.; Yue, W.; Geng, G.; Yu, B. Enhancing CO_2 Catalytic Activation and Direct Electroreduction on In-Situ Exsolved Fe/MnOx Nanoparticles from $(Pr,Ba)_2Mn_{2-Y}Fe_YO_{5+\delta}$ Layered Perovskites for SOEC Cathodes. *Appl. Catal. B Environ.* **2020**, *268*, 118389.

(106) Myung, J. H.; Neagu, D.; Miller, D. N.; Irvine, J. T. S. Switching on Electrocatalytic Activity in

Solid Oxide Cells. *Nature* **2016**, *537*, 528–531.

(107) Talha, M.; Lee, Y. W. Raman Modes and Dielectric Relaxation Properties of Epitaxial $BaBiO_3$ Thin Films. *Mater. Res. Express* **2020**, *7*, 16420.

(108) Lamagni, P.; Miola, M.; Catalano, J.; Hvid, M. S.; Mamakhel, M. A. H.; Christensen, M.; Madsen, M. R.; Jeppesen, H. S.; Hu, X. M.; Daasbjerg, K.; Skrydstrup, T.; Lock, N. Restructuring Metal–Organic Frameworks to Nanoscale Bismuth Electrocatalysts for Highly Active and Selective CO_2 Reduction to Formate. *Adv. Funct. Mater.* **2020**, *30*, 1910408.

(109) Zhao, M.; Gu, Y.; Gao, W.; Cui, P.; Tang, H.; Wei, X.; Zhu, H.; Li, G.; Yan, S.; Zhang, X.; Zou, Z. Atom Vacancies Induced Electron-Rich Surface of Ultrathin Bi Nanosheet for Efficient Electrochemical CO_2 Reduction. *Appl. Catal. B Environ*. **2020**, *266*, 118625.

(110) Zhang, W.; Hu, Y.; Ma, L.; Zhu, G.; Zhao, P.; Xue, X.; Chen, R.; Yang, S.; Ma, J.; Liu, J.; Jin, Z. Liquid-Phase Exfoliated Ultrathin Bi Nanosheets: Uncovering the Origins of Enhanced Electrocatalytic CO_2 Reduction on Two-Dimensional Metal Nanostructure. *Nano Energy* **2018**, *53*, 808–816.

(111) Kö, M.; Vaes, J.; Klemm, E.; Pant, D. Solvents and Supporting Electrolytes in the Electrocatalytic Reduction of CO_2. *Iscience* **2019**, *19*, 135–160.

(112) Ringe, S.; Chan, K.; Clark, E. L.; Resasco, J.; Walton, A.; Seger, B.; Bell, A. T. Understanding Cation Effects in Electrochemical CO_2 Reduction Understanding Cation Effects in Electrochemical CO_2 Reduction. *Energy Environ. Sci.* **2019**, *12* (10), 2851–3194.

(113) Li, X.; Cunathunge, C. M.; Agrawal, N.; Montalvo, C. H.; Jin, J.; Janik, M. J.; Waegele, M. M. Impact of Alkali Metal Cations and Iron Impurities on the Evolution of Hydrogen on Cu Electrodes in Alkaline Electrolytes. *J. Electrochem. Soc.* **2020**, *167*, 106505.

(114) Monteiro, M. C. O.; Dattila, F.; Hagedoorn, B.; García-muelas, R.; López, N.; Koper, M. T. M. Absence of CO_2 electroreduction on copper, gold and silver electrodes without metal cations in solution. *Nat. Catal*. **2021**, *4*, 654-662.

(115) Nightingale, E.R. Phenomenological Theory of Ion Solvation. Effecitve Radii of Hydrated Ions. *J. Phys. Chem*. **1959**, *63*, 1381-1386.

(116) Lee, C.-Y.; Wallace, G. G. CO_2 Electrolysis in Seawater: Calcification Effect and a Hybrid Self-

Powered Concept. *J. Mater. Chem. A* **2018**, *6*, 23301.

(117) Schizodimou, A.; Kyriacou, G. Acceleration of the Reduction of Carbon Dioxide in the Presence of Multivalent Cations. *Electrochim. Acta* **2012**, *78*, 171–176.

(118) Deka, D. J.; Kim, J.; Gunduz, S.; Jain, D.; Shi, Y.; Miller, J. T.; Co, A. C.; Ozkan, U. S. Coke Formation during High-Temperature CO_2 Electrolysis over $AFeO_3$ (A = La/Sr) Cathode: Effect of A-Site Metal Segregation. *Appl. Catal. B Environ.* **2021**, *283*, 119642.

(119) Chernyshova, I. V.; Somasundaran, P.; Ponnurangam, S. On the Origin of the Elusive First Intermediate of CO_2 Electroreduction. *Proc. Natl. Acad. Sci. U.S.A.* **2018**, *115* (40), E9261–E9270.

(120) Pan, Z.; Wang, K.; Ye, K.; Wang, Y.; Su, H.-Y.; Hu, B.; Xiao, J.; Yu, T.; Wang, Y.; Song, S. Intermediate Adsorption States Switch to Selectively Catalyze Electrochemical CO_2 Reduction. *ACS Catal.* **2020**, *10*, 3880.

(121) Banerjee, S.; Zhang, Z.-Q.; Hall, A. S.; Thoi, V. S. Surfactant Perturbation of Cation Interactions at the Electrode−Electrolyte Interface in Carbon Dioxide Reduction. *ACS Catal.* **2020**, *10*, 9907–9914.

(122) Wallentine, S.; Bandaranayake, S.; Biswas, S.; Baker, L. R. Direct Observation of Carbon Dioxide Electroreduction on Gold: Site Blocking by the Stern Layer Controls CO_2 Adsorption Kinetics. *J. Phys. Chem. Lett.* **2020**, *11*, 8307–8313.

(123) Banerjee, S.; Han, X.; Thoi, V. S. Modulating the Electrode−Electrolyte Interface with Cationic Surfactants in Carbon Dioxide Reduction. *ACS Catal.* **2019**, *9*, 5631–5637.

(124) Dunwell, M.; Lu, Q.; Heyes, J. M.; Rosen, J.; Chen, J. G.; Yan, Y.; Jiao, F.; Xu, B. The Central Role of Bicarbonate in the Electrochemical Reduction of Carbon Dioxide on Gold. *J. Am. Chem. Soc.* **2017**, *139*, 3774–3783.

(125) Singh, M. R.; Kwon, Y.; Lum, Y.; Ager, J. W.; Bell, A. T. Hydrolysis of Electrolyte Cations Enhances the Electrochemical Reduction of CO2 over Ag and Cu. *J. Am. Chem. Soc.* **2016**, *138* (39), 13006–13012.

(126) Liu, S.; Lu, X. F.; Xiao, J.; Wang, X.; Lou, X. W. (David). Bi_2O_3 Nanosheets Grown on Multi-Channel Carbon Matrix to Catalyze Efficient CO_2 Electroreduction to HCOOH. *Angew. Chem. Int. Ed.* **2019**, *58*, 13828–13833.

(127) Zhang, Y.; Li, F.; Zhang, X.; Williams, T.; Easton, C. D.; Bond, A. M.; Zhang, J. Electrochemical Reduction of CO_2 on Defect-Rich Bi Derived from Bi_2S_3 with Enhanced Formate Selectivity. *J. Mater. Chem. A* **2018**, *6*, 4714.

(128) Yang, X.; Deng, P.; Liu, D.; Zhao, S.; Li, D.; Wu, H.; Ma, Y.; Xia, B. Y.; Li, M.; Xiao, C.; Ding, S. Partial Sulfuration-Induced Defect and Interface Tailoring on Bismuth Oxide for Promoting Electrocatalytic CO_2 Reduction. *J. Mater. Chem. A* **2020**, *8* (5), 2472–2480.

(129) Fan, K.; Jia, Y.; Ji, Y.; Kuang, P.; Zhu, B.; Liu, X.; Yu, J. Curved Surface Boosts Electrochemical CO_2 Reduction to Formate via Bismuth Nanotubes in a Wide Potential Window. *ACS Catal.* **2020**, *10* (1), 358–364.

(130) Duan, Y.-X.; Liu, K.-H.; Zhang, Q.; Yan, J.-M.; Jiang, Q. Efficient CO_2 Reduction to HCOOH with High Selectivity and Energy Efficiency over Bi/RGO Catalyst. *Small Methods* **2020**, *4*, 1900846.

(131) Zhang, Y.; Zhang, X.; Ling, Y.; Li, F.; Bond, A. M.; Zhang, J. Controllable Synthesis of Few-Layer Bismuth Subcarbonate by Electrochemical Exfoliation for Enhanced CO_2 Reduction Performance. *Angew. Chem. Int. Ed.* **2018**, *57* (40), 13283–13287.

(132) Zhou, Y.; Yan, P.; Jia, J.; Zhang, S.; Zheng, X.; Zhang, L.; Zhang, B.; Chen, J.; Hao, W.; Chen, G.; Xu, Q.; Han, B. Supercritical CO_2-Constructed Intralayer $[Bi_2O_2]^{2+}$ Structural Distortion for Enhanced CO_2 Electroreduction. *J. Mater. Chem. A* **2020**, *8*, 13320.

(133) Li, F.; Gu, G. H.; Choi, C.; Kolla, P.; Hong, S.; Wu, T.-S. S.; Soo, Y.-L. L.; Masa, J.; Mukerjee, S.; Jung, Y.; Qiu, J.; Sun, Z. Highly Stable Two-Dimensional Bismuth Metal-Organic Frameworks for Efficient Electrochemical Reduction of CO_2. *Appl. Catal. B Environ.* **2020**, *277*, 119241.

(134) Zhang, X.; Zhang, Y.; Li, Q.; Zhou, X.; Li, Q.; Yi, J.; Liu, Y.; Zhang, J. Highly Efficient and Durable Aqueous Electrocatalytic Reduction of CO_2 to HCOOH with a Novel Bismuth-MOF: Experimental and DFT Studies. *J. Mater. Chem. A* **2020**, *8*, 9776.

(135) Zhou, J.; Yuan, K.; Zhou, L.; Guo, Y.; Luo, M.; Guo, X.; Meng, Q.; Zhang, Y. Boosting Electrochemical Reduction of CO_2 at a Low Overpotential by Amorphous Ag-Bi-S-O Decorated Bi^0 Nanocrystals. *Angew. Chem. Int. Ed.* **2019**, *58*, 14197–14201.

(136) Zhang, J.; Pan, B.; Li, Y. Modulating Electrochemical CO2 Reduction at Interfaces. *Sci. Bull.*

2022, *67* (18), 1844–1848.

(137) Liu, H.; Zhu, Y.; Ma, J.; Zhang, Z.; Hu, W. Recent Advances in Atomic-Level Engineering of Nanostructured Catalysts for Electrochemical CO_2 Reduction. *Adv. Funct. Mater.* **2020**, *30*, 1910534.

(138) Han, N.; Wang, Y.; Yang, H.; Deng, J.; Wu, J.; Li, Y.; Li, Y. Ultrathin Bismuth Nanosheets from in Situ Topotactic Transformation for Selective Electrocatalytic CO_2 Reduction to Formate. *Nat. Commun.* **2018**, *9* (1), 1–8.

(139) Fan, J.; Zhao, X.; Mao, X.; Xu, J.; Han, N.; Hao, Y.; Pan, B.; Li, Y.; Wang, L.; Li, Y. Large-Area Vertically Aligned Bismuthene Nanosheet Arrays from Galvanic Replacement. *Adv. Mater.* **2021**, *33*, 2100910.

(140) Wu, Y.; Liang, Y.; Wang, H. Heterogeneous Molecular Catalysts of Metal Phthalocyanines for Electrochemical CO_2 Reduction Reactions. *Acc. Chem. Res.* **2021**, *54*, 3149–3159.

(141) Zu, X.; Li, X.; Liu, W.; Sun, Y.; Xu, J.; Yao, T.; Yan, W.; Gao, S.; Wang, C.; Wei, S.; Xie, Y. Efficient and Robust Carbon Dioxide Electroreduction Enabled by Atomically Dispersed $Sn^{\delta+}$ Sites. *Adv. Mater.* **2019**, *31* (15), 1808135.

(142) Yi, L.; Chen, J.; Shao, P.; Huang, J.; Peng, X.; Li, J.; Wang, G.; Zhang, C.; Wen, Z. Molten-Salt-Assisted Synthesis of Bismuth Nanosheets for Long-Term Continuous Electrocatalytic Conversion of CO_2 to Formate. *Angew. Chem. Int. Ed.* **2020**, *59*, 2–10.

(143) Wang, Z.; Wang, C.; Hu, Y.; Yang, S.; Yang, J.; Chen, W.; Zhou, H.; Zhou, F.; Wang, L.; Du, J.; Li, Y.; Wu, Y. Simultaneous Diffusion of Cation and Anion to Access N, S Co-Coordinated Bi-Sites for Enhanced CO_2 Electroreduction. *Nano Res.* **2021**, *14*, 2790–2796.

(144) Yang, X.; Chen, Y.; Qin, L.; Wu, X.; Wu, Y.; Yan, T.; Geng, Z.; Zeng, J. Boost Selectivity of $HCOO^-$ Using Anchored Bi Single Atoms toward CO_2 Reduction. *ChemSusChem* **2020**, *13*, 6307–6311.

(145) Xu, S.; Zhong, G.; Chen, C.; Zhou, M.; Kline, D. J.; Jacob, R. J.; Xie, H.; He, S.; Huang, Z.; Dai, J.; Brozena, A. H.; Shahbazian-Yassar, R.; Zachariah, M. R.; Anlage, S. M.; Hu, L. Uniform, Scalable, High-Temperature Microwave Shock for Nanoparticle Synthesis through Defect Engineering. *Matter* **2019**, *1* (3), 759–769.

(146) Nakada, K.; Ishii, A. Migration of Adatom Adsorption on Graphene Using DFT Calculation.

Solid State Commun. **2011**, *151*, 13–16.

(147) Wang, Y.; Xu, L.; Zhan, L.; Yang, P.; Tang, S.; Liu, M.; Zhao, X.; Xiong, Y.; Chen, Z.; Lei, Y. Electron Accumulation Enables Bi Efficient CO_2 Reduction for Formate Production to Boost Clean Zn-CO_2 Batteries. *Nano Energy* **2022**, *92*, 106780.

(148) Shi, C.; Hansen, H. A.; Lausche, A. C.; Nørskov, J. K. Trends in Electrochemical CO_2 Reduction Activity for Open and Close-Packed Metal Surfaces. *Phys. Chem. Chem. Phys.* **2014**, *16*, 4720.

(149) He, S.; Ni, F.; Ji, Y.; Wang, L.; Wen, Y.; Bai, H.; Liu, G.; Zhang, Y.; Li, Y.; Zhang, B.; Peng, H. The P-Orbital Delocalization of Main-Group Metals to Boost CO_2 Electroreduction. *Angew. Chem. Int. Ed.* **2018**, *57* (49), 16114–16119.

(150) Jiang, H.; Liu, X.; Zhu, M.-N.; Xu, J.; An, L.; Sui, P.-F. F.; Luo, J.-L.; Cheng, G. J. Nanoalloy Libraries from Laser-Induced Thermionic Emission Reduction. *Sci. Adv*. **2022**, *8* (16), eabm6541.

(151) Zhang, T.; Chang, H.; Wu, Y.; Xiao, P.; Yi, N.; Lu, Y.; Ma, Y.; Huang, Y.; Zhao, K.; Yan, X.-Q.; Liu, Z.-B.; Tian, J.-G.; Chen, Y. Macroscopic and Direct Light Propulsion of Bulk Graphene Material. *Nat. Photon*. **2015**, *9*, 471-477.

(152) Wosylus, A.; Hoffmann, S.; Schmidt, M.; Ruck, M. In-Situ Study of the Solid-Gas Reaction of $BiCl_3$ to BiOCl via the Intermediate Hydrate $BiCl_3 \cdot H_2O$. *Eur. J. Inorg. Chem.* **2010**, 1469–1471.

(153) Wu, L.; Hu, S.; Yu, W.; Shen, S.; Li, T. Stabilizing Mechanism of Single-Atom Catalysts on a Defective Carbon Surface. *npj Comput. Mater.* **2020**, *6*, 23.

(154) Ramasse, Q. M.; Zan, R.; Bangert, U.; Boukhvalov, D. W.; Son, Y.-W.; Novoselov, K. S. Direct Experimental Evidence of Metal-Mediated Etching of Suspended Graphene. *ACS Nano* **2012**, *6* (5), 4063–4071.

(155) Dau, H.; Liebisch, P.; Haumann, M. X-Ray Absorption Spectroscopy to Analyze Nuclear Geometry and Electronic Structure of Biological Metal Centers-Potential and Questions Examined with Special Focus on the Tetra-Nuclear Manganese Complex of Oxygenic Photosynthesis. *Anal. Bioanal. Chem.* **2003**, *376* (5), 562–583.

(156) Li, Q.; Zhu, H.; Zheng, L.; Fan, L.; Ren, Y.; Chen, J.; Deng, J.; Xing, X. Local Structural Distortion Induced Uniaxial Negative Thermal Expansion in Nanosized Semimetal Bismuth.

Adv. Sci. **2016**, *3* (11), 1600108.

(157) Gong, Y.; Jiao, L.; Qian, Y.; Pan, C.; Zheng, L.; Cai, X.; Liu, B.; Yu, S.; Jiang, H. Regulating the Coordination Environment of MOF-Templated Single- Atom Nickel Electrocatalysts for Boosting CO_2 Reduction. *Angew. Chem. Int. Ed.* **2020**, *132*, 2727–2731.

(158) Fei, H.; Dong, J.; Feng, Y.; Allen, C. S.; Wan, C.; Volosskiy, B.; Li, M.; Zhao, Z.; Wang, Y.; Sun, H.; An, P.; Chen, W.; Guo, Z.; Lee, C.; Chen, D.; Shakir, I.; Liu, M.; Hu, T.; Li, Y.; Kirkland, A. I.; Duan, X.; Huang, Y. General Synthesis and Definitive Structural Identification of MN4C4 Single-Atom Catalysts with Tunable Electrocatalytic Activities. *Nat. Catal.* **2018**, *1*, 63–72.

(159) Zhang, J.; Mao, X.; Pan, B.; Xu, J.; Ding, X.; Han, N.; Wang, L.; Wang, Y.; Li, Y. Surface Promotion of Copper Nanoparticles with Alumina Clusters Derived from Layered Double Hydroxide Accelerates CO_2 Reduction to Ethylene in Membrane Electrode Assemblies. *Nano Res.* **2022**.

(160) Ma, W.; Xie, S.; Zhang, X. G.; Sun, F.; Kang, J.; Jiang, Z.; Zhang, Q.; Wu, D. Y.; Wang, Y. Promoting Electrocatalytic CO_2 Reduction to Formate via Sulfur-Boosting Water Activation on Indium Surfaces. *Nat. Commun.* **2019**, *10*, 892.

(161) Dutta, A.; Montiel, I. Z.; Kiran, K.; Rieder, A.; Grozovski, V.; Gut, L.; Broekmann, P. A Tandem (Bi_2O_3 → Bimet) Catalyst for Highly Efficient ec-CO_2 Conversion into Formate: Operando Raman Spectroscopic Evidence for a Reaction Pathway Change. *ACS Catal.* **2021**, *11*, 4988–5003.

(162) Atifi, A.; Boyce, D. W.; Dimeglio, J. L.; Rosenthal, J. Directing the Outcome of CO_2 Reduction at Bismuth Cathodes Using Varied Ionic Liquid Promoters. *ACS Catal.* **2018**, *8*, 2857−2863.

(163) Zhuo, H.-Y.; Zhang, X.; Liang, J.-X.; Yu, Q.; Xiao, H.; Li, J. Theoretical Understandings of Graphene-Based Metal Single-Atom Catalysts: Stability and Catalytic Performance. *Chem. Rev.* **2020**, *120* (21), 12315–12341.

(164) Hu, X.; Yao, S.; Chen, L.; Zhang, X.; Jiao, M.; Lu, Z.; Zhou, Z. Understanding the Role of Axial O in CO_2 Electroreduction on NiN 4 Single-Atom Catalysts via Simulations in Realistic Electrochemical Environment. *J. Mater. Chem. A* **2021**, *9*, 23515.

(165) Wang, X. X.; Cullen, D. A.; Pan, Y. T.; Hwang, S.; Wang, M.; Feng, Z.; Wang, J.; Engelhard, M. H.; Zhang, H.; He, Y.; Shao, Y.; Su, D.; More, K. L.; Spendelow, J. S.; Wu, G. Nitrogen-

Coordinated Single Cobalt Atom Catalysts for Oxygen Reduction in Proton Exchange Membrane Fuel Cells. *Adv. Mater.* **2018**, *30* (11).

(166) Li, K.; Zhang, S.; Zhang, X.; Liu, S.; Jiang, H.; Jiang, T.; Shen, C.; Yu, Y.; Chen, W. Atomic Tuning of Single-Atom Fe−N−C Catalysts with Phosphorus for Robust Electrochemical CO_2 Reduction. *Nano Lett.* **2022**, *22* (4), 1557–1565.

(167) Li, X.; Rong, H.; Zhang, J.; Wang, D.; Li, Y. Modulating the Local Coordination Environment of Single-Atom Catalysts for Enhanced Catalytic Performance. *Nano Res.* **2019**, *13* (7), 1842–1855.

(168) Zhu, G.; Li, Y.; Zhu, H.; Su, H.; Chan, S. H.; Chan, H.; Sun, Q. Curvature-Dependent Selectivity of CO_2 Electrocatalytic Reduction on Cobalt Porphyrin Nanotubes. *ACS Catal.* **2016**, *6*, 6294−6301.

(160) Mei, B.; Liu, C.; Sun, F.; Lu, S.; Du, X.; Li, X.; Song, F.; Xu, W.; Jiang, Z. Unraveling the Potential-Dependent Volcanic Selectivity Changes of an Atomically Dispersed Ni Catalyst During CO_2 Reduction. *ACS Catal.* **2022**, *58*, 5.

(169) Jia, Q.; Ramaswamy, N.; Hafiz, H.; Tylus, U.; Strickland, K.; Wu, G.; Barbiellini, B.; Bansil, A.; Holby, E. F.; Zelenay, P.; Mukerjee, S. Experimental Observation of Redox-Induced Fe-N Switching Behavior as a Determinant Role for Oxygen Reduction Activity. *ACS Nano* **2015**, *9* (12), 12496–12505.

(170) Wang, Q.; Ina, T.; Chen, W. T.; Shang, L.; Sun, F.; Wei, S.; Sun-Waterhouse, D.; Telfer, S. G.; Zhang, T.; Waterhouse, G. I. N. Evolution of Zn(II) Single Atom Catalyst Sites during the Pyrolysis-Induced Transformation of ZIF-8 to N-Doped Carbons. *Sci. Bull.* **2020**, *65*, 1743–1751.

(171) Miao, Z.; Wang, X.; Zhao, Z.; Zuo, W.; Chen, S.; Li, Z.; He, Y.; Liang, J.; Ma, F.; Wang, H.-L.; Lu, G.; Huang, Y.; Wu, G.; Li, Q. Improving the Stability of Non-Noble-Metal M–N–C Catalysts for Proton-Exchange-Membrane Fuel Cells through M–N Bond Length and Coordination Regulation. *Adv. Mater.* **2021**, *33*, 2006613.

(172) Adli, N. M.; Shan, W.; Hwang, S.; Samarakoon, W.; Karakalos, S.; Li, Y.; Cullen, D. A.; Su, D.; Feng, Z.; Wang, G.; Wu, G. Engineering Atomically Dispersed FeN4 Active Sites for CO_2 Electroreduction. *Angew. Chem. Int. Ed.* **2021**, *133*, 1035–1045.

(173) Krasnov, P. O.; Basova, T. V; Hassan, A. Interaction of Metal Phthalocyanines with Carbon Zigzag and Armchair Nanotubes with Different Diameters. *Appl. Surf. Sci.* **2018**, *457*, 235–240.

(174) Wang, M.; Chen, L.; Lau, T. C.; Robert, M. A Hybrid Co Quaterpyridine Complex/Carbon Nanotube Catalytic Material for CO_2 Reduction in Water. *Angew. Chem. Int. Ed.* **2018**, *57* (26), 7769–7773.

(175) Zhu, M.; Chen, J.; Guo, R.; Xu, J.; Fang, X.; Han, Y.-F. F. Cobalt Phthalocyanine Coordinated to Pyridine-Functionalized Carbon Nanotubes with Enhanced CO_2 Electroreduction. *Appl. Catal. B Environ.* **2019**, *251*, 112–118.

(176) Wu, X.; Sun, J. W.; Liu, P. F.; Zhao, J. Y.; Liu, Y.; Guo, L.; Dai, S.; Yang, H. G.; Zhao, H. Molecularly Dispersed Cobalt Phthalocyanine Mediates Selective and Durable CO_2 Reduction in a Membrane Flow Cell. *Adv. Funct. Mater.* **2021**, *2*, 2107301.

(177) Liu, Y.; Deb, A.; Leung, K. Y.; Nie, W.; Dean, W. S.; Penner-Hahn, J. E.; Mccrory, C. C. L. Determining the Coordination Environment and Electronic Structure of Polymer-Encapsulated Cobalt Phthalocyanine under Electrocatalytic CO_2 Reduction Conditions Using in Situ X-Ray Absorption Spectroscopy. *Dalt. Trans.* **2020**, *49*, 16329.

(178) Kim, H.; Shin, D.; Yang, W.; Hye Won, D.; Oh, H.-S.; Wook Chung, M.; Jeong, D.; Hee Kim, S.; Hwa Chae, K.; Yeon Ryu, J.; Lee, J.; June Cho, S.; Seo, J.; Kim, H.; Hyuck Choi, C. Identification of Single-Atom Ni Site Active toward Electrochemical CO_2 Conversion to CO. *J. Am. Chem. Soc.* **2021**, *143*, 925–933.

(179) Wu, H.; Zeng, M.; Zhu, X.; Tian, C.; Mei, B.; Song, Y.; Du, X. L.; Jiang, Z.; He, L.; Xia, C.; Dai, S. Defect Engineering in Polymeric Cobalt Phthalocyanine Networks for Enhanced Electrochemical CO_2 Reduction. *ChemElectroChem* **2018**, *5* (19), 2717–2721.

(180) Han, N.; Wang, Y.; Ma, L.; Wen, J.; Li, J.; Zheng, H.; Nie, K.; Wang, X.; Zhao, F.; Li, Y.; Fan, J.; Zhong, J.; Wu, T.; Miller, D. J.; Lu, J.; Lee, S. T.; Li, Y. Supported Cobalt Polyphthalocyanine for High-Performance Electrocatalytic CO_2 Reduction. *Chem* **2017**, *3* (4), 652–664.

(181) Yang, M.; Wu, K.; Sun, S.; Duan, J.; Liu, X.; Cui, J.; Liang, S.; Ren, Y. Unprecedented Relay Catalysis of Curved Fe1-N4 Single-Atom Site for Remarkably Efficient $^1O_2$ Generation. *ACS Catal.* **2023**, *13*, 681–691.

(182) Han, G.; Zhang, X.; Liu, W.; Zhang, Q.; Wang, Z.; Cheng, J.; Yao, T.; Gu, L.; Du, C.; Gao, Y.; Yin, G. Substrate Strain Tunes Operando Geometric Distortion and Oxygen Reduction Activity of CuN2C2 Single-Atom Sites. *Nat. Commun.* **2021**, *12* (1), 6335.

(183) Wang, J.; Huang, X.; Xi, S.; Xu, H.; Wang, X. Axial Modification of Cobalt Complexes on Heterogeneous Surface with Enhanced Electron Transfer for Carbon Dioxide Reduction. *Angew. Chem. Int. Ed.* **2020**, *59* (43), 19162–19167.

(184) Zhang, X. X.; Wu, Z.; Zhang, X. X.; Li, L.; Li, Y.; Xu, H.; Li, X.; Yu, X.; Zhang, Z.; Liang, Y.; Wang, H. Highly Selective and Active CO_2 Reduction Electrocatalysts Based on Cobalt Phthalocyanine/Carbon Nanotube Hybrid Structures. *Nat. Commun.* **2017**, *8*, 1–8.

(185) Anantharaj, S.; Subrata, K. Do the Evaluation Parameters Reflect Intrinsic Activity of Electrocatalysts in Electrochemical Water Splitting? *ACS Energy Lett.* **2019**, *4*, 1260–1264.

(186) Wei, C.; Sun, S.; Mandler, D.; Xun Wang, B.; Zhang Qiao, S.; Xu, Z. J. Approaches for Measuring the Surface Areas of Metal Oxide Electrocatalysts for Determining Their Intrinsic Electrocatalytic Activity. *Chem. Soc. Rev.* **2019**, *48*, 2518.

(187) Anantharaj, S.; Karthik, P. E.; Noda, S. The Significance of Properly Reporting Turnover Frequency in Electrocatalysis Research. *Angew. Chem. Int. Ed.* **2021**, *60* (43), 23051–23067.

(188) Sun, C.; Hou, Y.; Lüdi, N.; Hu, H.; De Jesús Gálvez-Vázquez, M.; Liechti, M.; Kong, Y.; Liu, M.; Erni, R.; Rudnev, A. V; Broekmann, P. Improving the Lifetime of Hybrid CoPc@MWCNT Catalysts for Selective Electrochemical CO_2-to-CO Conversion. *J. Catal.* **2022**, *407*, 198–205.

(189) Yang, H.; Lin, Q.; Zhang, C.; Yu, X.; Cheng, Z.; Li, G.; Hu, Q.; Ren, X.; Zhang, Q.; Liu, J.; He, C. Carbon Dioxide Electroreduction on Single-Atom Nickel Decorated Carbon Membranes with Industry Compatible Current Densities. *Nat. Commun.* **2020**, *11*, 593.

(190) Chen, Z.; Jiang, S.; Kang, G.; Nguyen, D.; Schatz, G. C.; Van Duyne, R. P. Operando Characterization of Iron Phthalocyanine Deactivation during Oxygen Reduction Reaction Using Electrochemical Tip-Enhanced Raman Spectroscopy. *J. Am. Chem. Soc.* **2019**, *141*, 15684–15692.

(191) Wan, L.; Zhao, K.; Wang, Y.-C.; Wei, N.; Zhang, P.; Yuan, J.; Zhou, Z.; Sun, S.-G. Molecular Degradation of Iron Phthalocyanine during the Oxygen Reduction Reaction in Acidic Media. *ACS Catal.* **2022**, *12*, 11097–11107.

(192) Xie, X.; He, C.; Li, B.; He, Y.; Cullen, D. A.; Wegener, E. C.; Kropf, A. J.; Martinez, U.; Cheng, Y.; Engelhard, M. H.; Bowden, M. E.; Song, M.; Lemmon, T.; Li, X. S.; Nie, Z.; Liu, J.; Myers, D. J.; Zelenay, P.; Wang, G.; Wu, G.; Ramani, V.; Shao, Y. Performance Enhancement and Degradation Mechanism Identification of a Single-Atom Co–N–C Catalyst for Proton Exchange Membrane Fuel Cells. *Nat. Catal.* **2020**, *3* (12), 1044–1054.

(193) Xi, W.; Haes, A. J. Elucidation of PH Impacts on Monosubstituted Benzene Derivatives Using Normal Raman and Surface-Enhanced Raman Scattering. *J. Chem. Phys.* **2020**, *153*, 184707.

(194) Blacha-Grzechnik, A.; Turczyn, R.; Burek, M.; Zak, J. In Situ Raman Spectroscopic Studies on Potential-Induced Structural Changes in Polyaniline Thin Films Synthesized via Surface-Initiated Electropolymerization on Covalently Modified Gold Surface. *Vib. Spectrosc.* **2014**, *71*, 30–36.

(195) Shi, L.-L.; Li, M.; You, B.; Liao, R.-Z. Theoretical Study on the Electro-Reduction of Carbon Dioxide to Methanol Catalyzed by Cobalt Phthalocyanine. *Inorg. Chem.* **2022**, *61*, 16549–16564.

(196) Liu, Q.; Zhang, X.; Zeng, W.; Wang, J.; Zhou, Z. Fine-Tuning of Electronic Structure of Cobalt(II) Ion in Nonplanar Porphyrins and Tracking of a Cross-Hybrid Stage: Implications for the Distortion of Natural Tetrapyrrole Macrocycles. *J. Phys. Chem. B* **2015**, *119*, 14102–14110.